Modifying redox and binding interactions between coordinated manganese and native bacterial reaction centers

Charles Protheroe

A Thesis in the Department of Physics

Presented in Partial Fulfillment of the Requirements

For the Degree of

Master of Science (Physics)

at

Concordia University

Montreal, Quebec, Canada

February 2016

CONCORDIA UNIVERSITY
School of Graduate Studies

This is to certify that the thesis prepared

By: Charles Protheroe

Entitled: Modifying redox and binding interactions between coordinated manganese and native bacterial reaction centers

and submitted in partial fulfillment of the requirements for the degree of

Master of Science (Physics)

complies with the regulations of the University and meets the accepted standards with respect to originality and quality.

Signed by the final examining committee:

Dr. Sushil Misra Chair

Dr. Pablo Bianucci Examiner

Dr. Valter Zazubovits Examiner

Dr. Laszlo Kalman Supervisor

Approved by _____
Chair of Department or Graduate Program Director

_____
Dean of Faculty

Date _____

Abstract

Modifying redox and binding interactions between coordinated manganese and native bacterial reaction centers

Charles Protheroe

Between 2.8 and 2.4 billion years ago Nature designed a method to catalytically split water into oxygen and hydrogen with sunlight, a process that humanity struggles to perform efficiently to this day. This manifested itself as the evolution from anoxygenic to oxygenic photosynthesis, a process which involved the incorporation of manganese ions from the environment by anoxygenic photosynthetic organisms, in order to utilize water as a new electron source. Recently, native bacterial reaction centers (BRCs), the protein complexes responsible for the photoelectric energy conversion of anoxygenic photosynthetic organisms, were shown to be able to utilize manganese as a secondary electron donor, an ability thought to only be possessed by oxygenic reaction centers. Here we uncovered several important details of this interaction, including the binding and donating sites of manganese in the BRCs, the rate of electron transfer from manganese to the BRC, and information on the composition of the manganese complex. This new information sheds light on the earliest step in the transition from anoxygenic to oxygenic photosynthesis, allowing an evaluation of the feasability of this potential evolutionary pathway by considering the effects of manganese on the native secondary electron donor, and on the final electron acceptor.

Acknowledgments

Firstly, I'd like to thank my supervisor, Dr. Lászlo Kálmán, for his relentless guidance and support throughout my time here. I would have never been able to connect my knowledge of physics with the worlds of biology and chemistry if it weren't for him. I am also greatly indebted to the knowledge and help of my colleague Dr. Sasmit Deshmukh, who has provided a model of a researcher which I strive to emulate. A special thank you is owed to the Misra group, including Lin Li and Dr. Sergey Andronenko, for their measurements of EPR spectra for us. Additionally, I'd like to thank Zejlko Bulut and Wentworth Brookes, for their invaluable technical expertise, previous colleagues, Matei-Alexandru Ivanescu and Sarah Lag, for their help and company, and Dr. Valter Zazubovits for explaining some of his related research to me, and for his advice in optics. Finally, I also owe a very large thank you to my awesome girlfriend, Corinne Côté, for keeping me healthy and sane throughout my studies.

Contents

List of Figures

Notations and conventions

The following notations are used throughout this thesis:

ET	Electron transfer
R. sphaeroides	*Rhodobacter sphaeroides*
RC	Reaction Center
BRC	Bacterial Reaction Center
cyt c	Cytochrome c (electron donor protein)
cyt c_2	Cytochrome c_2 (BRC's native secondary electron donor)
WT	Wild Type (native strain of R. *sphaeroides*)
R − 26	Carotenoidless strain of R. *sphaeroides*
BChl	Bacteriochlorophyll
BPheo	Bacteriopheophytin
UQ_{10}	Ubiquinone Q_{10} (native quinone of the BRC)
P	Bacteriochlorophyll dimer cofactor of the BRC
B	Bacteriochlorophyll monomer cofactor of the BRC
B_A, B_B	Active B cofactor, inactive B cofactor
H	Bacteriopheophytin cofactor of the BRC
H_A, H_B	Active H cofactor, inactive H cofactor
Q	Quinone cofactor of the BRC

Q_A, Q_B	Primary quinone, secondary quinone
PDB	Protein Data Bank (http://www.rcsb.org)
LDAO	Lauryldimethylamine N-oxide
$TX-100$	Triton X-100, or polyethylene glycol p-(1,1,3,3-tetramethylbutyl)-phenyl ether
DOPC	1,2-dioleoyl-sn-glycero-3-phosphocholine
DOPG	1,2-dioleoyl-sn-glycero-3-[phospho-rac-(3-lysyl(1-glycerol))]
DOTAP	1,2-dioleoyl-3-trimethylammonium-propane
BTP	Bis Tris Propane, or 1,3-bis(tris(hydroxymethyl)methylamino)propane
Tris	Tris(hydroxymethyl)aminomethane
CAPS	N-cyclohexyl-3-aminopropanesulfonic acid
EDTA	Ethylenediaminetetraacetic acid
TEN	Solution of Tris-HCl, EDTA, NaCl
$TL^{0.X}E$	Dispersion of Tris-HCl, 0.X % LDAO, EDTA; where X varies from 0.03 to 0.1
$TL^{0.1}$	Dispersion of Tris-HCl, 0.1% LDAO
UV	Ultraviolet light
VIS	Visible light
NIR	Near infrared light
K_D	Dissociation constant
DAD	2,3,5,6-tetramethyl-p-phenylenediamine

1

Introduction

1.1 Overview of photosynthesis

Photosynthesis is the process utilized by living organisms to convert solar energy into metabolizable chemical energy. It is thus the primary energy production process for nearly all life on Earth, with the high-energy molecules produced from this process fueling not only phototrophs themselves, but also other organisms which feed on them, and the non-dietary energy needs of humans in the form of fossil fuels generated by the anaerobic decomposition of these phototrophs over millions of years.[1] Furthermore, our oxygen-rich atmosphere, needed for the high energy yield metabolic process of cellular respiration that virtually all complex lifeforms rely on, is due to the oxygen byproduct formed during photosynthesis.[2] Despite the huge number and variety of organisms which utilize this process, the enzyme that performs the earliest steps of energy conversion in photosynthesis is remarkably conserved. This enzyme is a pigment-protein complex known as the reaction center (RC), and all RCs can be organized into two groups: those that produce oxygen (oxygenic), and those that do not (anoxygenic). The more primitive anoxygenic RC is found in purple non-sulfur bacteria and is termed as the bacterial reaction center (BRC). This protein complex relies on the cyclical transfer of electrons between itself and nearby proteins to drive its function. The more complex oxygenic RC of cyanobacteria and plants is known as photosystem II (PSII). This complex is able to use water as an electron source, freeing it of the need to re-cycle electrons, and allowing it to utilize electrons and photons of much higher energies. In spite of their differences in function, these RCs are structurally very similar, with the most striking difference being the presence of a manganese-calcium complex in PSII. This complex catalyzes the oxidation of water, leading to its splitting into hydrogen and oxygen. It is thus known as the oxygen-evolving complex (OEC).

The last common ancestor of the modern BRC and PSII has been proposed to be an anoxygenic RC, most likely very similar to the modern day BRC.[3,5] This evolution from anoxygenic

to oxygenic RCs likely occurred between 2.8 and 2.2 billion years ago.[3–5] The structural similarities of the current-day BRC and PSII suggest that this happened by the incorporation of a transition metal complex,[6,7] however, the details of this evolutionary transition remain unknown. In this work we provide evidence of manganese binding and oxidation in native BRCs which suggest that utilizing manganese may have preceded the genetic modification that ultimately resulted in highly oxidizing reaction centers capable of splitting water.

1.2 Reaction center structure and function

1.2.1 Comparison of structures

X-ray crystallography has enabled a complete atomic picture of both the BRC and the PS II at a resolution of up to 1.9 Å.[8,9] Both the inner core of PS II and the BRC are membrane protein complexes of ~100 kDa, comprised of multiple subunits and having an approximate 2-fold symmetry along a central axis normal to the membrane (see Figure 1.1). The two main subunits, L and M in the BRC, and D1 and D2 in the PS II, each contain five membrane-spanning α helices. While the PSII has many other subunits surrounding its core, the BRC has only one other subunit, H. It is globular in form, and consists of short beta sheets and an α helix, capping the cytoplasmic side of the L and M subunits.

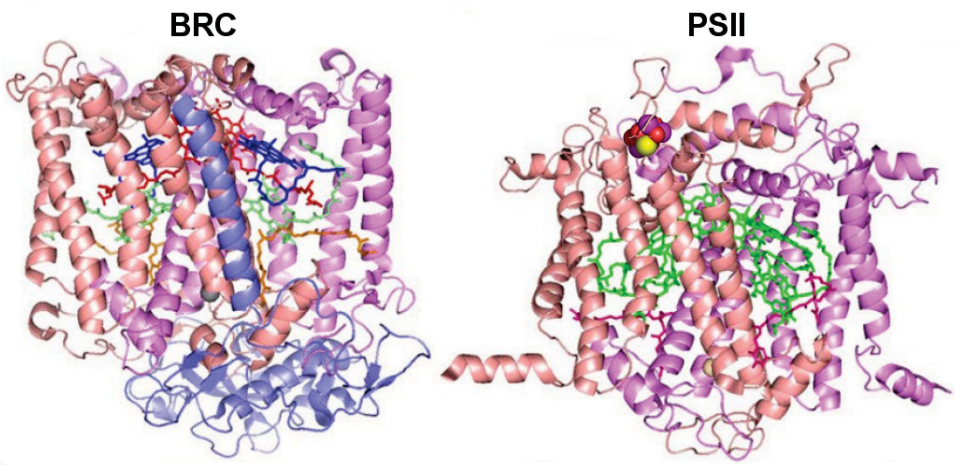

Figure 1.1: Structural similarity of BRC and PSII. The BRC subunits are colored pink, salmon, and blue, for L, M, and H, respectively. The cofactors are red, blue, green, and orange, for P, B, H, and Q, respectively. The D1 and D2 subunits of PSII are colored similarly to the BRC, however all cofactors are colored green, except for the Qs, which are colored red. The OEC is also depicted as spheres, and colored by atom: purple, red and yellow, for Mn, O, and Ca, respectively. The central iron atom is also pictured as a sphere, and is colored grey in the BRC, and beige in PSII. The quasi two-fold symmetry axis is vertical relative to the displayed images, going through the center of the proteins. Images were created from atomic coordinates of previously resolved structures that have been published in the Protein Data Bank (PDB). Coordinates for the above images are from PDB codes 4RCR and 3WU2 for BRC and PSII, respectively.

The cofactors of the two photosystems are also similar and follow the same 2-fold symmetry, with pairs along the two main subunits. In the BRC from the periplasmic surface going down (top to bottom in Figure 1.1), this includes a dimer of bacteriochlorophylls (P), followed by a bacteriochlorophyll monomer (B), a bacteriopheophytin (H), and a quinone molecule (Q). There is also a single divalent iron atom found closer to the cytoplasmic surface of the BRC. PS II has a similar arrangement of cofactors, with the bacteriochlorophylls (BChls) and bacteriopheophytins (BPheos) being replaced by chlorophylls and pheophytins, and having different quinones. In addition the OEC is also located in this core, along the lumenal surface, near P (colored spheres in Figure 1.1). This complex consists of one calcium, five oxygen and four manganese atoms.

1.2.2 Electron transfer in the bacterial reaction center

The overall mechanisms of charge transfer in both BRC and PSII have been studied in great detail and are generally well understood. For a review see text by Ke.[10] The charge transfer cycle of the BRC is illustrated in Figure 1.2. Upon photo-excitation of the BRC, P acts as the primary electron donor. The electron is transferred to H of the L subunit (H_A) with the aid of the nearby B (B_A) in ~3 ps. It is rapidly transferred further to a nearby quinone molecule in the M subunit, referred to as the primary quinone (Q_A), in ~200 ps, and finally transferred to the quinone in the L subunit, the secondary quinone (Q_B), via a slower, conformationaly gated process, taking from 6 to 150 μs. The BChl monomer and BPheo of the M subunit are not active in the main photosynthetic function of the BRC, and likely serve as excitation quenchers, protecting overly excited RCs from prolonged exposure to the free radicals created from charge separation.[11,12] Electron transfer along the cofactors of PS II follows a similar pathway, but with many more steps involved in the complete transfer, including those on the donor side, involving the OEC, and those on the acceptor side, involving the transfer to the next photosynthetic apparatus.

In the BRC, the oxidized P is then reduced by a secondary electron donor protein, cytochrome c_2 (cyt c_2), with the electron transfer (ET) occurring in 1 - 10μs. This allows a second reduction of Q_B, which includes an uptake of two protons to produce the doubly protonated, doubly reduced quinol (QH_2). QH_2 is weakly bound to the Q_B binding site, and is replaced by an oxidized quinone from the membrane's quinone pool. It will then diffuse to another membrane pigment-protein complex, the cytochrome bc_1 complex, where it will be oxidized, releasing its protons to the periplasmic side of the membrane. This creates a proton concentration gradient across the membrane, which is used for ATP synthesis. The full transfer process is much more complex for PS II. The two electron, two proton gate mechanism of Q_B is similar, but the following transfers on the acceptor side are much more numerous and not relevant to the current study. However, the donor side reactions are worth summarizing. The oxidized P is reduced by a high potential tyrosine residue, which is in turn reduced by the manganese ions

of the OEC. The OEC is able to store four reduction equivalents from the oxidation of two water molecules. These doubly oxidized water molecules will then split into molecular oxygen and protons, which are released as byproducts.

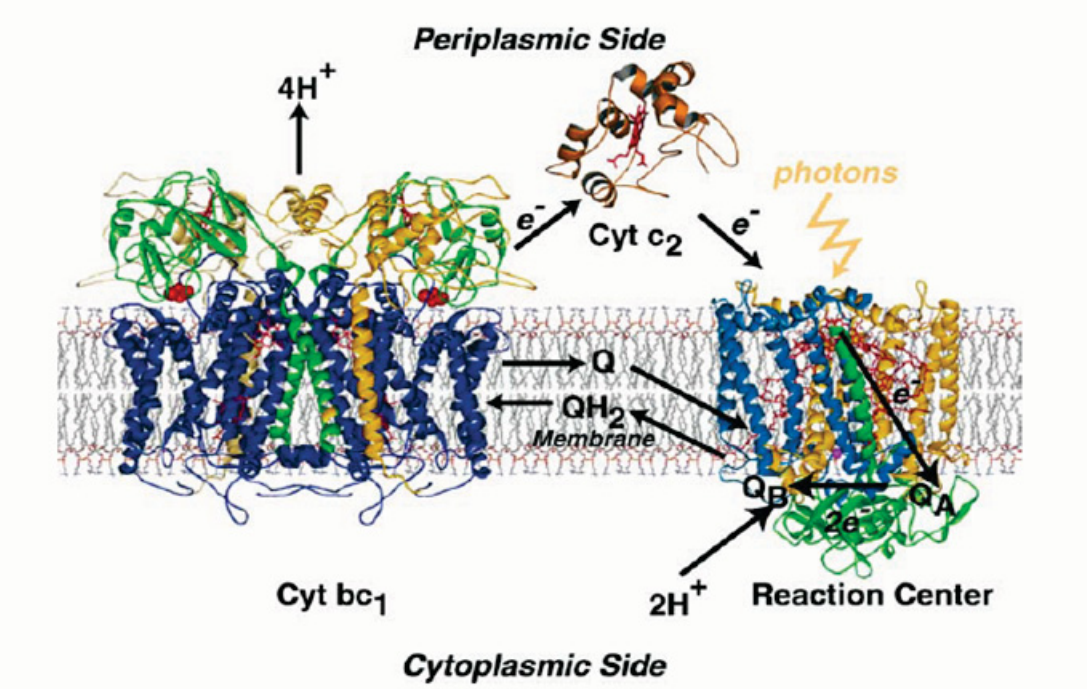

Figure 1.2: Charge transfer circuit of bacterial photosynthesis. Electron and proton transfer in the native membrane between the BRC, neighboring cytochrome bc_1 complex, and cytochrome c_2. See text for details. Figure reproduced with permission from Axelrod et al.[13]

A great engineering accomplishment of these photosynthetic apparatuses is their nearly perfect efficiency of energy and charge transfer.[14] This efficiency, in fact, makes this process the most energy efficient process in Nature. The key to the low-loss of these processes is the uni-directional nature of the electron transfer. This is accomplished through transfer rates which are orders of magnitude more rapid in the forward direction than the reverse. A map of these transfers in the BRC, and their competing back reactions can be seen in Figure 1.3. While the identities and rates of individual ETs in PSII differ slightly, the overall mechanism of uni-directional ET is the same.[14]

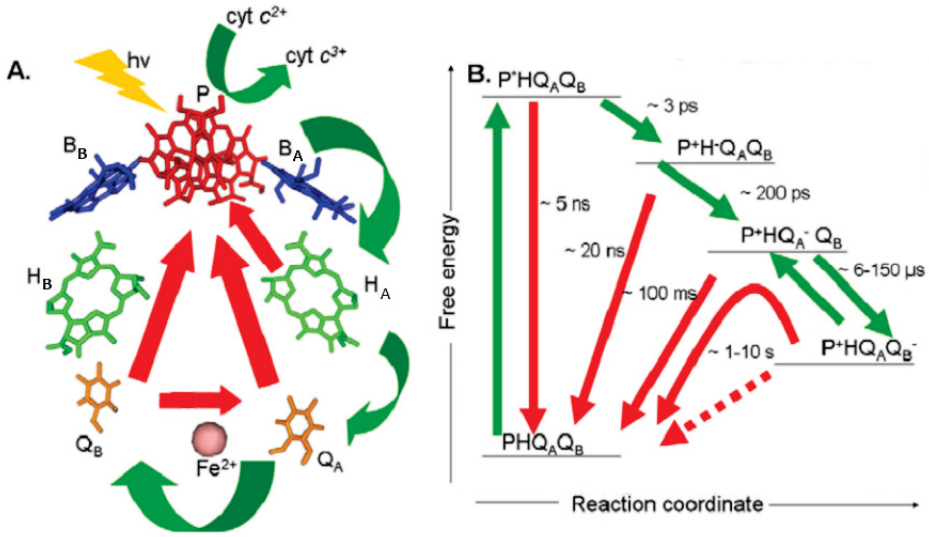

Figure 1.3: Forward and reverse electron transfer in the BRC. A: molecular electron transfer pathway. Green arrows show forward direction and red arrows show reverse direction. Phytyl and isoprenoid chains of the cofactors have been truncated for clarity. B: free energy diagram of the various excited and charge-separated states, along with their forward and reverse rate electron transfer constants. Figure reproduced with permission from Deshmukh.[15]

1.2.3 Interaction of the bacterial reaction center with its environment

In order to unravel the energetics and kinetics of the electron and proton transfer in RCs it is often necessary to isolate them from their natural membrane environment, with many neighboring proteins and molecules. This is especially true for optical techniques, as measurements will be strongly affected by the presence of surrounding light harvesting complexes. As RCs are membrane proteins they have a large hydrophobic region, which is not soluble in water. Their native membrane is, therefore, typically replaced by a simpler substitute. In this study we examine BRCs which have had their natural membrane replaced by a homogeneous detergent or lipid environment. Detergent molecules form a micellar belt around the hydrophobic section, consisting of a layer of single molecules with their hydrophobic chain pointing towards the midsection of the BRC and the polar head forming the outer surface which reacts with the solvent. Lipids, on the other hand, form a liposome incorporating several BRCs, and consist of a bilayer with hydrophobic tails pointed inwards and polar headgroups forming the inner and outer surfaces of the liposome shell (see Figure 1.4).

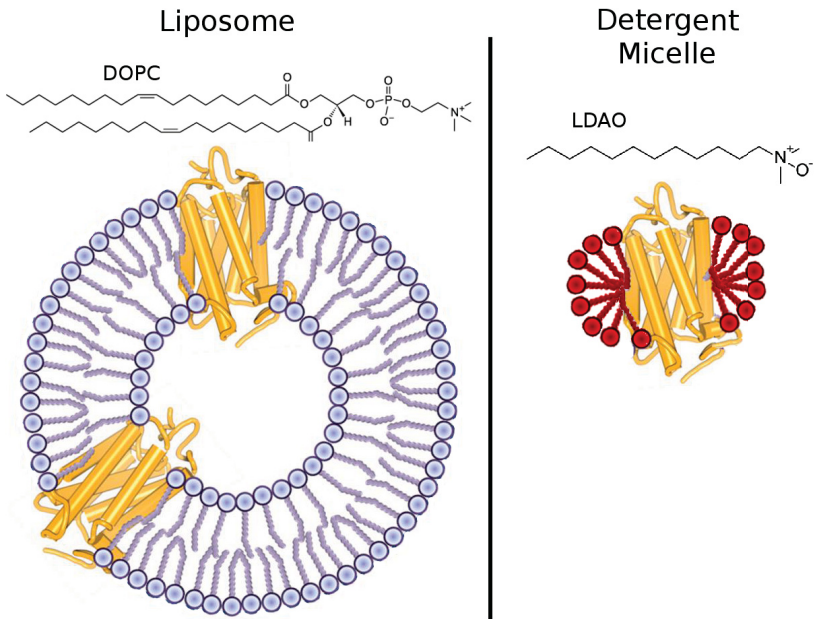

Figure 1.4: Lipid and detergent membrane substitutes of membrane proteins. Top shows chemical structure of typical detergent and lipid molecules (LDAO and DOPC, respectively). Bottom shows a 2D diagram of the protein-membrane substitute configuration. The membrane protein is depicted orange, while lipids are colored blue and detergent molecules colored red.

The type of membrane substituent has been shown to have significant effects on the function of the BRC.[16,17] This can be due to differences in hydrophobic thickness between the membrane substitute and the protein, causing changes in the structure of both the protein and nearby membrane substituent molecules.[18,19] It can also be due to a difference in the environment provided to the cofactors by the different surfactants.[20] Additionally, for liposomes the headgroup charge of the lipid will dictate the curvature and packing density of the the liposome, as charged headgroups will suffer an electrostatic repulsion not present with neutral lipids (see Figure 1.5). This has been found to affect accessibility of Mn ions to the liposome-solubilized BRCs, as charged headgroup liposomes were observed to be more accessible for Mn ions than neutral ones.[20]

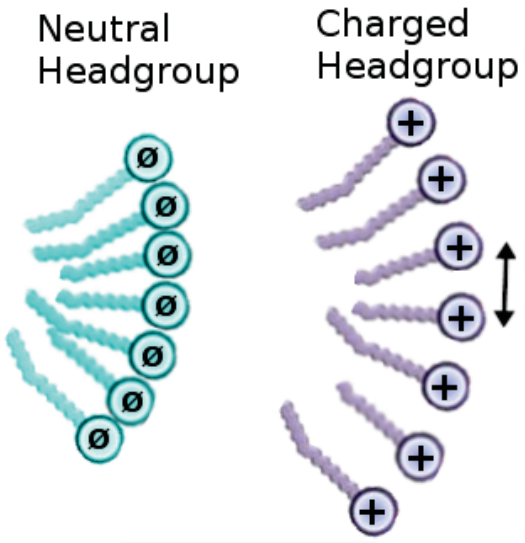

Figure 1.5: The effect of lipid headgroup charge on liposome packing density. Charged headgroups suffer electrostatic repulsion between neighbors, reducing the packing density relative to neutral lipids.

Once the BRC has been removed from its natural membrane environment it no longer has access to the pool of quinone molecules residing in this membrane. It is therefore necessary to add excess quinone if a functioning quinone cycle is desired. The same is true for a secondary electron donor. Without the cytochrome bc_1 complex present to reduce cyt c, a large excess of reduced cyt c or other secondary electron donor must be added. Alternatively, a smaller amount of secondary electron donor, along with an excess of reducing agent can be used.

1.3 Optical spectrum of the BRC

A powerful tool in the study of the RCs is optical absorption spectroscopy. It is particularly useful, as the differences in structure and conjugation of the various electron transport cofactors, along with differences in the dielectric constants of their environments, has lead to clearly separated optical absorption bands of several electronic transitions. This is true for electronic excitations along the Q_x and Q_y dipoles of both the BChls and the BPheos (see Figure 1.6 for BChl, BPheo has similar dipole orientations with respect to the tetrapyrrole ring). For these excitations the high conjugation of these molecules greatly lowers their band gap, taking them from the typical ultraviolet (UV) energy levels to visible (VIS), and even near-infrared (NIR) energy levels. The Q_x transition dipole goes from the ring 4 to ring 2, and has absorption bands in the VIS, at ~600 nm and ~540 nm for BChl and BPheo, respectively. The Q_y transition dipole goes from ring 1 to ring 3 and has absorption bands in the NIR, with a BPheo absorption band at ~760 nm. The greater degree of conjugation of the dimer, spanning the two tetrapyrrole rings, shifts the BChl band to lower energy than the monomer, with

the absorption band of P at ~865 nm, and that of B at ~800 nm (for a review see the paper by Clayton[21]). As the absorption bands corresponding to excitations along the Q_y transition dipole of the BChl dimer and monomer, and the BPheo are studied and discussed extensively in this work, we will refer to them as the P band, B band, and H band, respectively.

While these are the most useful absorption bands for our purposes, additional bands are present including the Soret band between 350 - 400 nm, due to excitations of the porphyrin macrocycle of these pigments, and the UV bands around 280 nm and below, due to excitations of amino acids with aromatic rings.

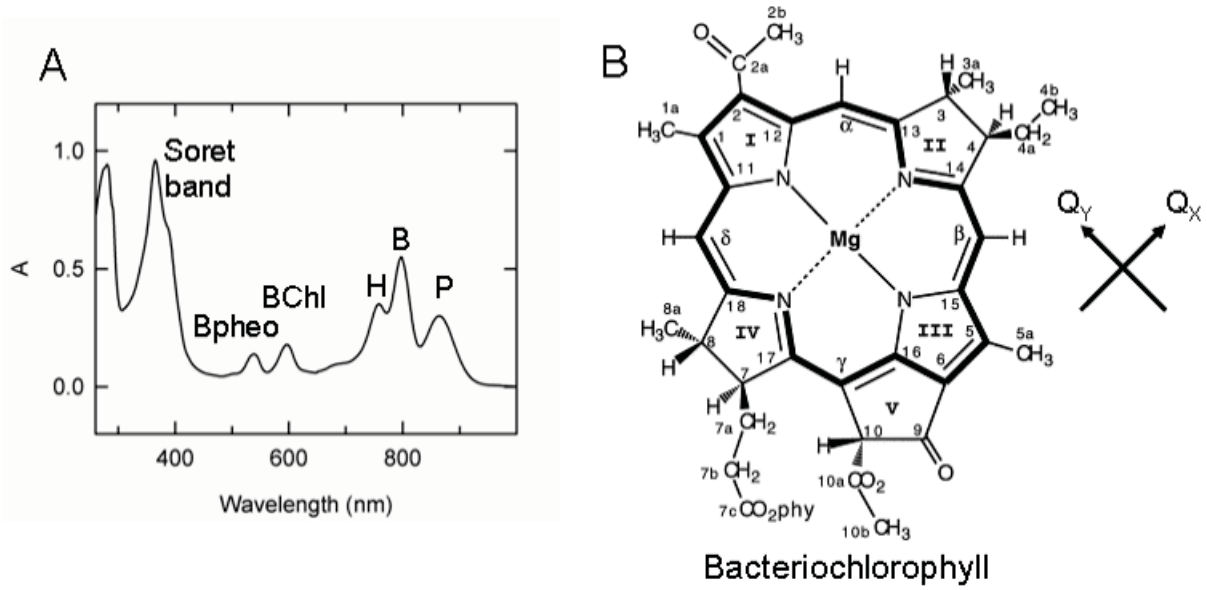

Figure 1.6: Electronic transitions in the BRC and their molecular origin. A: UV-VIS-NIR optical absorption spectrum of the BRC. The UV consists of both bands of aromatic amino acids, and bands of excitations of pigments porphyrin macrocycles (the Soret band). In the Vis, excitations along the Q_x dipole are visible, with spectral resolution between bands of BChl and BPheo. Excitations along the Q_y dipole are observed in the NIR, with spectral resolution of not only the BChls and BPheos bands, but also the P and B bands. B: structure of BChl showing the directions of the Q_x and Q_y transition dipoles (arrows) and the porphyrin macrocycle (bold). Figure reproduced with permission from Deshmukh.[22]

Upon absorption of a photon, charge separation quickly occurs with the transfer of an electron from P to Q, establishing a local electric field across the RC between these cofactors. The effects of the electric field on the cofactors, along with the oxidation of P, cause observable effects on the absorption spectrum of the BRC. These effects can take the form of shifts in absorption band position, due to a change in polarizability of the molecule, broadening or narrowing of the band, due to a change in strength of the transition dipole moment, or bleaching of the band, if the effects are so great that they drastically change the energy of the excitation.[23] Figure 1.7 demonstrates these effects by showing the spectrum before and after each change,

along with the difference spectrum.

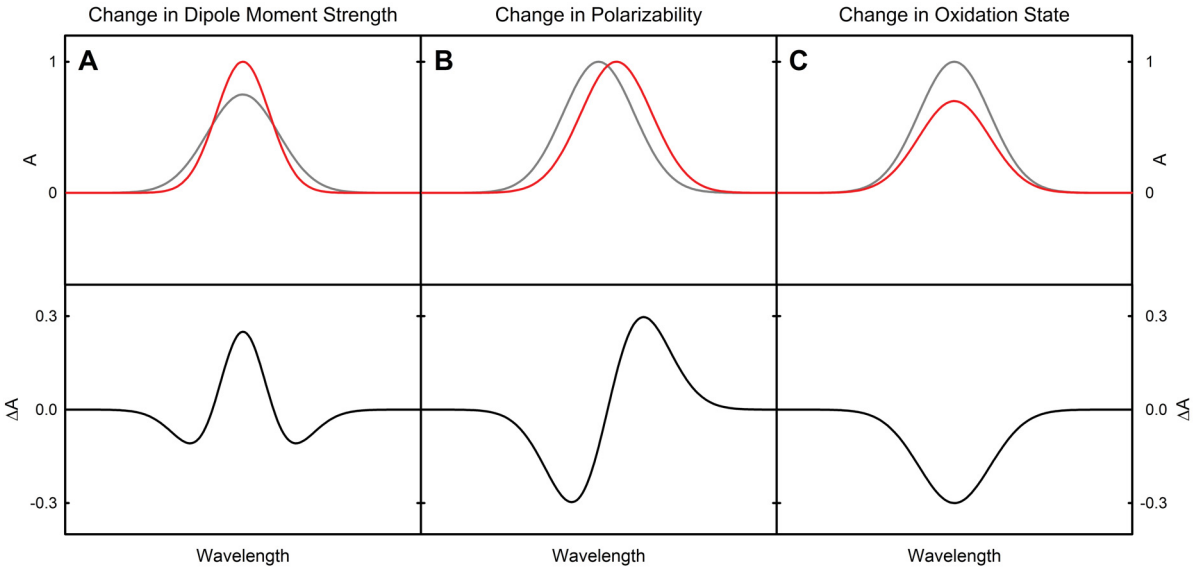

Figure 1.7: Demonstration of electrochromic and oxidative changes on absorption spectra. A: narrowing of an absorption band due to the strengthening of the moment of the transition dipole. B: the shift of an absorption band due to a change in polarizability of the of the absorbing molecule. C: the bleaching of an absorption band due to a change in oxidation state. Grey traces denote initial spectra, red traces denote final spectra, and black traces on lower graphs denote difference spectra.

The effects of charge separation on the absorption spectrum of the BRC can be most easily tracked in the NIR spectrum. The oxidation of P completely removes the absorption band at 865 nm due to excitation along its Q_y dipole. The presence of the electric field, however, only slightly shifts the energy levels of the Q_y excitations, causing a red shift of the H band, and blue shift of the B band,[25] as seen in Figure 1.8 A and B. Taking the difference spectrum between before and after illumination highlights these spectral changes (panel B), and is known as the light minus dark (light - dark) spectrum. As in this case the charge separation is between P and Q_A or Q_B, this state of the BRC is known as the P^+Q^- state.

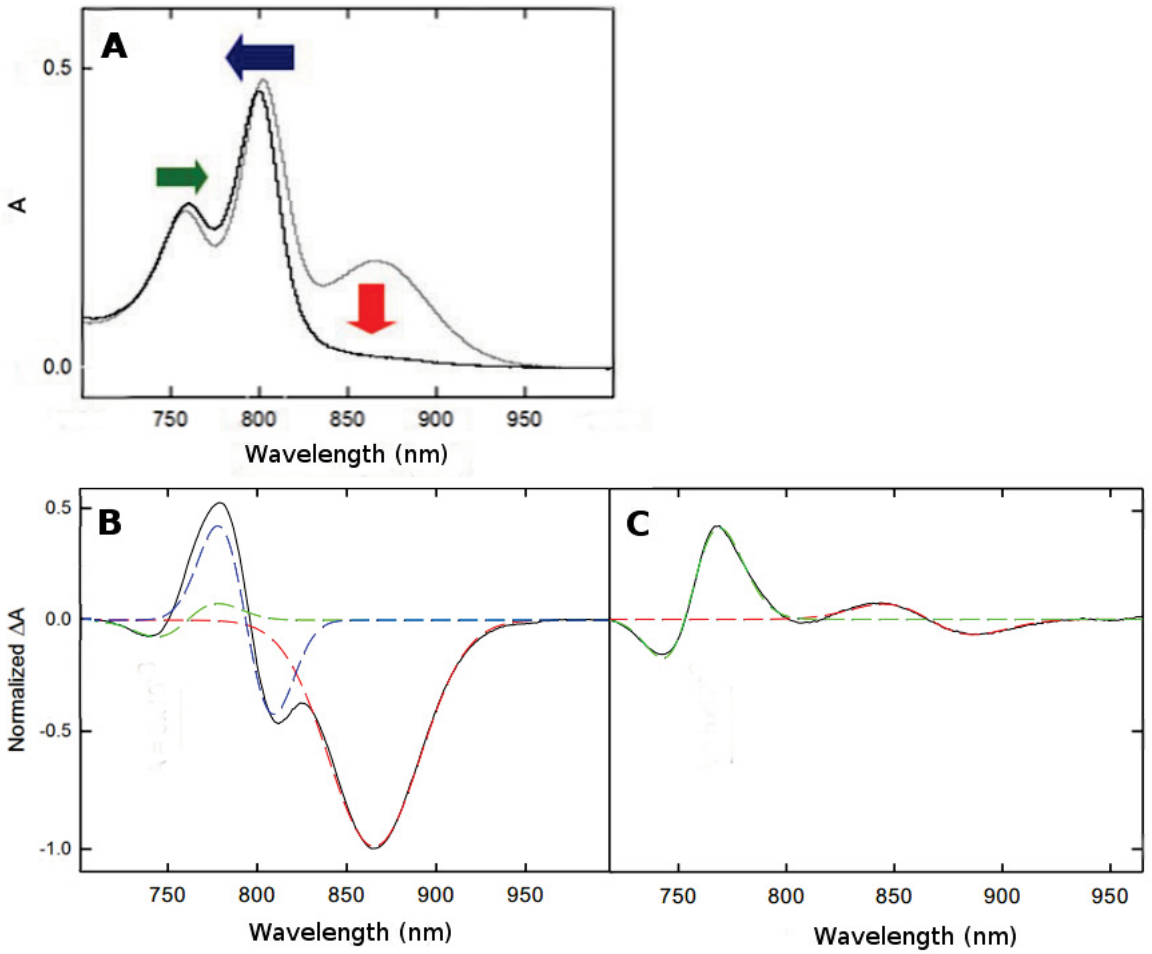

Figure 1.8: Effect of charge separation on Q_y absorption bands. A: dark-adapted spectrum of the Q_y bands of the BRC is shaded gray, and the spectrum recorded during light excitation is shaded black. Illumination triggers the transfer of an electron from P to Q_B, or Q_A if no Q_B present, (creating the P^+Q^- state) which in turn effects these bands. Colored arrows demonstrate the specific effects on each pigment, namely the bleaching of the P band, the blue shift of the B band, and the red shift of the H band. B: the light - dark difference spectrum corresponding to the spectra shown in panel A. The spectrum is decomposed into the individual effects of each band (dashed lines), with colors matching the arrows of panel A. C: when a secondary electron donor is present (cyt c^{2+} in the above spectrum), it will re-reduce P leaving only the negative charge on the quinone (Q_B in the above spectrum) to effect the absorption bands. The resulting light - dark spectrum is similar to that of the P^+Q^- state, but without the blue shift of B, and with the bleaching of the P band being replaced by a small blue shift.

If the oxidized dimer (P^+) is then returned to its neutral state through re-reduction by a secondary electron donor, the remaining electric field due to the negatively charged Q has a similar, though diminished effect on the Q_y absorption bands. While the red shift of the H band is similar, the blue shift of the B band is absent, as the corresponding transition dipole is perpendicular to the ring of Q. The P band is no longer bleached, as it is in a neutral state, but it does have a small blue shift due to the charge on Q (see Figure 1.8 C).[26] This state of

the BRC is known as the PQ^- state. Unlike the recovery of the P^+Q^- state, which takes ~1s in isolated BRCs (see Figure 1.3) and occurs through charge recombination, recovery of the PQ^- state requires the reduced quinone to salvage an electron acceptor from its surroundings, and thus takes much longer with a time constant of minutes and depending on environmental conditions.

As the absorption bands of the various cofactors are well separated, and there are strong changes in these bands associated to electron transfer, these changes can be tracked in time to determine the rates of various electron transfer processes.

1.4 Research perspective

1.4.1 Previous advances

Over the past two decades much work has been done attempting to model the transition from anoxygenic to oxygenic photosynthesis. Some of this took the form of recreating changes in the BRC similar to those that would have had to occur in ancient anoxygenic RCs in order to be able to incorporate transition metals into the electron transfer chain. Over this time significant progress has been made in addressing the various obstacles ancient RCs would have had to overcome in an evolutionary context. Here we will review some of the most relevant results to this study. These studies modeled this transition by either creating mutations which lead to the BRC being able to oxidize higher potential electron donors, or attempting to lower the oxidation potentials of these donors to within reach of P^+.

1.4.1.1 Utilizing manganese as an electron source in mutant BRCs

Via 3 successive mutations, the P/P^+ potential of the BRC was elevated from ~500 mV to up to ~770 mV, high enough to be able to oxidize high-potential (~750 mV) tyrosine residues, analogous to the electron transfer chain of PSII.[27] These high-potential mutants were created by substituting in positively charge amino acids for neutral ones in the vicinity of P. This created additional hydrogen bonds between P and surrounding amino acid residues of the BRC, which was found to increase the stability of the charge-neutral ground state (P), and elevate the P/P^+ potential by 60 - 125 mV per hydrogen bond. Similar mutants were later found to be able to oxidize bicarbonate coordinated manganese in solution.[29] This was accomplished by lowering the Mn^{2+}/Mn^{3+} potential, first by coordinating manganese with bicarbonate, and then by elevating the pH, further lowering the Mn^{2+}/Mn^{3+} potential to ~620 mV, well below that of the elevated P/P^+ potential. However, a very low affinity between the BRC and Mn in solution was observed, leading to low-yield electron transfer. With additional mutations a

Mn binding site was designed near P, yielding 1st order ET* from a bound Mn^{2+} to P^+.[28] Here amino acid residues with carboxylic acid groups were added to bind Mn in a location not far from the analogous Mn binding site of PSII. While these mutants allowed 1st order ET from Mn to the BRC with rate constants up to 90 s^{-1}, a total of 6 mutations were needed.

1.4.1.2 Utilizing manganese as an electron source in native BRCs

The incorporation of manganese was also attempted with native BRCs, by changing only manganese coordination and environmental factors. Bicarbonate coordination of manganese, similar to that used with mutant BRCs earlier, showed signs of Mn interacting with the BRC. Here the rate of P^+ recovery was accelerated for BRCs in the presence of manganese bicarbonate after illumination was turned off.[30] Direct evidence of ET from manganese to P^+, however, was not observed. By using higher concentrations of bicarbonate, the Mn^{2+}/Mn^{3+} potential was found to be reduced to ~520 mV. Although this potential is still greater than that of unmodified P/P^+ (~500 mV), it was close enough to observe electron transfer from this new complex to P^+, though with a very low yield.[31] Manganese coordinated by bis tris propane (BTP) was also found to interact with the BRC at pH 8. It did so by blocking light-induced conformational changes in the vicinity of P, and by elevating the P/P^+ potential from ~500 mV to ~600 mV, likely due to the binding of this complex to the BRC.[22] Increasing the pH to 9.4 was found to have the additional effect of drastically lowering the Mn^{2+}/Mn^{3+} potential below that of P/P^+, and allowing the reduction of P^+ by this complex.[24] This low manganese potential at high pH is likely due to the deprotonation of the second amine group of BTP, providing an additional ligand with which to coordinate manganese.

1.4.2 Motivation

The evolution to oxygenic photosynthesis occurred through the incorporation of a transition metal complex by anoxygenic RCs, which then evolved the molecular machinery necessary to use these transition metals to catalyze the splitting of water and the harvesting of the resulting high-energy electrons. This transition is one of most significant events in the history of life on Earth, with its repercussions being felt by the oceans, the atmosphere, and nearly all life on the planet. Understanding the mechanism of this transition is not only important for our knowledge of Earth's history, but it could also prove useful in the development of hydrogen production for our future energy needs. The hydrogen fuel cell is an energy storage technology that has been heavily developed over the last couple of decades, showing potential for use in both low-emission transportation, and stationary power distribution applications.[32,33]

*A 1st order ET is defined as an ET where the rate of the formation of the products is linearly proportional the the activity of the reactants, ie: $\frac{d[B^-]}{dt} \propto [A]$ for the ET: $A + B \rightleftharpoons A^+ + B^-$. This can occur when there are no external factirs needed for the transfer to take place, such as conformational changes, protonation, etc., and diffusion is not a limitation (in our case this means Mn^{2+} is bound near P^+).

The largest barrier to adoption of this technology is the clean, efficient generation of hydrogen. Currently ~95% of hydrogen gas is produced with fossil fuels in processes that have high greenhouse gas emissions.[34] However the development of an efficient, zero-emissions form of hydrogen production could provide humanity with a renewable energy source usable in both stationary and transportation applications, unlike current battery technology, which does not have sufficient energy density for widespread adoption in transportation. Such a form of production could be similar to the process of oxygenic photosynthesis, using solar energy to split water, and then finding another method to combine the liberated protons into molecular hydrogen. Much work is underway to develop such "artificial leaf" systems. While the majority of the research and development has been focused on using synthesized electrodes to catalyze the splitting of water and generation of hydrogen, these methods generally require harsh organic solvents, rare materials, and are currently stuck at 14% efficiency.[35] Therefore a biomimetic approach, such as PSII's method of proton generation through oxygenic photosynthesis, coupled to hydrogenase enzymes producing molecular hydrogen from these protons, could provide a more appropriate alternative.[36] This method would likely involve plentiful, non-toxic materials, and be cheap to produce. Importantly, an understanding of the pathway nature took to solve the water-splitting problem could lead to much needed advances in such an approach.

Despite the importance of this transition, the details of these early steps of the evolutionary process remain unknown. We propose the hypothesis that anoxygenic BRC-like RCs were exposed to an environment where a fitness advantage existed for the incorporation of a manganese complex into the donor-side electron transfer chain. The simplest way this could happen would be for the manganese complex to act directly as the secondary electron donor to P^+. This provides a more likely transition than one which relies on multiple simultaneous mutations before manganese could be used by the RC, and any fitness advantage is gained. Of the aforementioned studies, the incorporation of a BTP coordinated manganese by native RCs currently holds the most promise. In this case rapid electron donation by Mn was observed with no loss of stability of the BRC, and no need for mutations. We have, therefore, focused this work on extending this study. Specifically, we better resolved the binding, ET rates, and other interactions between the Mn-BTP complex and the BRC, along with identifying the manganese composition of the Mn-BTP complex. This not only allow us to evaluate whether this system provides a feasible evolutionary mechanism to the anoxygenic-oxygenic photosynthesis transition, but also could provide insight to a possible biomimetic solution to the hydrogen generation problem.

2

Materials and Methods

2.1 Bacterial growth of *R. sphaeroides*

Cell growth and BRC protein purification was performed for two strains of *R. sphaeroides,* Wild Type (WT) and R-26, a carotenoid-less mutant induced by environmental stesses. This was done following the protocol of Feher and Okamura.[37] First bacterial growth media was prepared immediately before use. The media was then bottled in 1 L Pyrex bottles and autoclaved for 1 hour at 121 °C in a SV-12 scientific pre-vacuum sterilizer. Once cooled to room temperature, the bottles were inoculated with approximately 110 mL of fully grown bacteria stored from previous growths. The inoculations were performed on a sterilized bench with an electric burner nearby to further assure no contamination occurred.

After inoculation the bottles were kept in the dark for 6 hours to promote the anaerobic metabolism of any oxygen in the media. The bacteria were then grown for 2 days in a chamber with 6 60 W tungsten light bulbs and reflective siding. Incandescent lighting was chosen for its wide spectrum, covering the visible and near infra-red light that R. *sphaeroides* utilizes.

Once fully grown, the bacteria were centrifuged in a Beckman J2-HS centrifuge with a JA-10 rotor at 7000 rpm, and 4 °C for 20 minutes. This combination generates 7000 g's of force. The supernatant was then discarded, and the cells were collected, weighed, and stored at -20 °C.

Details on the preparation of the solutions used for bacterial growth media are as follows:

- Growth Media: 4 g of casamino acids, 4 mL of vitamin solution, 80 mL of concentrated base, 40 mL of 20 % potassium succinate solution, 80 mL of 1M phosphate buffer, and 25 mL of ammonium sulfate solution were added to distilled water for a final volume of 4 L.
- Vitamin solution: 2 mg of biotin, 50 mg of sodium bicarbonate, 100g of nicotinic acid, 50 mg of thiamine-hydrochloride, and 100 mg of para amino benzoic acid were mixed

together in distilled water to a final volume of 100 mL. The solution was boiled until all ingredients were dissolved. It was then autoclaved for 1 hour at 121 °C, and cooled for storage.

- Concentrated Base: 20 g of nitrilotriacetic acid and 12 g of potassium hydroxide were mixed in 1 L of distilled water with a magnetic stirrer for 20 minutes. This was allowed to sediment, and then the supernatant was recovered. To this 58 g of magnesium sulfate heptahydrate, 6.8 g of calcium chloride dehydrate, 4 mL of ammonium molibdenate solution, 200 mg of ferrous sulfate heptahydrate, and 100 mL of metals 44 solution were added. The ammonium molibdenate was added 1 mL at at time, waiting for it to completely dissolve after each addition. The final volume was adjusted to 2 L and the pH was slowly adjusted to 6.7 using 5 % m/v KOH at a rate of 2 mL per minute.
- Metals 44 solution: 200 mg of ethylenediaminetetraacetic acid (EDTA), 1.1 g of zinc sulfate heptahydrate, 500 mg of ferrous iron sulfate heptahydrate, 150 mg of manganous sulfate monohydrate, 40 mg of cupric sulfate pentahydrate, 20 mg cobalt chloride, 12 mg boric acid, and 150 μL of 6 N sulfuric acid were mixed in distilled water to a final volume of 100 mL. One can tell when the solution is properly prepared as it turns from green to yellow, and finally amber weeks later.
- 20 % Potassium succinate solution: 200 g of succinic acid was added to 250 mL of distilled water. To dissolve this, a separate beaker of 200 g of potassium hydroxide was dissolved in another 250 mL of distilled water and allowed to cool. With the succinic acid beaker in an ice water bath, the potassium hydroxide solution was slowly added. The final pH was then adjusted to between 6.8-7.0 with HCl, and the final volume was brought to 1 L with distilled water.
- 1 M Phosphate buffer: 274 g of dibasic potassium phosphate trihydrate was added to 1.2 L distilled water. This in turn was slowly added to a solution of 136 g of monobasic potassium phosphate in 800 mL of distilled water. The final pH was adjusted to 7.0 and the final volume adjusted to 2 L.
- 10 % Ammonium sulphate: 50 g of ammonium sulfate was dissolved in 470 mL of distilled water. The pH was adjusted to 7.0 with ammonium hydroxide, and the final volume was adjusted to 500 mL.

All solutions were stored at 4 °C.

2.2 BRC isolation

BRCs in detergent micelles were next isolated from the frozen cells. First 100 g of the frozen cells were suspended in 200 mL of distilled water and 2 mL of 1 M Tris by stirring for approx-

imately 1 hour, until a homogeneous dispersion was attained. After this 2 mL of EDTA, 1.25 g of NaCl, and 1.7 mL of LDAO detergent were added and the mixture was sonicated in a Mandel Scientific XL2020 ultrasound processor in order to lyse the cells. This was done in an ice bath for 40 minutes in intervals of 10 s on and 10 s off in order to avoid thermal degradation of the cells. Once the cells are lysed the BRC became photosensitive and care was taken to limit light exposure in all following steps. The sonicated dispersion's volume was next brought to 210 mL and poured into 8 polycarbonate tubes for ultracentrifugation in a Beckman Optima XL-100K ultracentrifuge with a Ti-70 fixed angle rotor at 45 000 rpm. This combination generates a force of 200 000 g's and was used for 2 hours at 4 °C. The pellet was then collected and resuspended in 205 mL of buffer containing 15 mM Tris-HCl, 1 mM EDTA, 0.1 M NaCl (TEN), and finally 4.66 mL of LDAO. This was left to stir for 10 minutes at room temperature before ultracentrifuging again with the same parameters as the first round. Crude BRCs in detergent micelles were now in the supernatant. These were then precipitated by mixing 72 g of ammonium sulfate and 7.3 mL of 30 % LDAO in 220 mL of supernatant, stirring for 15 minutes at room temperature, and centrifuging in the Beckman J2-HS centrifuge with a JA-17 rotor at 10 000 rpm (10 000 g's) and 4 °C for 15 minutes. The BRC micelles were then re-suspended in TEN buffer and dialysed overnight in 15 mM Tris-HCl, 0.1% LDAO, and 1 mM EDTA ($TL^{0.1}E$) to remove the ammonium sulphate. Dialysis membranes with a molecular weight cut off (MWCO) of 12-14 kDa were used. For samples where active secondary quinone was desired, 30 μM of UQ_{10} was added to the BRCs for every dialysis bath.

The BRC micelles were further purified to remove antennae complexes and free pigment with a diethylaminoethyl (DEAE) ion exchange chromatography column. Toyopearl 650 M beads were first washed with $TL^{0.1}E$ buffer and then loaded into the column, which was then left to pack under gravity and then further equilibrated with at least 250 mL of additional $TL^{0.1}E$ flowing through a peristaltic pump. The BRC was then loaded into the column with the pump, where it promptly bound to the upper layer of beads and was washed with $TL^{0.1}E$ until free pigment could no longer be detected in the column waste. To elute the protein, a linear salt gradient from 0.00 to 0.25 M NaCl was applied to the column. As the BRC was bound to the column beads with a different ionic strength than that of the antennae complex and other impurities, we were able to collect high purity BRC samples by collecting the column elute in small fractions using an automatic fraction collector, and then spectroscopically testing these fractions. The ratio of the summed extinction coefficients of the aromatic amino acids of the BRC at 280 nm, and that of the bacteriochlorophyll monomers at 800 nm should theoretically be 1.2. In practice we kept fractions that displayed a ratio of 1.6 or less*. Furthermore the extinction coefficients of the redox active pigments of the BRC are approximately equal, but separated in wavelength. We therefore assured that we had a 1:2:1 ratio of bacteriopheophytin to bacteriochlorophyll monomer to bacteriochlorophyll dimer, as the BRC's anatomy dictates.

*While this means there must be some non-pigment containing protein impurities, it is common practise in the field to use samples with ratios greater than 1.2, and has not been shown to significantly affect results.

Fractions meeting the above requirements were then pooled and dialyzed overnight to remove excess salt. This was done in a similar manner as before, but now in $TL^{0.1}$ as EDTA is a strong chelator of metal and therefore incompatible with studies involving manganese. The column was also washed with 1 M NaCl and stored at 4 °C for future use.

The following day the purified protein was concentrated for ease of use and storage. This was accomplished with a millipore ultrafiltration unit with a 30 kDa nominal molecular weight limit membrane, under 5 psi of nitrogen. The concentration was measured by absorption spectroscopy using the extinction coefficient of 288 $mM^{-1}cm^{-1}$ at 800 nm.[38] Samples were concentrated to approximately 100 μM and then stored in the dark at -20 °C.

For further details on BRC isolation see earlier works on BRC research.[39–41]

2.3 Sample preparation

Unless otherwise stated, concentrated, frozen BRCs were thawed and diluted to 1 μM final concentration in a dispersion of 80 mM Bis Tris Propane (BTP) and 0.03 % LDAO at pH 9.4 immediately before experiment. These conditions were chosen as they were previously found to provide optimal ET from Mn to the BRC.[22,24] Either WT or R-26 RCs were used, depending on experiment. As with protein isolation, all preparations were done in the dark with only dim, orange-filtered light, and care was taken to limit BRC illumination as much as possible.

Manganese solutions were prepared fresh before experiment from dried manganese chloride or manganese acetate, both >98 % pure, from Sigma Aldrich. This was dissolved in the buffer at 1 M concentration and vortexed until completely dissolved. The Mn^{2+} needed for electron donation would auto-oxidize to Mn^{3+} under ambient conditions, therefore care was always taken to not measure samples with exposed manganese after 3 hours. Furthermore, it was found that Mn^{2+} needs ~15 minutes to properly associate with the BRC (see Figure 3.4), therefore measurements were not taken before this period.

2.4 Biophysical characterization

2.4.1 Single-flash excitation spectroscopy

The simplest way to determine rate constants of electron transfer in the BRC is by measuring the transient spectroscopic signal associated with the change in redox state of the electron donor or acceptor. One can then directly determine the rate constant of this process from the exponential decay of the signal. We accomplished these measurement with two different instruments. For very rapid processes we used a laser flash photolysis unit (LFP-112, Luzchem Research Inc., Ottawa), capable of delivering a high-intensity pulse of ~5 ns via a Nd:YAG

laser at 532 nm, and equipped with a detector with similar temporal resolution. For slower processes we used a Cary 5000 absorption spectrophotometer (Varian, now Agilent) with temporal resolution of 33 ms, and a camera flash (SIGMA EF-530 DG Super PA-PTTL), which has a pulse width of ~1.4 μs and is capable of producing saturating photochemical light intensity to our samples. These were coupled with a water-filled light guide to prevent the heating of our samples. Although this setup has a much lower temporal resolution, the detector and dual beam measurement improved the signal-to-noise to such an extent that it became the more advantageous setup for measuring all processes with time constants >60 ms. A 750 nm band pass filter was used to reduce the excitation light intensity, and thus the initial spike in absorbance reading after a flash, for the fastest kinetic measurements.

Unless stated otherwise, all measurements were done with 1 nm spectral bandwidth, monitoring at 865 nm, where the bleaching of the dimer peak occurs. 30μM excess quinone (UQ_{10}) was added to reconstitute Q_B activity (lost during sample preparation) in BRCs, when desired. The recorded data was decomposed into 1 or more components and the 1st order rate constants were determined by fitting the data to exponential decays with a least mean squares (Levenberg-Marquardt) algorithm.

2.4.2 Optical spectroscopy of BRCs in neutral and charge separated states

Steady-state kinetics and light-induced difference spectra were measured with the same Cary 5000 spectrophotometer. Continuous, white light excitation was provided by either a 250 W tungsten lamp (Oriel 6129) powered by an AMETEK DCS33-33E power supply (Sorensen) for lower light intensity experiments, or a 1000 W mercury xenon arc lamp (Oriel 6140) powered by an Oriel 8550-5 power supply, for high intensity experiments. The light source was coupled to the spectrophotometer with the same water-filled light guide as that of the flash excitation. Unless otherwise noted the tungsten lamp was driven at 200 W, giving a flux of ~0.13 W/cm^2 at the sample surface, and the arc lamp was driven near 1000 W, giving a flux of ~1.05 W/cm^2. Kinetic measurements were again monitored at 865 nm, unless otherwise noted, with 1 nm spectral bandwidth and 33 ms temporal resolution. Light-induced difference spectra were measured from 700 – 1000 nm at 2000 nm/min, and 1.1 nm spectral resolution with 2 nm spectral bandwidth, as this allowed for fast spectrum acquisition, and therefore higher time resolution when tracking light-induced changes. Spectra were also recorded without excitation illumination to track changes of the BRC and the manganese complex not associated with illumination. These were recorded from 200 – 1000 nm at 500 nm/min, with 0.28 nm spectral resolution and 2 nm spectral bandwidth. This slower data acquisition was chosen as there were no signs of fast changes in the dark, and measurements in the UV region were very susceptible to noise, demanding higher data averaging. For all spectra measurements a baseline was collected immediately before the first measurement. hlA flat zero line was similarly recorded to assure that the probe beam of the spectrophotometer had negligible

excitation effect on the sample. Again, data was fit with a least mean squares algorithm to the appropriate mathematical function.

2.4.3 Protein monolayer deposition and interferometry (Dual polarization interferometry)

Surface binding of manganese to the BRC was probed with an Analight Bio 200 Dual Polarization Interferometer (DPI) (Farfield Group) being pumped by a Harvard Apparatus PHD2000 pump and two 30 mL disposable syringes. First an unmodified FB80 AnaChip was loaded into the DPI. Buffer (80 mM BTP, pH 8) was then flown over the chip for at least 45 minutes at 50 μL/min. Interference fringes were then selected if undistorted, otherwise ethanol and 2 % Hellmanex were injected onto the chip and the fringes were checked again. The chip was calibrated with nanopure water and 80 % ethanol m/v, as per the manufacturer's specifications. Following this, the injection rate was lowered to 25 μL/min and three 1 mL injections of 80 μM reduced cytochrome c^{2+} (cyt c^{2+}) from horseheart (Sigma Aldrich) were performed, allowing all excess protein to flow off of the chip between injections. Cyt c can easily bind to the chip surface as it is a water soluble protein with a positive surface charge, which can interact with the negative charge of the chip. Once a stable reading was achieved the chip was flushed with injections of 2 % Hellmanex and the tubing and chip were then flushed with nanopure water at a rate of 100 uL/min for at least 30 minutes. The chip was then removed cleaned, and stored for future use. This process was repeated two more times, with injections of 80 μM cyt c mixed with 1 μM BRC or 1 μM BRC + 30 mM Mn^{2+}. The BRC has a cyt c binding site on its periplasmic side, so specific binding to the cyt c layer should be observed if this site is available. Computation of the thickness and density of these layers from the measured phases at perpendicular polarizations was performed by the manufacturer's software, Analight Explorer.

2.4.4 Spectroelectrochemical redox measurements

A spectroelectrochemical redox cell was used to both control auto-oxidation of the Mn-BTP complex, and to measure the Mn^{2+}/Mn^{3+} reduction-oxidation potential of this complex. The cell was of local design, as described previously.[42] It consisted of a thin sample chamber including the measuring electrode, a 333 lines/in. gold mesh (Precision Eforming, Cortland, New York), pressed together between two UV-grade quartz windows; and an electrolyte trough connecting the two measuring electrodes, filled with 300 μM redox mediators potassium hexacyanoferrate-(II) and potassium tetracyanomono(1,10-phenanthroline)ferrate-(II). Measurements were taken relative to a miniature calomel reference electrode (Cole Palmer, Vernon Hills, Illinois, USA). A CV-27 potentiostat (Bioanalytical Systems, West Lafayette, Indiana) controlled the ambient redox potential. The instrument was calibrated according to

O'Reilly.[43]

Measurements were performed by adding a high concentration of the Mn-BTP complex to the grid (1 μM Mn^{2+} in 80 mM BTP). This high concentration was needed to provide reasonably large signals in the very short path length used. The amplitude and shift of the UV peaks of this complex were then monitored with the Cary 5000 spectrophotometer at increasing applied potentials. The difference between these peaks at no applied potential, and maximum applied potential was then assigned to the spectral changes of Mn oxidation. As measurements were taken relative to a calomel electrode, 243 mV had to be added to the measured applied potential to obtain the potential relative to a standard hydrogen electrode.

2.4.5 Electron paramagnetic resonance spectroscopy

Electronic paramagnetic resonance (EPR) measurements were performed on both an X-band Bruker 200-SRC spectrometer at a microwave frequency of ~9.61 GHz, and an X-band Bruker E580 spectrometer at a microwave frequency of ~9.64 GHz. Samples of ~300 μL were prepared at concentrations of 5 mM Mn^{2+} in 80 mM BTP at pH 9.4, where the Mn-BTP complex would form, and 1 mM Mn^{2+} in 10 mM CHES at pH 9, where the Mn hexa-aqua complex would form. Lower concentrations were needed here as at higher concentrations hlbroadening from particle-particle interactions makes the absorption bands unresolvable.

2.4.6 Surface tension measurements

The surface tension of suspensions was determined with the ring method using a CSC DuNouy interfacial tensiometer (Central Scientific Co. Inc., Fairfax Virginia, USA). A platinum-iridium ring from the same company was used with a circumference of 5.992 cm, and ratio of the radii of ring and the wire of 53.6. The surface tension of suspensions of 80 mM BTP at pH 9.4, with varying concentrations of LDAO detergent were determined by pulling the ring through the surface of the suspension while measuring the tension on the surface at the breaking point.

2.5 Data analysis

2.5.1 Kinetics of electron transfer

Monitoring the kinetics of the recovery of the bleached 865nm peak associated with light-induced P^+ formation, or the recovery of other spectral features associated to other redox states, was the main method of determining rate constants for electron donation and charge recombination. These kinetics were decomposed into 1 or 2 different exponential decays and

assigned to different processes, depending on the conditions being probed. For LFP and camera flash measurements the data were fit with two components for Q_B active samples, one assigned to $P^+Q_B^-$ charge recombination and 1 assigned to $P^+Q_A^-$ charge recombination; and they were fit with 1 component for samples with terbutryne, an inhibitor of electron transfer to Q_B. The kinetics produced by continuous illumination were fit to only one component, corresponding to manganese electron donation to P^+, where fast recoveries and high concentrations of Mn^{2+} were present, and two components for low Mn^{2+} concentrations and slow processes, where the second component corresponded to Mn^{2+}-BRC systems in a different conformational state. This decomposition was performed by fitting the decaying signal to the exponential decay equation:

$$A(t) = Be^{k_1 t} + Ce^{k_2 t} \tag{2.5.1}$$

Where $A(t) \equiv$ amplitude of P at any time t

B, $C \equiv$ amplitudes of the different kinetic components

k_1, $k_2 \equiv$ rate constants of the decaying kinetic components

The time constant, or lifetime, associated with the rate constant, $(\tau) = 1/k$, is often reported in place of the rate constant itself.

2.5.2 Decomposition of absolute and difference absorption spectra

Resolution of difference spectra into the individual changes of each of the bands of the BRC's spectrum were resolved by a two part process. First Gaussians were fit to the bands of the spectrum before any changes were induced. This was done with a simple Gaussian distribution:

$$A(\lambda) = \sum_n B\, exp\left[-\frac{1}{2}\left(\frac{\lambda - \lambda_i}{b_i}\right)^2\right] \tag{2.5.2}$$

Where $A(\lambda) \equiv$ absorbance at wavelength λ

$B \equiv$ amplitude of the band's peak

$\lambda_i \equiv$ spectral position of the peak of the unaltered spectrum

$b_i \equiv$ standard deviation of the band of the unaltered spectrum; related to the Full Width at Half Maximum (FWHM) by: $\mathrm{FWHM} = 2\sqrt{2ln2}b_i$

In the case of multiple overlapping absorption bands, such as the NIR spectrum of the BRC, fits were performed on the sum of the bands, to account for contributions from the tails of neighboring bands. In this case Eq. 2.5.2 took the form:

$$A(\lambda) = \sum_{n=1}^{N} B_n \, exp\left[-\frac{1}{2}\left(\frac{\lambda_n - \lambda_{n,i}}{b_{n,i}}\right)^2\right] \tag{2.5.3}$$

Where N is the number of absorption bands present.

Once Gaussian parameters for the unperturbed absorption bands had been determined, changes were induced, such as by the addition of manganese. A new spectrum was then recorded, and a difference spectrum was created. The shifts and broadenings or narrowings of this difference spectrum were then fit, using the parameters of the unaltered Gaussian and the equation:

$$\Delta A(\lambda) = B\left\{exp\left[-\frac{1}{2}\left(\frac{\lambda - \lambda_f}{b_f}\right)^2\right] - exp\left[-\frac{1}{2}\left(\frac{\lambda - \lambda_i}{b_i}\right)^2\right]\right\} \tag{2.5.4}$$

Where $\Delta A(\lambda) \equiv$ the change in absorbance at wavelength

$\lambda_f \equiv$ spectral position of the peak after the change (this would be different than λ_i for shifts, or identical for broadenings/narrowings)

$b_f \equiv$ standard deviation of the band after the change (this would be different than b_i for broadenings/narrowings, or identical for shifts)

2.5.3 Ligand binding

Dissociation constants were determined by assuming equilibrium binding,

$$nL + S \rightleftharpoons nL : S$$

where L is the ligand (generally Mn in our case), n is the number of ligands active in the binding, S is the substrate (generally BRC in our case), and $nL : S$ is the substrate with bound ligand(s). Such an equilibrium leads to the common binding equation:

$$A = \frac{B}{1 + (K_D/[L])^n} \tag{2.5.5}$$

Where $A \equiv$ the fraction of occupied binding sites; in our case this is generally the fraction of BRCs exhibiting reduction by manganese

$B \equiv$ total amplitude, or maximum fraction of binding attainable

$K_D \equiv$ dissociation constant of the binding

$[L] \equiv$ ligand concentration; in our case this is generally Mn^{2+} concentration

This equation was then fit to our data, yielding K_Ds of the binding. We also occasionally monitored binding by the disappearance of the fraction of unoccupied binding sites, for example the

fraction of BRCs exhibiting no or slow recovery not typical of BRCs with bound manganese. This is simply $B - A$, therefore Equation 2.5.5 becomes:

$$B - A = \frac{B}{1 + (K_D/[L])^{-n}} \tag{2.5.6}$$

2.5.4 Redox potentials

Oxidation/reduction midpoint potentials were determined by plotting the mole fraction of the oxidized or reduced form of the molecule of interest as a function of applied potential. The fractions were determined by the positions and/or the intensities of the absorbance bands that were sensitive to the applied potential. The data were fit with a Nernst equation:

$$E_{app} = E_m + \frac{RT}{nF} ln \frac{O}{R} \tag{2.5.7}$$

Where E_{app} $\equiv$ applied potential

E_m $\equiv$ midpoint potential

R $\equiv$ universal gas constant, 8.314 $JK^{-1}mol^{-1}$

T $\equiv$ absolute temperature

n $\equiv$ number of electrons involved in the process (1 in our case)

F $\equiv$ Faraday constant, $9.648 \text{x} 10^4$ $Cmol^{-1}$

O $\equiv$ mole fraction of the molecule oxidized at the applied potential

R $\equiv$ mole fraction of the molecule reduced at the applied potential

3

Results

As explained in Section 1.4.1.2 of the Introduction, BTP coordinated manganese (II) ions have previously been shown to act as secondary electron donors to native BRCs. However, much remains unclear about the interaction between these donors and the BRC, including specifics of the binding of manganese to the BRC, and the rate at which electron donation to the oxidized bacteriochlorophyll dimer takes place. In this work we present a mechanism which provides a resolved picture of both these issues, along with evidence of the manganese composition of the Mn-BTP complex.

3.1 Probing manganese binding sites in the bacterial reaction center

Ligand binding site modeling software (Q-SiteFinder, University of Leeds[44]) previously predicted two metal binding sites of the BRC that were plausible candidates for a secondary electron donor.[22] One of these sites (Site 1) is located at the inner opening of the carotenoid binding site, in a large cavity in the membrane-shielded region of the protein. The other (Site 2) is located on the periplasmic surface of the BRC at the the approximate location of the docking site of the native electron donor, cytochrome c_2 (cyt c_2). The location of the two binding sites on the BRC can be seen in Figure 3.1. In order to confirm binding of a manganese ion to one or both of these sites, and distinguish between them, we first established evidence of manganese binding to each of these sites, and then systematically tested them for redox activity.

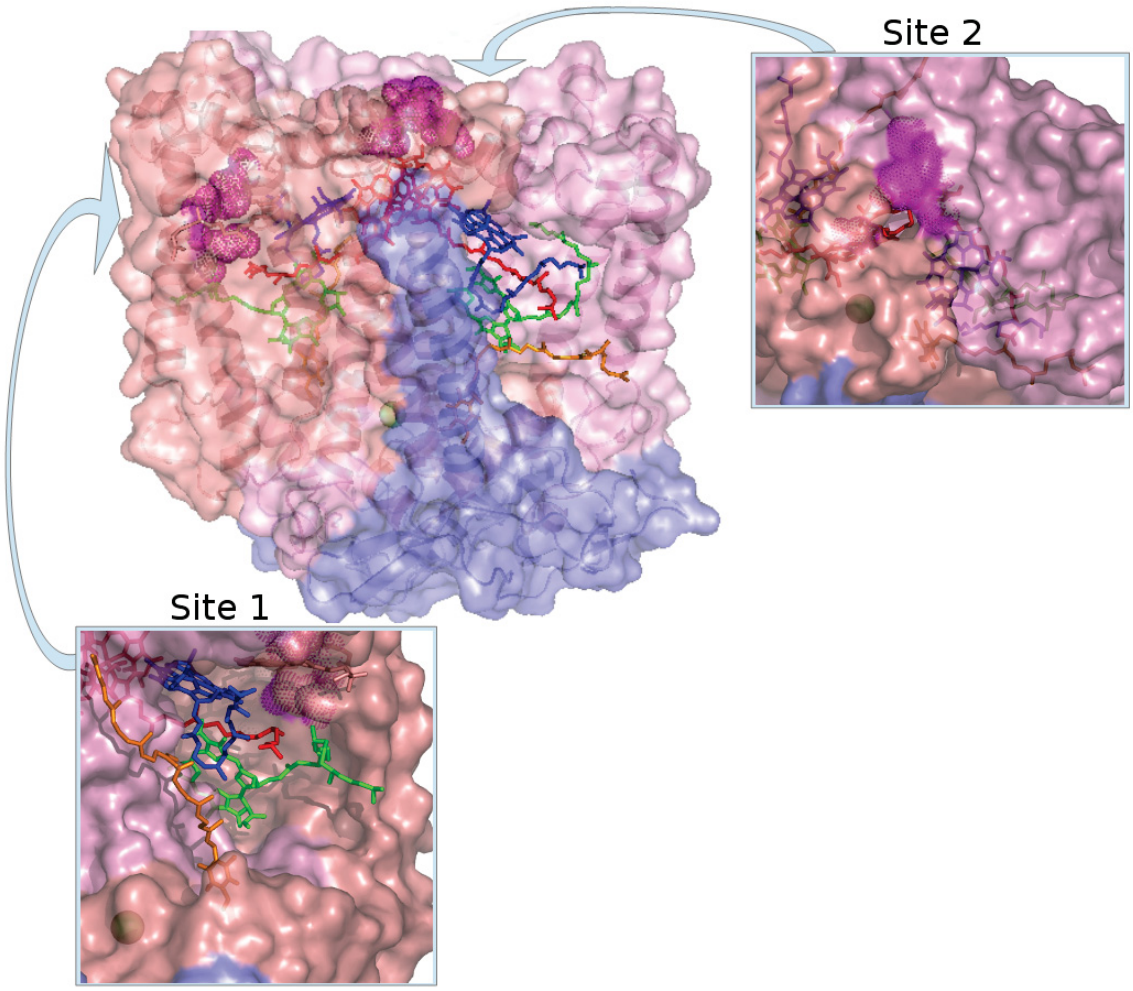

Figure 3.1: Predicted metal binding sites on the BRC. BRC represented as both a surface and semi-transparent ribbons. Binding sites are shown as bright pink spheres. Coloring of the subunits and cofactors is the same as in Figure 1.1. Atomic coordinates taken from PDB code: 1PCR.

3.1.1 Manganese binding near the carotenoid binding site (Site 1)

Site 1 is buried in the hydrophobic membrane region of the protein. A closeup of this binding site (pink) is shown in Figure 3.2, from inside the cavity in panel A, and from outside the cavity in panel B. Also shown in these images is the direction of the Q_y dipole moments of the bacteriochlorophyll dimer (P) and monomer (B), colored red and blue, respectively. The alignment of these dipoles is such that they approximately point to or from the proposed binding site. Therefore, the presence of charges at this location should affect them significantly. Furthermore, the carotenoid cofactor (colored salmon) binds in the immediate vicinity of this site. We would, thus, expect differences in binding affinities of WT and R-26 (the carotenoid-less mutant) BRCs at this site. As shown in Section 1.3 of the Introduction, strong absorption bands (Q_y bands) are seen due to excitation along these dipoles in the NIR. Consequently, we

should be able to observe evidence of Mn^{2+} binding by recording the NIR absorption spectra of BRC in the presence and absence of manganese. To eliminate auto-oxidation, the samples were placed in a spectroelectrochemical cell where the operating redox potential and the corresponding absorption changes were controlled (see Section 2.4.4 of Materials and methods for details). The BRC-Mn^{2+}/BRC difference spectra are shown with thick grey lines in panels D and H for R-26 (recorded previously[24]) and WT, respectively. The features of these difference spectra were then decomposed into shifts and broadenings of the Q_y bands of the cofactors with Gaussian fits, as outlined in Section 2.5.2 of Materials and methods, and are also shown. The previous results of these fittings for R-26 found that the presence of Mn^{2+} caused a blue shift on the P band from 866.7 nm to 865.0 nm, a broadening of the B band by 1.0 nm at FWHM, and a very small red shift of the H band from 757.8 nm to 758.2 nm. For WT, the presence of manganese was found to induce a similar blue shift of the P peak from 866.2 nm to 865.4 nm, but the B and H peaks were also blue shifted this time, from 804.9 nm to 803.4 nm for B, and from 758.4 nm to 756.9 nm for H. These effects of Mn^{2+} on the Q_y dipoles suggests the binding of a Mn^{2+} ion along the axes of these dipoles, which traverse the hydrophobic, membrane-embedded region of the pigment-protein complex. The fact that the presence or absence of a carotenoid affects these spectral changes suggests that manganese must bind at or near Site 1.

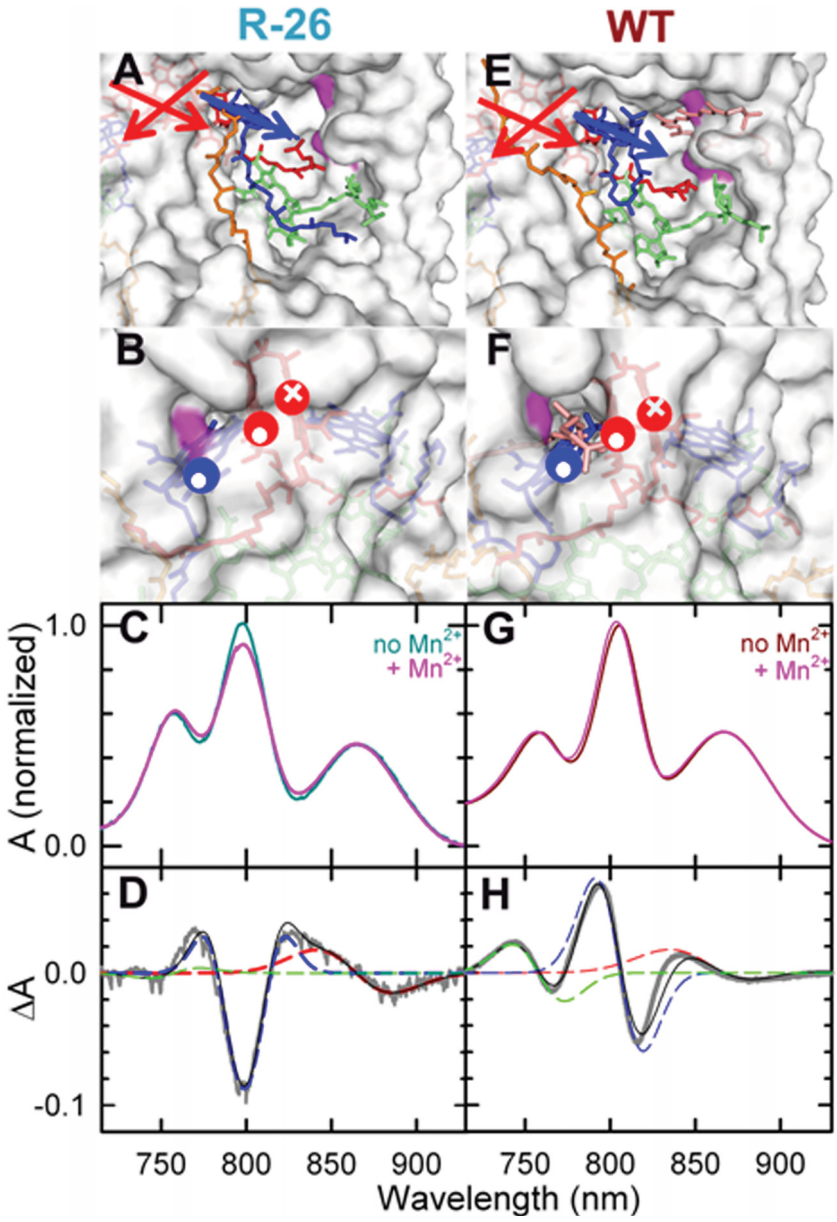

Figure 3.2: Confirmation of manganese binding to Site 1 from the effect of the presence of Mn^{2+}on the Q_y dipoles of the bacteriochlorophylls. Left panels: R-26, right panels: WT. Close-up of the proposed manganese binding site located in the membrane region of the protein, as seen from inside the cavity (A, E), and from the exterior of the protein (B, F). The protein is shown with a white surface representation, with the binding site colored pink. Cofactors are shown as sticks colored red, blue, green, orange, and salmon for P, B, H, Q, and carotenoid, respectively. The Q_y dipole moments of P and B are also shown, and colored to match their cofactors. Note the carotenoid cofactor (salmon) is only present in WT BRCs. NIR absorption spectra of the BRCs are shown with and without Mn (C, G), along with the difference spectra (D, H). Difference spectra are shown with grey lines, their decompositions into shifts and broadenings of the peaks of the cofactors' dipole moments are shown with dashed lines (colors match the cofactors), and the sum of these decompositions are shown as thin, black lines. Conditions: ~200 μM RC in 0.05 % TX-100, 80 mM BTP at pH 9.4, 70 mM KCl, 300 μM hexa cyano ferate (ferricyanide) and 30 mM Mn^{2+}. Panels C, D data and analysis from Ivanescu.[24] Atomic coordinates taken from PDB codes: 1PCR.

3.1.2 Manganese binding to the cytochrome c_2 binding site (Site 2)

The other proposed binding site, Site 2, resides on the periplasmic surface of the BRC, at the cyt c_2 binding site (Figure 3.3 A). This site is a more likely candidate for metal binding, as it is solvent accessible, yet still provides a reasonably short electron-tunneling pathway to the dimer (13 Å). As the binding site overlaps with that of cyt c_2 and other cytochromes, we determined whether manganese competes with cytochrome* to occupy this site. If this is the case we should notice a weakened binding of cyt c to the BRC in the presence of manganese. We tested for this by binding the positively charged cyt c^{2+} to the surface of a negatively charged silicon chip, creating a monolayer of protein. We then measured the thickness and mass of this layer with a Dual Polarization Interferometer (DPI) (see Section 2.4.3 for details). Next we compared the properties of this layer with layers made in a similar manner, but with injections of cyt c^{2+} and BRC, or cyt c^{2+} and BRC that had been pre-mixed with Mn^{2+}. The thicknesses of the resulting layers are shown in Figure 3.3 B, along with possible binding configurations which match the measured thickness (mass data gave nearly identical relative results, and has been left out for clarity). Layer thicknesses were measured to be 2.2 nm, 5.7 nm, and 2.5 nm for cyt c^{2+} alone, cyt c^{2+}+BRC, and cyt c^{2+}+BRC+Mn^{2+}, respectively. As layers containing BRCs pre-exposed to manganese resulted in a layer thickness similar to that of cyt c^{2+} alone, we concluded that cyt c^{2+} was unable to bind to these BRCs. This is most likely due to Mn^{2+} binding to Site 2 of the BRC during pre-mixing, and then preventing further binding at this location by cyt c^{2+}.

*Note that we do not use the native secondary electron donor of the BRC, cyt c_2, but instead a similar commercially available cytochrome c (cyt c) from horse heart. This form of cytochrome c is chemically similar, and has been shown to be fully functional as a secondary electron donor to the BRC.[45,46]

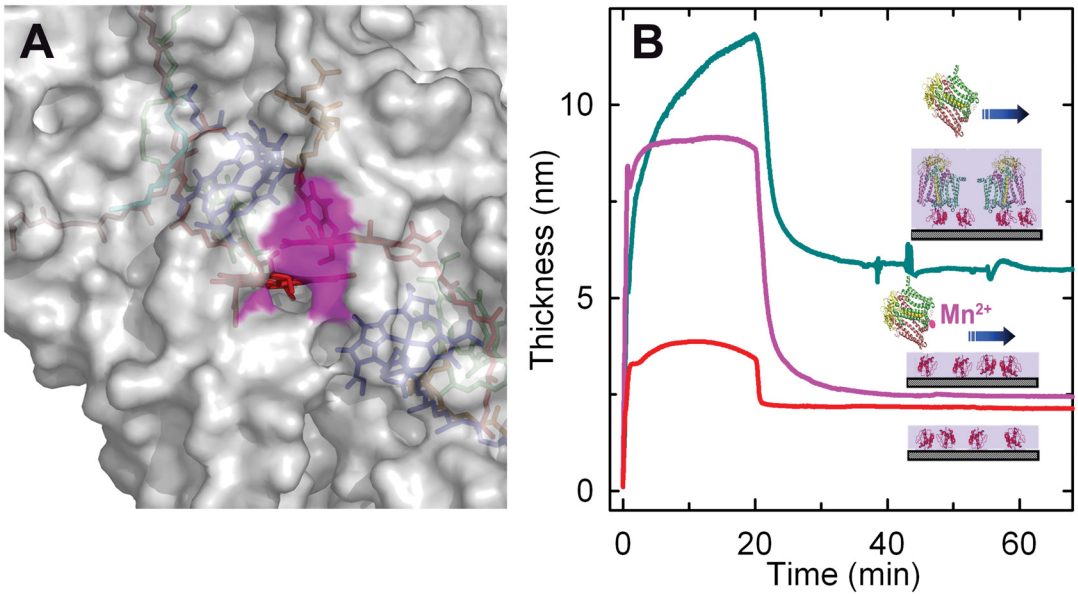

Figure 3.3: Evidence of a bound manganese at Site 2. A: top view of the predicted binding site (pink) of the BRC. B: measured thickness of bound layer after injection of: cyt c^{2+} (red trace), cyt c^{2+}+BRC only (blue-green trace), cyt c^{2+}+BRC pre-mixed with Mn^{2+} (pink trace). Diagrams depict possible scenarios with matching thicknesses. Conditions: A: coordinates were taken from PDB entry 1RG5. B: an injection of 1 mg/ml cyt c^{2+} alone, or mixed with 1 μM R-26 BRC or 1 μM R-26 BRC pre-mixed with 30 mM Mn^{2+}. A running buffer of 80 mM BTP pH 8 was used. Atomic coordinates taken from PDB code: 1PCR.

3.2 Evidence of a secondary electron donor at Site 1 upon manganese binding

Once manganese binding to the BRC had been confirmed for two different binding sites, we searched for evidence of electron donation to the dimer from each of these sites. To do this we performed several different experiments that would demonstrate manganese electron donation from one site or the other. We first examine the evidence of electron transfer from manganese bound to Site 1.

3.2.1 Accessibility of the binding sites to the manganese electron donor

The two proposed binding sites are very different in nature, with Site 2 on the the periplasmic surface being solvent accessible, and therefore having a high affinity to ions and polar molecules, and Site 1 being contained in the membrane-shielded region of the protein, an energetically unfavorable environment for ions and polar molecules due to its low dielectric constant. From these differences one must assume a much different accessibility of these sites for manganese. Addition of a water soluble secondary electron donor should, therefore, show

virtually instantaneous activity if ET occurs at the periplasmic surface of Site 2, while this would not be expected if ET occurs at the more buried Site 1. To observe this difference we added Mn^{2+} to the BRC and allowed it to incubate for a varying amount of time before illuminating it and recording the proceeding kinetics. By monitoring the difference in the observed rate constant of P^+ reduction with respect to the incubation time of Mn^{2+}, we could observe the rate of diffusion and binding of the Mn complex to the BRC (fitted lines in panel B), quantifying the binding site's accessibility to manganese. From Fick's law of diffusion, $J \propto -\nabla c$, we know that the rate of diffusion, J, will be proportional to the concentration gradient, ∇c, of the diffusing species, in this case manganese. As these diffusional rates can be rapid relative to the time needed to prepare and perform a measurement (minutes), a lower manganese concentration of 5 mM was chosen for this experiment.

The accessibility of Site 1 to manganese must also be affected by light-induced conformational changes of the BRC, which have been shown to occur in this same cavity, near B_B,[47] precisely where the proposed manganese binding site lies. These conformational changes can therefore also be used as a probe of Site 1, by comparing the accessibility of the binding sites to manganese in BRCs which have had these changes induced in them (red traces and symbols), to the accessibility in BRCs that are kept in the dark-adapted state (black traces and symbols). The presence of Mn^{2+} ions has been shown to block these conformational changes in the BRC,[24] therefore dark-adapted samples could be prepared by adding Mn^{2+} before exposing samples to illumination. However, samples in which light-induced conformational changes were desired were pre-illuminated for 1 minute with 0.13 W/cm^2 of continuous white light to bring samples to a new conformational state. Mn^{2+} was then added once the charge-separation had recovered. As these illumination conditions have been shown to induce conformational changes recovering on the hours timescale, we had ample time to perform experiments on these conformationally altered BRCs.

Kinetics of dark-adapted and pre-illuminated samples, both soon after Mn^{2+} addition, and after sufficient time to attain the maximum rate, are shown in in Figure 3.4 A. The rate constants of these kinetics as a function of the manganese incubation time are shown in panel B. The rate constants of electron transfer from Mn^{2+} to the BRC were found to increase by 80 % to a maximum of 0.20 s^{-1} for dark-adapted BRCs, and increased by 35 % to a maximum of 0.28 s^{-1} for pre-illuminated BRCs. The large increase in rate constant with Mn^{2+} incubation time suggests a diffusionally limited process due to a low accessibility of the binding site to Mn^{2+}. The greater rate constants and lesser dependence on incubation time of pre-illuminated samples suggests that light-induced conformational changes of the BRC increase the accessibility to Mn^{2+}. The rise in rate constant with incubation time took ~20 minutes to reach saturation for pre-illuminated samples, while saturation took over 60 minutes for dark-adapted samples. The shorter saturation time required for pre-illuminated samples again demonstrated the increased accessibility to Mn^{2+} due to light-induced conformational changes.

Both the low accessibility of the binding site to Mn^{2+}, and the increase in this accessibility by

light-induced conformational changes provide evidence that the identity of the BRC's dominant or only secondary electron donor is a Mn^{2+} at Site 1.

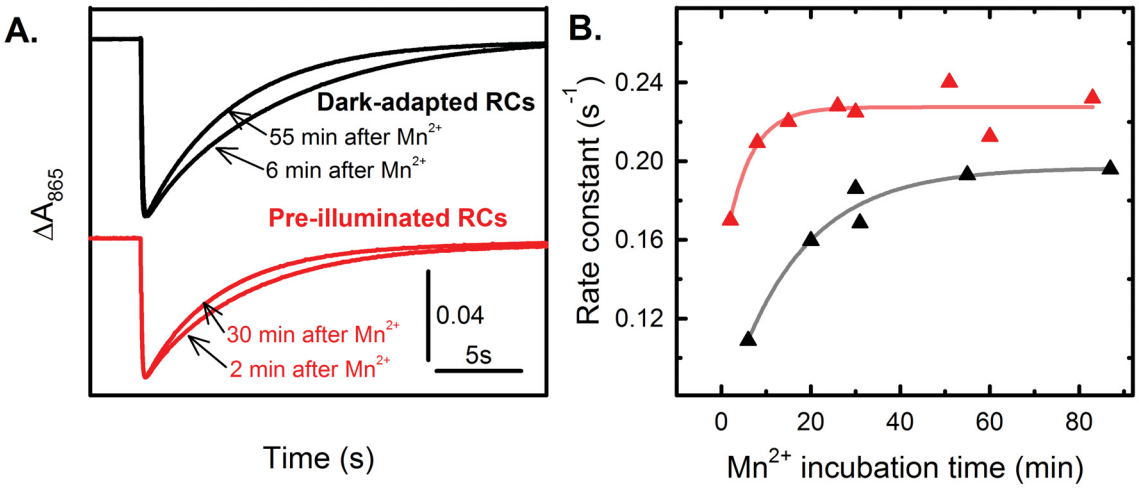

Figure 3.4: Influence of light-induced conformational changes on the kinetics of P^+ reduction in the presence of Mn^{2+}. A: representative traces of P^+ recovery kinetics soon after manganese addition, and at the time of maximum rate. B: rate constants as a function of Mn^{2+} incubation time. Solid lines represent exponential fits to the increasing rate constant with time, yielding rate constants of 3.7 s^{-2} and 10.9 s^{-2} for dark-adapted and pre-illuminated BRCs, respectively. Conditions: 1 μM R-26 in 0.03 % LDAO, 80 mM BTP at pH 9.4, 5 mM Mn^{2+}. Pre-illumination was accomplished by exciting samples with 0.13 W/cm^2 continuous illumination for one minute, fifteen minutes prior to manganese addition.

3.2.2 Effect of molecules with different dielectric properties and functional roles on electron transfer from Mn^{2+} at Site 1

Previous studies have shown many molecules present inside the two large hydrophobic cavities of the BRC's membrane region, some even obtaining direct images with x-ray crystallography. These observed molecules include those with important functional roles, such as quinones, carotenoid, and when used, herbicides,[52,53] along with other molecules such as water, glycerol, lipids, and detergent.[48–51] Furthermore, the cavity containing the carotenoid binding site (and Site 1) has been shown to be solvent-accessible, though on the timescale of hours,[54] whereas no such evidence of accessibility has been reported for the cavity containing the active cofactors. We, therefore, had a means to induce environmental changes in the vicinity of Site 1 through the presence or absence of some of these molecules. We used these changes as probes for manganese electron transfer from this site.

To identify potential molecules appropriate for probing these cavities, we monitored the effects of the candidate molecule on the Q_y bands of the BRC. As discussed earlier, and shown in

Figure 3.2, the axis of the Q_y dipole passes through these cavities, very close to Site 1 itself, for the H and P pigment cofactors. Therefore any spectral changes caused by the addition of these molecules would suggest that they can access deep into these cavities and disrupt the electrostatics of the cofactors' dipoles. Figure 3.5 shows the spectral effects induced by the addition of molecules found to have the greatest effect. These difference spectra were taken for both R-26 (blue-green traces), and WT (brown traces) BRCs, so that the presence or absence of the carotenoid molecule, residing near Site 1, would act as an additional probe. LDAO, NaCl, UQ_{10}, and the bound carotenoid of WT all showed large effects on the Q_y bands, identifying themselves as having access to the close vicinity of the pigment cofactors. The probes had the largest effect in R-26 samples, where the carotenoid was not present. The spectral effects of these probe molecules were then decomposed into shifts and broadenings/narrowings of each of the pigments. The major contributions of these effects were: a blue shift of the P band of 5 nm upon addition of 0.2 % LDAO, a red shift of the P band of 2.5 nm upon addition of 100 mM NaCl, and a red shift of the P band of 4.5 nm as well as a narrowing of the B band by 2 nm. Pictured beside these difference spectra are images, taken from X-ray crystallography data,[48,49,52] of these probe molecules bound near Site 1.

The influence of these probe molecules on the Q_y bands, along with their previously observed binding near Site 1 (except for NaCl, which will also be present near Site 2 due to its polar nature), suggests that they must be binding near the large hydrophobic cavities. The sensitivity of all of these shifts to the presence of the carotenoid (WT BRCs) gives further evidence to binding near Site 1.

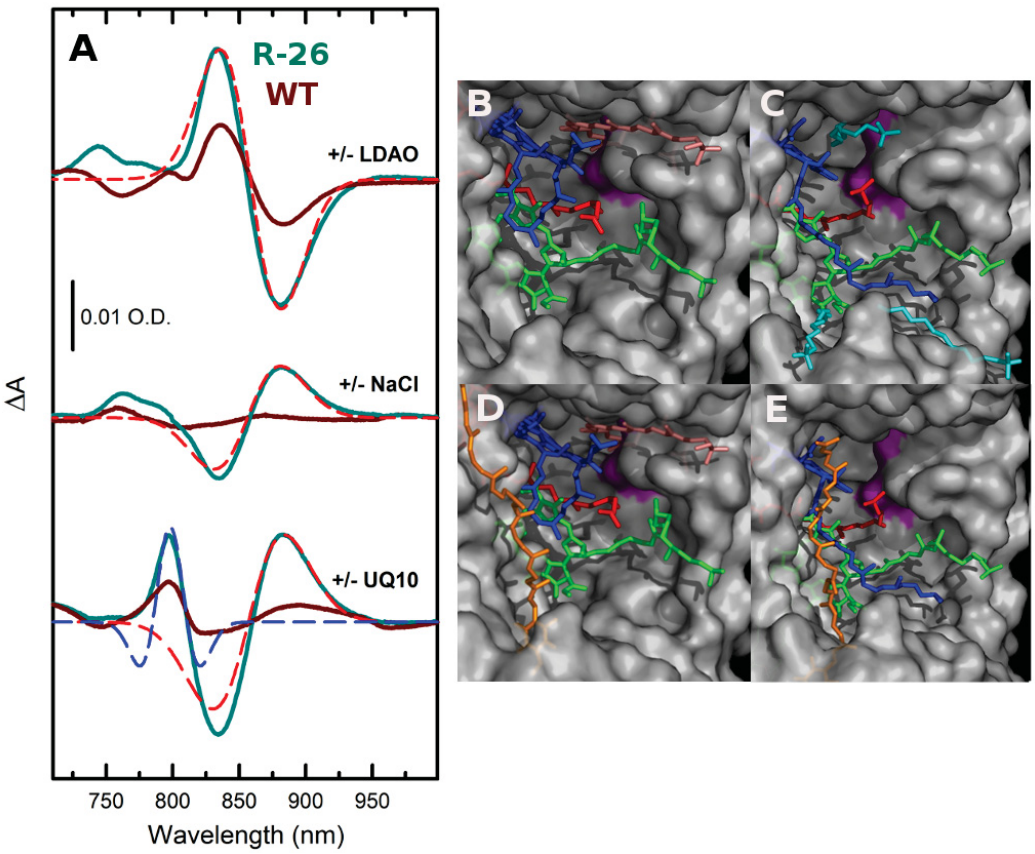

Figure 3.5: The effects of several molecules with access to Site 1 on the optical absorption spectrum of the BRC cofactors' Q_y dipoles. A: The difference spectra for R-26 (blue-green) and WT (brown) BRCs in the presence/absence of: an additional 0.2% LDAO (top trace), 100 mM NaCl (middle trace), or 30 μM UQ_{10} (bottom trace). The higher amplitudes of the R-26 spectra have been decomposed into shifts and a narrowing of the different pigment bands. This is shown as dashed lines, colored red and blue for P and B, respectively. B - E: X-ray crystallography images showing probe molecules near Site 1, with representation and coloring similar to Figure 3.2. B, C: LDAO binding at Site 1 for R-26 and WT. In WT the presence of the carotenoid (salmon) prevents LDAO binding to Site 1 (panel B), yielding a smaller shift. In R-26 multiple LDAO molecules (cyan) have been observed to bind to the BRC in this region, with one bound precisely to Site 1 (panel C). D, E: UQ_{10} binding. Binding of UQ_{10} (orange) is similar in WT (panel D) and R-26 (panel E). Note: Na^+ and Cl^- ions are not pictured as crystal structures with small ions present have not been observed. Conditions: 1 μM BRC in 0.03 % LDAO, and 80 mM BTP at pH 9.4. Atomic coordinates taken from PDB codes: 1PCR, 4RCR, and 1RG5.

Once the probe molecules had been identified and tested for access to Site 1, their effects on Mn^{2+} electron transfer (ET) to P^+ were tested. This was accomplished by illuminating BRCs in the presence of Mn^{2+}, and each molecule individually, and recording light - dark optical difference spectra, as seen in Figure 3.6 (for an explanation of light - dark spectra see Section 1.3 of the Introduction). As Mn^{2+} was present to act as a secondary electron donor, the light-induced charge-separated state, P^+Q^-, was rapidly reduced to the PQ^- state, producing a light - dark difference spectrum similar to that observed using other molecules (such as cyt c^{2+}) as secondary electron donors, as shown in the top traces of Figure 3.6. Initially the

difference spectra in the presence of these molecules were all similar to this spectrum of the PQ^- state. However, as pre-illumination had previously been found to increase the binding affinity of Mn to the BRC (see Figure 3.4), pre-illuminated samples were tested here as well (3^{rd} trace down, and all following traces). With pre-illuminated samples a large blue shift of the dimer band was observed, in addition to the normal PQ^- spectrum. The magnitude of this shift was found to be sensitive to the presence of the probe molecules, including the carotenoid, present in WT BRCs. As this shifted P band was only observed for pre-illuminated BRCs with Mn^{2+} present, it is likely due to an oxidized manganese, being influenced by the light-induced conformational changes. In the previous section pre-illumination was shown to increase the accessibility of Site 1 to Mn^{2+}, it is therefore possible that the manganese at Site 1 could be more tightly bound in these BRCs, and could remain bound after oxidation. The presence of the extra charge of Mn^{3+} at Site 1 could then affect the Q_y dipole of the cofactors, and give rise to the observed dimer shift. While this hypothesis provides an explanation for the observed spectral differences, and could also provide further evidence for the Site 1 bound manganese being responsible for electron transfer to the BRC, further tests needed to be performed to validate it. We performed these tests in the following section.

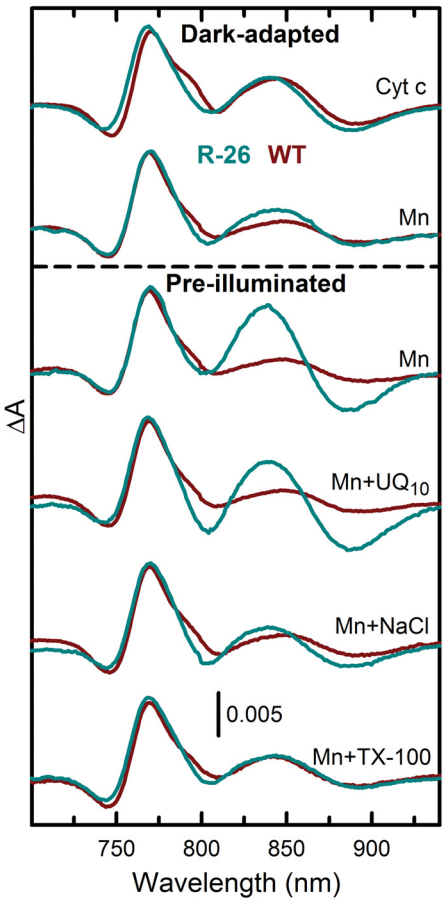

Figure 3.6: Light - dark optical difference spectra of BRCs in the presence of a secondary electron donor, or a secondary electron donor and a molecule with access to Site 1. R-26: blue-green, WT: brown. Samples for the first two traces were kept in the dark-adapted state, while samples for the following traces were pre-illuminated. Conditions as for Figure 3.5 with the addition of either 30 mM Mn^{2+} or 30 μM cyt c^{2+}. LDAO was replaced with TX-100 in the bottom trace.

3.2.3 The origin of the electrochromic dimer shift induced by manganese oxidation

To better understand the source of the large dimer shift observed in Figure 3.6, we monitored the recovery of this shift relative to the recovery of the unaltered PQ^- state in both pre-illuminated and dark-adapted samples. The spectral changes of the PQ^- state in the absence of manganese are due to the impact on the Q_y dipoles of the cofactors from the negative charge residing on the quinone. If, however, the large dimer shift in the presence of manganese is due to the presence of a different charge, such as the hypothesized extra positive charge of a bound oxidized manganese, the dimer shift should recover with a different rate than that of the other spectral features. The peak-to-trough amplitudes of the two main spectral features

of the PQ^-/PQ spectrum of pre-illuminated R-26 samples, the blue shift of the dimer peak at 865 nm and the red shift of the bacteriopheophytin peak at 757 nm, are plotted as a function of time in Figure 3.7. For comparison the recovery of the dark-adapted PQ^-/PQ spectrum is also plotted, which lacks the large dimer shift of pre-illuminated samples. Additionally, a few measurements with WT were taken, though an in-depth study of WT was not performed as a large P shift was not observed in this strain. The recoveries of these electrochromic changes were found to be the same within experimental error (see Figure 3.7 for times). We can, therefore, conclude that the large shift in the P band recovers with the PQ^- state. An explanation of why a manganese signal would have an identical recovery is given in Section 4.2.2.2 of the Discussion.

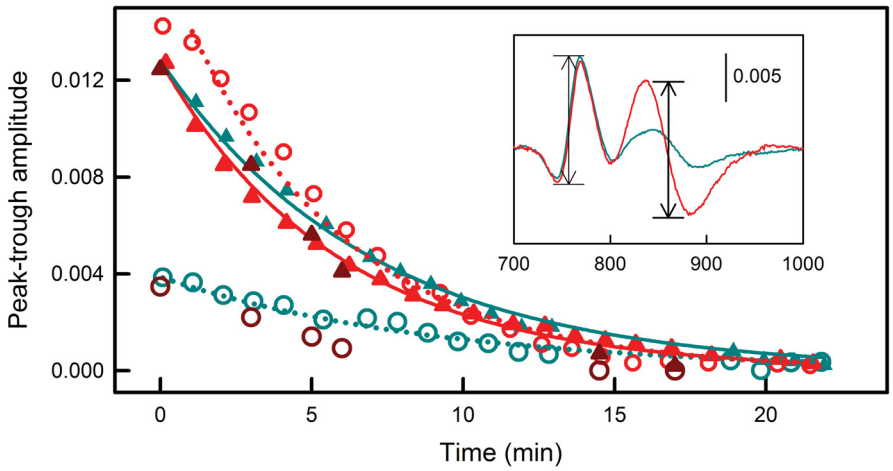

Figure 3.7: Recovery of the light-induced spectral changes of pre-illuminated and dark-adapted R-26 BRCs in the presence of manganese. The inset shows the light - dark difference spectra promptly after illumination was stopped, and where the amplitudes are measured. Red and blue-green symbols represent pre-illuminated and dark-adapted R-26 samples, respectively, while open circles and closed triangles represent peak-to-trough amplitudes of the 865 nm shift of the P band and the 757 nm shift of the H band, respectively. The kinetics followed simple exponential decay for all recoveries (solid lines) except for the pre-illuminated dimer shift, whose recovery was delayed by a preceding process. Lifetimes at 865 nm and 757 nm, respectively: 5.3 minutes and 5.9 minutes for pre-illuminated samples, 9.2 minutes and 6.9 minutes for dark-adapted samples. The two datasets were normalized to the dark-adapted 770 nm peak. Additionally, some WT measurements are shown in brown. As there was no difference between pre-illuminated or dark-adapted WT, only pre-illuminated data is shown. Conditions as for the traces labeled "Mn" in Figure 3.6.

Along with measuring the rate constant of its recovery, we also studied the cause of this large dimer shift by determining its dependence on detergent. We saw from Figure 3.6 that while the large dimer shift could be induced with pre-illumination, it could also be prevented by the presence of NaCl, or the absence of LDAO detergent, as no shifts were observed for these cases (LDAO was exchanged for TX-100 in the bottom trace). The effect of NaCl can be explained

by the presence of a high concentration of ions screening the electrostatic interactions needed for ligand binding, however the effect of LDAO is less obvious. It could either be due to the difference in membrane substituent, in neutral TX-100 and zwitterionic LDAO detergent, or it could be due to one or more LDAO molecules binding near Site 1 and facilitating manganese binding to the BRC, as seen in Figure 3.5 C. In order to differentiate between these two possibilities we performed two LDAO titrations. The first was performed while monitoring the amplitude of the large dimer shift relative to the bacteriopheophytin shift, as seen in Figure 3.8 A. The behavior of this titration fit to Eq. 2.5.5 for a single LDAO ligand, yielding a K_D of 3.7 mM in R-26 (dashed blue-green line) and 12.6 mM in WT (dashed brown line). The second titration was performed while monitoring the surface tension of the suspension (panel B). In the semi-log plot of surface tension versus LDAO concentration, the different LDAO dependent regions, corresponding to the monomer phase and the micellar phase, appear linear. The intersection of the fits to these regions (solid black lines) shows the point of phase transition of the detergent, known as the critical micelle concentration (CMC), and was found to be 0.4 mM. This is lower than CMC values typically reported in the literature of ~1.6 mM,[55–57] which is not a surprise as the CMC is known to be affected by both buffer concentration and pH,[55] both of which are elevated in our case. Presence of the BRC could also affect the CMC but the instability of the BRC at low detergent concentrations makes this difficult to determine.

By comparing the CMC of LDAO to the K_D of LDAO-BRC binding we can see that these events are not closely related, as they are separated by an order of magnitude in LDAO concentration. This suggests that it is not the membrane environment of the LDAO detergent belt which is critical for this shift, but instead a bound integral LDAO molecule.

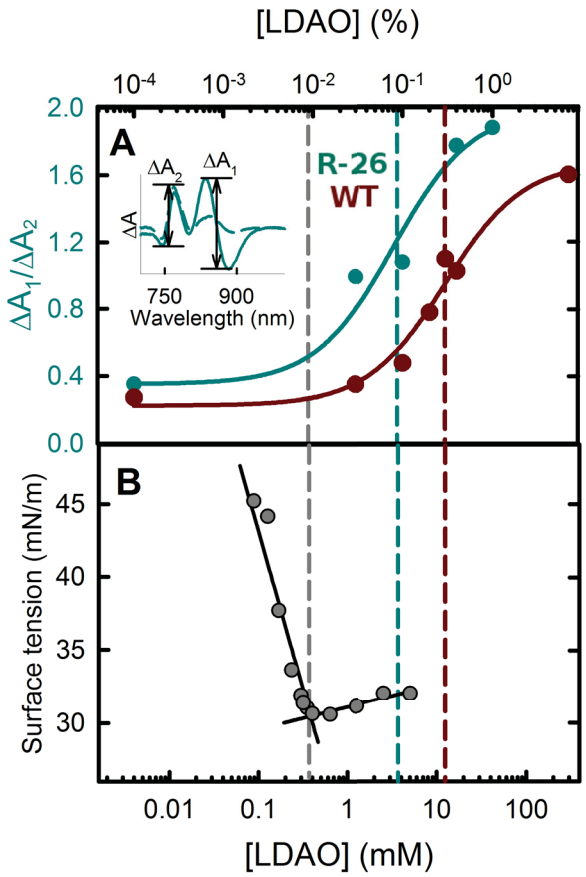

Figure 3.8: Influence of LDAO on the large electrochromic dimer shift, and the surface tension of the suspension. A: the normalized peak-trough amplitude of the dimer shift of light - dark difference spectra as a function of LDAO concentration. Inset shows where the peak-trough amplitude is measured, and how it is normalized. Solid lines represent fits to binding equation 2.5.5, and dashed lines mark the K_D of these fits, 3.7 mM for R-26 and 12.6 mM for WT. B: the surface tension as a function of LDAO concentration. Solid lines represent exponential fits to the strong and weak concentration dependence regimes of during and after micelle formation, respectively. The dashed grey line marks the CMC, 0.4 mM, determined by the intersection of these lines. Conditions as in the pre-illuminated trace with manganese of Figure 3.6.

3.3 Kinetics of electron transfer from a manganese (II) ion to the oxidized dimer

With evidence of a bound, redox active manganese at Site 1 established, we next characterized the kinetics of both charge recombination and manganese oxidation electron transfers of the Mn-BRC system. This was accomplished by probing the kinetics of multiple time regimes, with multiple forms of BRC photo-excitation, and finding the optimal conditions for P^+ reduction by Mn^{2+}.

3.3.1 Influence of a bound manganese on charge recombination

3.3.1.1 Kinetics following flash excitation

We first found the rate constants of P^+ reduction in the presence of Mn^{2+} using flash excitation. A titration of Mn^{2+} was performed while monitoring the flash-induced kinetics in R-26 and WT. This allowed us to both observe the optimal rate constant of P^+ reduction at the maximum concentration of Mn^{2+}, and the binding of Mn^{2+} to the BRC from the full titration. The results can be seen in Figure 3.9. As these samples were Q_B active, the kinetics was found to be biphasic, with the slower component due to BRCs in the $P^+Q_B^-$ state, and the more rapid component due to those in the $P^+Q_A^-$ state. The amplitude of the slower component fell, in favor of the faster component, as the concentration of Mn^{2+} increased. This behavior followed the binding equations 2.5.5 and 2.5.6 for the fast and slow components, respectively. Fits to these equations suggested 2 Mn ligands, and gave identical K_Ds (within uncertainty) for both components, with a K_D of 4.1 mM and 3.9 mM for R-26 and WT, respectively. The rate constants of the fast component were also elevated by the presence of Mn^{2+}, from 8.0 s^{-1} in the absence of Mn, to a maximum of 9.5 s^{-1} and 10.7 s^{-1} in the presence of 30 mM Mn^{2+} for R-26 and WT, respectively.

While the results of the titration clearly show the binding of Mn^{2+} to the BRC, the nearly complete drop in relative amplitude of the slower component, assigned to charge recombination from the $P^+Q_B^-$ state, with the nearly saturating rise of the relative amplitude of the faster component, could be interpreted in two ways. Mn^{2+} could either be reducing P^+ with a similar rate to that of $P^+Q_A^-$ charge recombination, or the presence of the bound Mn^{2+} could be changing the dominant pathway of charge recombination, from the $P^+Q_B^-$ state to the $P^+Q_A^-$ state. A follow up experiment, examining the consequences of Mn^{2+} ET to P^+ at these rate constants, will distinguish between these two possibilities in the next section.

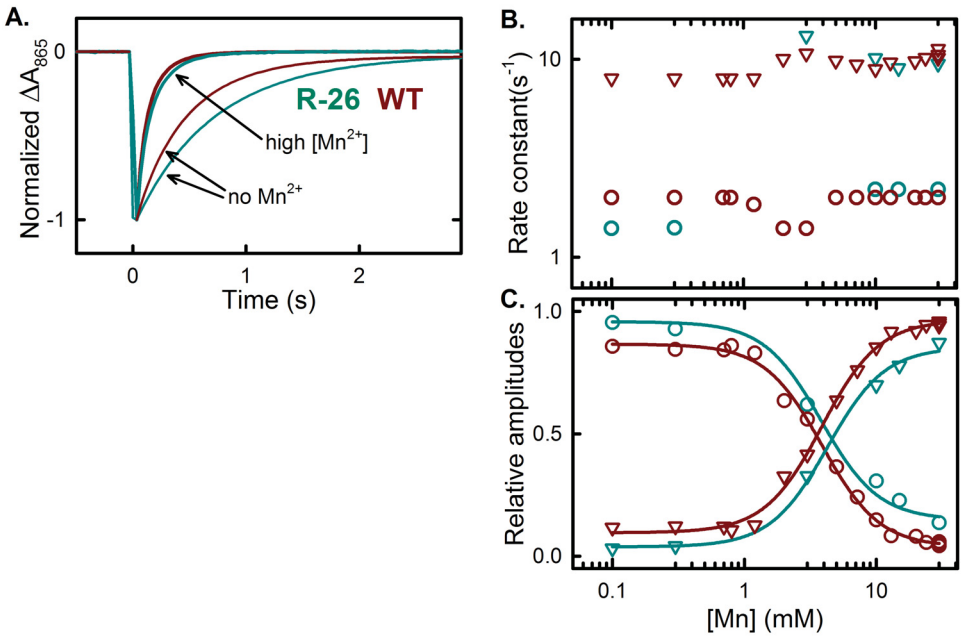

Figure 3.9: Flash-induced kinetics of P^+ reduction in the presence of Mn^{2+} for R-26 and WT. A: representative traces of P^+ reduction kinetics after flash excitation in R-26 (blue-green traces) and WT (brown traces) at high and low concentrations of Mn^{2+}. B: rate constants as a function of Mn^{2+} concentration. Circles correspond to rate constants of 1.4 - 2.2 s^{-1} , which are assigned to $P^+Q_B^-$ charge recombination, and triangles correspond to rate constants of ~8 - 13 s^{-1}, which are assigned to faster $P^+Q_A^-$ charge recombination. Brown symbols represent WT BRCs and blue-green symbols represent R-26. C: Relative amplitudes of fast and slow components. Lines show fits to binding equations 2.5.5 and 2.5.6 for 2 Mn ligands, yielding K_Ds of 3.9 mM and 4.1 mM for WT and R-26, respectively. K_Ds were identical, within uncertainty, for fast and slow components. Conditions: 1 μM BRC, in 0.03 % LDAO, 80 mM BTP at pH 9.4, 30 μM UQ_{10}, and varying concentrations of Mn^{2+}.

3.3.1.2 Electron transfer path following flash excitation

As the kinetics of P^+ recovery following flash excitation at saturated binding of Mn^{2+} had rate constants similar to those of charge recombination in the absence of manganese, ~1 s^{-1} from the $P^+Q_B^-$ state and ~10 s^{-1} from $P^+Q_A^-$ state,[58] we needed to distinguish whether this recovery was due to ET from Mn^{2+} to P^+, or a modified charge recombination due to the presence of the bound Mn^{2+}. The rapid component of these kinetics had a rate constant faster than that of charge recombination from the $P^+Q_A^-$ state in the absence of Mn (9.5 - 10.7 s^{-1} with Mn^{2+} compared to 8.0 s^{-1} without). Therefore, if this recovery were due to ET from Mn^{2+}, a single flash would trap the majority of BRCs in the $P(Q_AQ_B)^-$ state†, which has a recovery

†Note: in the $P(Q_AQ_B)^-$ state the recovery rate will be similar whether the electron resides on Q_A or Q_B, as ET between the quinones is much faster than recovery of the PQ_A^- state even in the energetically unfavorable direction (6 - 150 μs compared to several minutes).[61] We therefore generally do not distinguish between these two possibilities, and instead refer to the state as PQ^-.

time of several minutes (as discussed in Section 1.3 of the Introduction). This scenario is depicted in the following reaction scheme:

$$PQ : Mn^{2+} \overset{h\nu}{\rightleftharpoons} P^{+}Q^{-} : Mn^{2+} \rightharpoonup PQ^{-} : Mn^{3+} \tag{3.3.1}$$

Where $h\nu$ denotes a photon excitation of P, and $PQ : Mn$ denotes the BRC with a bound Mn ion.

The NIR absorption spectrum of the PQ^- state is significantly different from both that of the P^+Q^- state, and the PQ state. We should therefore be able to distinguish between Mn^{2+} ET, and P^+Q^- charge recombination by the presence or absence of a PQ^-/PQ difference spectrum immediately after a flash. Figure 3.10 A shows a representative spectrum of what we observed after a single flash excitation (black trace). No PQ^-/PQ signal can be seen, despite the fact that the majority of the BRCs should be in this state.

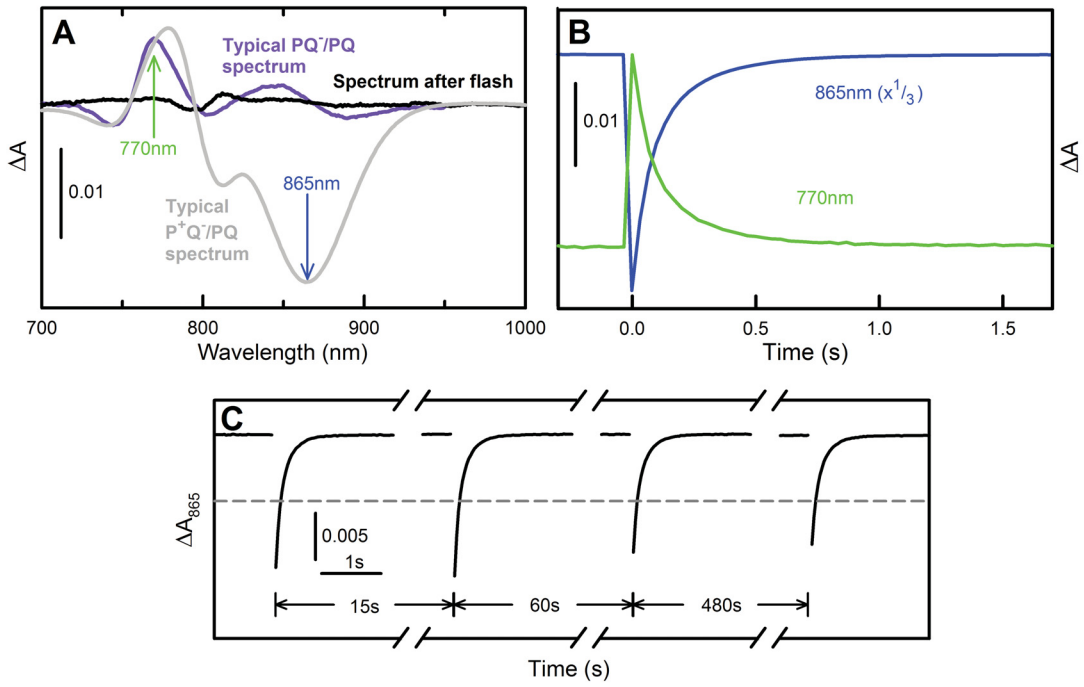

Figure 3.10: Influence of Mn^{2+} on the flash-induced light - dark optical difference spectrum and on the kinetics of charge recovery. A: light - dark optical difference spectrum immediately after excitation by a flash (black trace) compared to spectra typical of the PQ^- (purple trace) and P^+Q^- states (light grey) of the BRC. Colored arrows indicate the wavelengths where time-resolved absorbance changes are monitored in the following panel. B: flash-induced kinetics monitored at wavelengths where the greatest change in absorbance is expected for the P^+Q^- state (865 nm) and the PQ^- state (770 nm). C: multi-flash kinetics monitored at 865 nm. The time interval between flashes was varied as indicated by arrows. Grey dashed line indicates 50 % amplitude of the first flash, as variations of ~50 % amplitude between flashes would be expected for rapid Mn^{2+} reduction of P^+ (see text). Data for R-26 shown. WT showed similar results and has been left out for clarity. Conditions: 1 μM R-26 in 0.03 % LDAO, 80 mM BTP at pH 9.4, and 30 mM Mn^{2+}.

The search for PQ^- state formation after flash excitation was then probed with greater time resolution, measuring the kinetics of flash excitation at wavelengths corresponding to the greatest absorbance changes of the P^+Q^- state, at 865 nm, and the PQ^- state, at 770 nm (see arrows in Figure 3.10 A). These kinetics showed similar rapid recoveries, as seen in Figure 3.10 B, with bi-phasic rate constants of 10.0 ± 0.2 s^{-1} for the faster component, accounting for 90 % of the total amplitude, and 2.0 ± 0.1 s^{-1} for the slower component. The similarity of both the bi-phasic nature, and the rate constants of recovery, at these two wavelengths suggest P^+ is recovering through charge recombination from the $P^+Q_A^-$ state rather than reduction by Mn^{2+}.

We performed one additional experiment to probe for Mn^{2+} ET to P^+ during flash excitation, this time by performing multiple consecutive flashes and looking for differences in the the light-induced kinetics at 865 nm (panel C). Monitoring the kinetics of multiple flashes should expose P^+ reduction by Mn^{2+} from the large, systematic variation in amplitude of P^+ formation. This amplitude should vary by ~50 % over consecutive flashes, as any BRCs that were reduced by manganese would be trapped in the PQ^- state, and further flashes would only yield charge separation in the P^+H^- state, which has a lifetime of 20 ns, and would thus be unobservable to us. As the PQ^- state recovers in 5-10 minutes (see Figure 3.7), flashes separated by only a few seconds should mostly probe the PQ^- state and would, therefore, induce kinetics with a large drop in amplitude, while flashes separated by several minutes should probe BRCs that have mostly recovered to the PQ state, and would induce kinetics closer to that of the first flash. The total amplitude of P^+ formation for each flash can be seen in the traces of panel C. While some variation is observed (a maximum of 17 % from the first flash), this is within the expected fluctuation due to the sampling rate of the spectrometer being close to the rates measured. It is also far from the systematic ~50 % variation in amplitude expected from manganese electron donation. We therefore have additional evidence suggesting the kinetics of P^+ recovery after flash excitation are due to charge recombination and not ET from Mn^{2+}.

The conclusions of this and the previous results clearly demonstrate that flash excitation leads only to charge recombination, having rate constants of ~10 s^{-1} for recovery of the $P^+Q_A^-$ state, and a rate constant of ~2 s^{-1} for recovery of the $P^+Q_B^-$ state. From the total lack of Mn^{2+} oxidation, we can also conclude that the rate constant of Mn^{2+} ET to P^+ must be slower than both of these rate constants, and not have time to occur during a single flash excitation.

3.3.2 Obtaining the rate constant of electron donation from bound manganese

As shown in the previous section, flash excitation did not provide a charge separated state with a long enough lifetime for ET from Mn^{2+} to the dimer to take place. To mitigate this we moved to continuous illumination to determine the kinetic information of this electron transfer. The reaction scheme of Equation 3.3.1 can be elaborated to show the rate constants

of each process as:

$$PQ : Mn^{2+} \underset{k_{recomb}}{\overset{k_{light}}{\underset{h\nu}{\rightleftharpoons}}} P^+Q^- : Mn^{2+} \overset{k_{Mn}}{\rightharpoonup} PQ^- : Mn^{3+} \tag{3.3.2}$$

We are interested in the rate constant of Mn^{2+} ET to P^+, k_{Mn}. However, when we determine rate constants of electron transfer through P^+ reduction kinetics (monitoring absorbance changes at 865 nm), they are affected by the other processes. To understand how this happens, it is helpful to first examine this process in the absence of manganese. In this case when the sample is first illuminated an equilibrium between the PQ and P^+Q^- states of Equation 3.3.2 is reached, which is determined by the ratio of the photochemical rate constant, k_{light}, which is dependent on the illumination intensity, and the rate constant of charge recombination, k_{recomb}:

$$\frac{[PQ]}{[P^+Q^-]} = \frac{k_{recomb}}{k_{light}} \tag{3.3.3}$$

If manganese is introduced it becomes an additional drain for the P^+Q^- state and will compete with charge recombination to reduce P^+. The reduction mechanism of P^+ will then be split between these drains, with a ratio determined by their relative rate constants. To avoid this split in the P^+ reduction mechanism we must effectively remove the drain of charge recombination, which is equivalent to shifting the PQ/P^+Q^- equilibrium nearly completely to the P^+Q^- state. This can be accomplished by increasing the light intensity of illumination, which will in turn increase k_{light} and make the ratio in Equation 3.3.3 approach zero. At this point the first reaction of Equation 3.3.2 has effectively become one way and the kinetics of P^+ decay will be exclusively dependent on the sole drain, ET from Mn^{2+} to P^+. As long as Equation 3.3.3 is kept near zero, the kinetics will also be effectively independent of light intensity, providing us with a way of knowing when we have reached high enough intensities.

We accomplished this in practice by monitoring the kinetics of P^+ reduction at several light intensities, as seen in Figure 3.11. We found that the rate constant of P^+ recovery increased until saturation at an intensity of ~0.95 W/cm^2, yielding maximum rate constants (corresponding to the rate constants of ET from Mn^{2+}) of 1.3 s^{-1} and 0.8 s^{-1} for R-26 and WT, respectively. Interestingly, the large difference between the rate constants of electron donation from manganese to P^+ in WT and in R-26 disappeared upon addition of high-concentration LDAO (7 %), with the rate constant of WT remaining the same and that of R-26 falling to 0.7 s^{-1}. This is consistent with observed difference in LDAO binding between WT and R-26, and a possible explanation for this will be provided in Section 4.2.2.2.

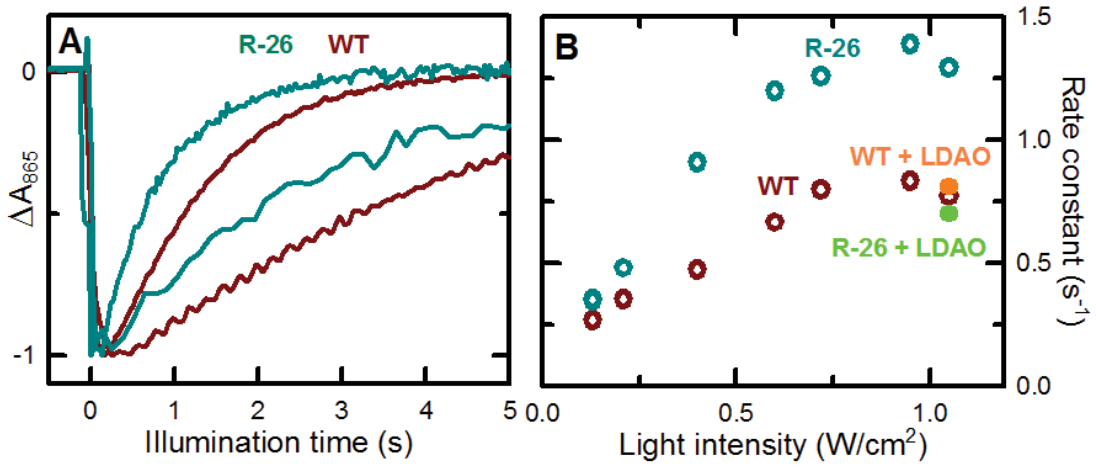

Figure 3.11: Light intensity dependence of the kinetics of P^+ reduction in the presence of Mn^{2+}. A: Kinetics of P^+ recovery during continuous illumination in WT (brown) and R-26 (blue green) BRCs. Slower traces recorded with low (0.13 W/cm^2) light intensity and more rapid traces recorded with high (0.95 W/cm^2) light intensity. B: observed rate constant of P^+ reduction as a function of light intensity in BRCs from WT (brown open symbols) and R-26 (blue-green open symbols) BRCs. Closed, lighter colored symbols show the rate constant at maximum intensity with excess (7 %) LDAO. Conditions: 1 μM BRC in 0.03 % LDAO, 80 mM BTP at pH 9.4, and 30 mM Mn^{2+}.

3.3.3 Electron transfer kinetics modulated by the occupation of Site 1

In Section 3.2 we found spectral evidence of a bound photochemically-oxidized Mn^{3+} near Site 1. As the previous section gave us an understanding on the kinetics of ET from Mn^{2+} to P^+, we next looked for evidence of these kinetics originating at Site 1, a more direct confirmation that the secondary electron donor of the BRC is in fact the Mn^{2+} located at this site. We therefore investigated the effects of the probe molecules with access to Site 1, from Section 3.2.2, on the kinetics of Mn^{2+} electron transfer to P^+. We first performed a qualitative comparison of these kinetic effects under weak (0.13 W/cm^2) continuous illumination, as this allowed us to compare our results with a wealth of data previously collected under these conditions. The electron transfer kinetics were found to be most significantly affected by the presence of two of these molecules, quinone UQ_{10} and terbutryne, as can be seen in Figure 3.13 A.No significant results were found for NaCl, TX-100, or LDAO (data not shown). The P^+ reduction kinetics of BRCs with and without manganese can be seen as blue-green and pink traces, respectively, in panel A of Figure 3.13. These kinetics were drastically slowed with the addition of UQ_{10} or terbutryne, an inhibitor of the BRC which competitively binds to the secondary quinone (Q_B) binding site, (yellow and orange traces). One would expect a large impact on P^+ reduction with the addition of excess quinone to the BRC, as it would then be able to complete the quinone cycle (see Figure

3.12), replacing doubly reduced quinol (QH_2) with oxidized quinone (Q) from the quinone pool, and providing further opportunity for the photo-oxidation of P. However, this is clearly not the only cause for the modified kinetics, as upon addition of terbutryne, which inhibits the quinone cycle,[53] the kinetics slowed even further. It, therefore, seems that the strong effects that these molecules have on the kinetics of P^+ reduction by Mn^{2+} is more due to their presence near Site 1 than their effects on the quinone cycle.

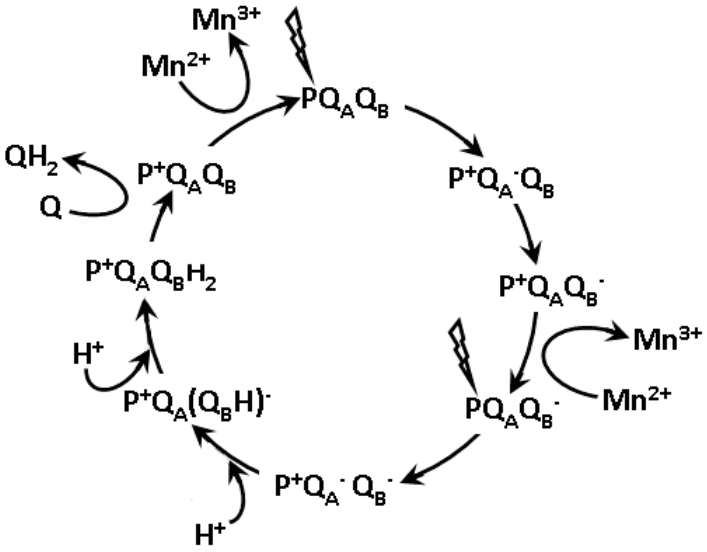

Figure 3.12: Quinone cycle of the BRC in the presence of a manganese (II) secondary electron donor. BRC starts in the neutral PQ_AQ_B state and goes through charge separation following absorption of a photon, eventually leading to the $P^+Q_AQ_B^-$ state. Mn^{2+} reduces P^+, and the cycle repeats once more, with Q_B also taking up 2 protons. The doubly reduced, doubly protonated Q_B is then replaced by an oxidized Q from the Q pool, and the cycle is reset.

We also compared these kinetics to those taken previously under similar conditions, but with BRCs incorporated into liposomes in place of detergent micelles[20] (panel B of Figure 3.13). In this case the barrier to the hydrophobic midsection of the BRC had been changed from that of a loosely spaced, zwitterionic detergent belt to that of the more tightly packed liposome vesicles, as described in Section 1.2.3 of the Introduction. These liposomes were made of lipids with positive (DOTAP), negative (DOPG) and neutral (DOPC) headgroups, in which the difference between these lipids manifested itself as liposomes with tighter or looser sealing. This change in structure and accessibility of the BRC's membrane region, including Site 1, induced slowing of 1-2 orders of magnitude in kinetics for all but the liposomes made from lipids with negatively charged headgroups, which were only slightly slower than those of BRCs in micelles. The large retarding effect on kinetics upon lowering the accessibility of Site 1 provides further evidence of the manganese electron donor being bound here.

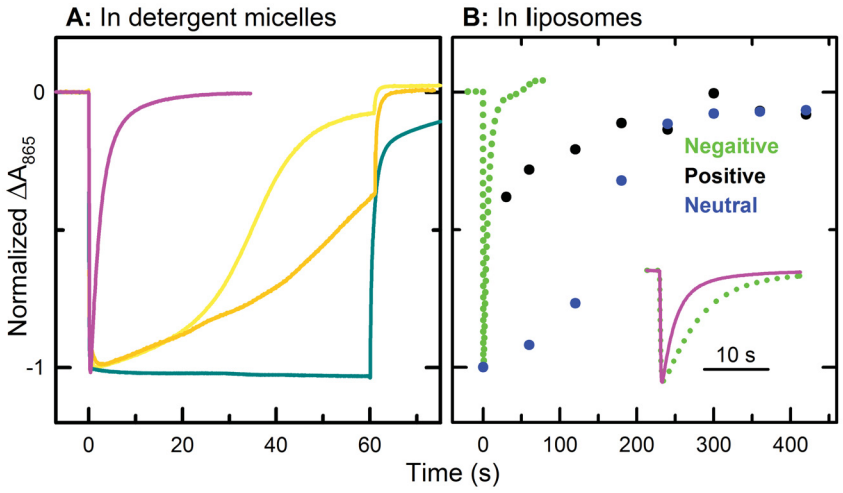

Figure 3.13: Effects of molecules with access to Site 1 on the kinetics of P^+ reduction by Mn^{2+} under continuous illumination. Solid lines: BRCs incorporated into detergent (LDAO) micelles, dots: BRCs incorporated into liposomes. Pink trace: pre-illuminated BRC with 30 mM Mn^{2+}, yellow trace: additional 30 μM UQ_{10} added, orange trace: 100 μM terbutryne added, blue-green trace: no manganese. Green dotted trace: liposomes formed from lipids with negatively charged headgroups, black symbols: liposomes formed from lipids with positively charged headgroups, blue symbols: liposomes formed from neutral lipids. Kinetics normalized to absorbance change promptly upon illumination. Liposome data taken from Lag.[20] Conditions: 1 μM R-26 in 0.03 % LDAO detergent, or DOPG, DOTAP, or DOPC liposomes. Continuous illumination excitation of 0.13 W/cm^2 white light.

Upon finding evidence of these molecules affecting the kinetics of Mn^{2+} ET to P^+, we characterized the extent of each molecule's effect by performing a titration of the molecule while monitoring the P^+ reduction kinetics under continuous illumination. High-intensity excitation was used for this study, to more accurately follow the rate of Mn^{2+} electron transfer (see Section 3.3.2). In Figure 3.13 we observed a huge effect from the presence of both quinone UQ_{10} and terbutryne, a molecule which competitively binds to the binding site of Q_B, inhibiting secondary quinone function in the BRC.[53] To further probe the strong dependence of the occupation of this site we included another quinone, UQ_0, in this study, along with the previously used molecules. UQ_0 is particularly interesting because with its lack of an isoprene tail, it is much less hydrophobic, and therefore has a much weaker affinity to the BRC of *R. sphaeroides*. It is also not able to bind to the Q_B binding site above a pH of ~8.5, and therefore the BRC cannot perform the full quinone cycle to produce quinol.[63] The results of these titrations can be seen in Figure 3.14. Panel A and B show, respectively, the fraction of recovered P after 10 s of illumination, and the rate constant, as a function of the concentration of molecule added. Panels C through G show the kinetic traces themselves at varying concentrations. All of the molecules tested had a retarding effect on the rate constants, the fraction of recovered P, or both, and all effects were monotonic, therefore the slowest trace corresponds to the highest concentration of added molecule. For the quinones, the fraction of recovered P^+ after

10 s could be modeled with binding equation 2.5.6 (solid lines in panel A). These fits yielded 1 and 2 binding molecules, and dissociation constants of 130 μM and 8.4 μM for UQ_0 and UQ_{10}, respectively. While LDAO, NaCl, and terbutryne did have observable effects on the kinetics, their behaviors were more complex and we were unable to quantitatively characterize them with these titrations.

The slowing effect of each of these molecules, which have access to Site 1, on the kinetics of ET from Mn^{2+} to P^+ provides further evidence that the Mn electron donation originates from Site 1. An explanation of the different effects from the various agents used will be offered in Sections 4.2.3 and 4.4.1.1.

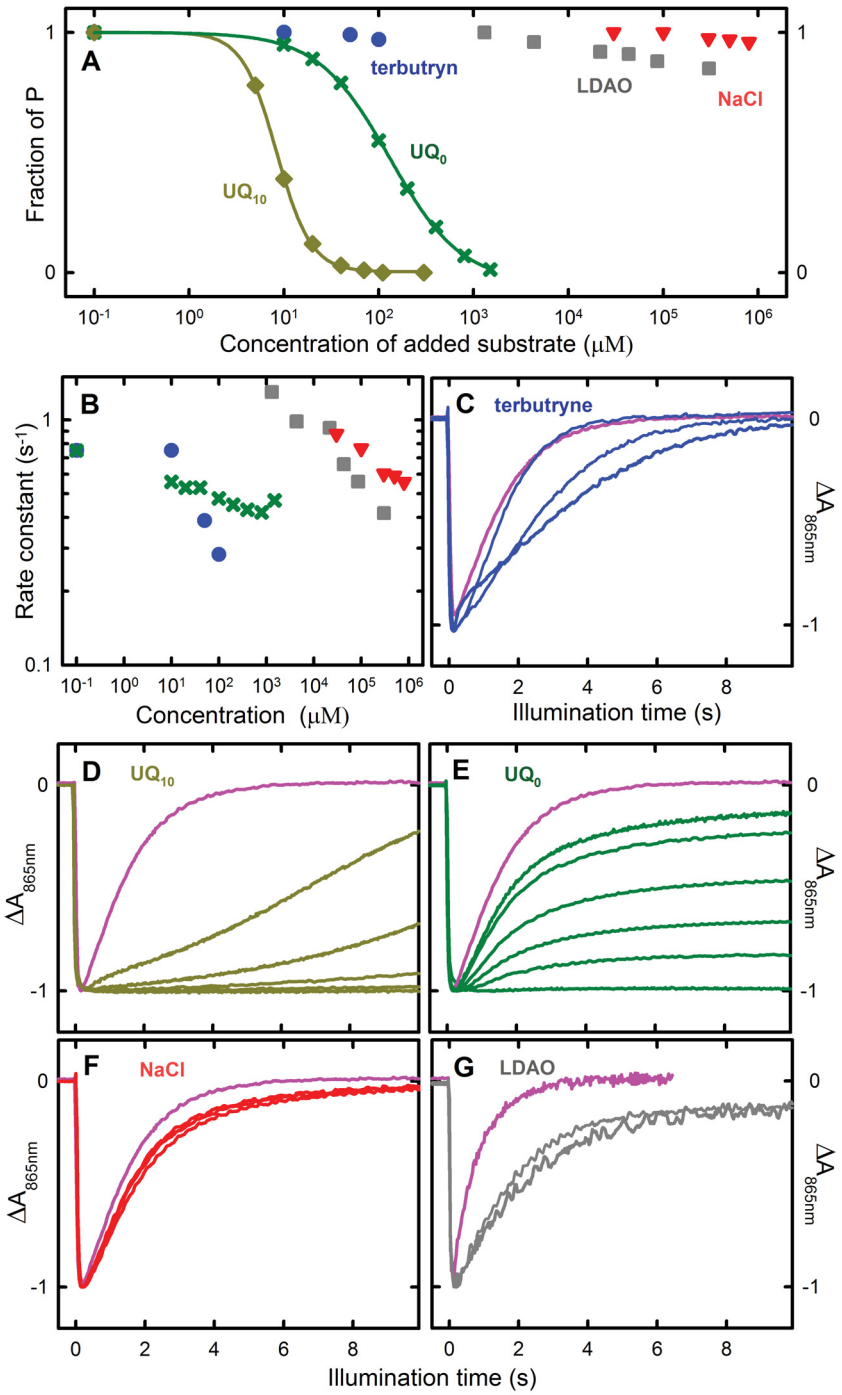

Figure 3.14: Probe molecule concentration dependence of the kinetics of P^+ reduction by Mn^{2+}. A, B: fraction of reduced P^+ and rate constant as a function of probe concentration, respectively. Solid lines represent fits to binding equation 2.5.6 with 1 molecule binding for UQ_0, and 2 for UQ_{10}. C-G: overlays of kinetic traces before addition (pink trace) and at probe concentrations depicted in panels A and B. All probes had a monotonically retarding effect on kinetics, therefore slower traces represent higher probe concentrations. All titrations were conducted with WT BRCs except for the LDAO titration of panel G, as LDAO does not affect WT kinetics. Conditions: 1 μM BRC in 0.03 % LDAO, 80 mM BTP at pH 9.4, 30 mM Mn^{2+}. High-intensity (1.05 W/cm^2) continuous illumination was used to induce photochemical kinetics.

3.4 Probing for electron donation from manganese at Site 2

It had previously been shown that the P^+ reduction rate after flash excitation in the presence of cyt c^{2+} was slowed significantly, giving time constants of ~110 ms when Mn was present, which was assigned to ET from Mn^{2+} to P^+.[24] In lieu of the lack of ET from Mn^{2+} observed during flash excitation (see Figure 3.10), we decided to extend this study by monitoring P^+ reduction in the presence of cyt c^{2+} with both nanosecond laser excitation and continuous illumination excitation. The resulting kinetics, including the original data using millisecond flash excitation, are shown in Figure 3.15. Under ideal conditions cyt c^{2+} donates an electron to the BRC in ~1 μs for bound cyt c and ~10 μs for collisional cyt c.[64] However, cyt c is known to lose protons above pH 9.2, and gradually become inactive at higher pHs.[65,66] As we are working at pH 9.4, we first measured the kinetics of ET from cyt c^{2+} to P^+ without manganese. This was measured with our laser flash photolysis instrument, and gave biphasic kinetics (red inset), composed of 50 % fast component, with a time constant of 720 μs, and 50 % slow component, with a time constant of 7.3 ms, a slowing of nearly 3 orders of magnitude from optimal conditions. We then monitored the kinetics of P^+ reduction in the presence of Mn^{2+}, and cyt c^{2+} with Mn^{2+}, under continuous illumination. We found that samples with cyt c^{2+} exhibited much faster kinetics (160 ms) than those with only Mn^{2+} (780 ms). Therefore while the rate constant of cyt c ET is slowed by over 1 order of magnitude (160 ms compared to 7.3 ms) in the presence of manganese, it is not completely deactivated. While this retardation gives further support for the presence of a bound manganese at Site 2, the lack of observation of P^+ reduction from Mn^{2+} in the presence of cyt c^{2+} provides no evidence of ET to P^+ from manganese bound to this site.

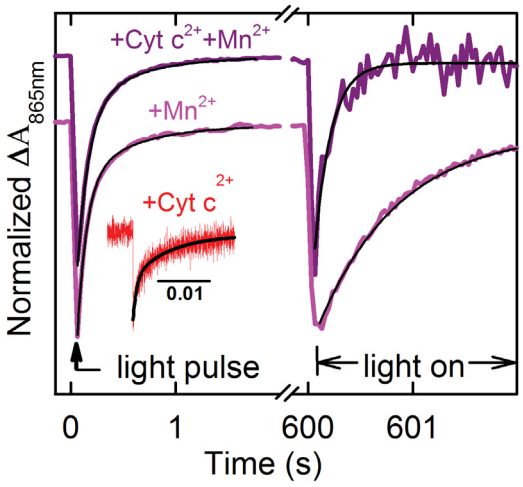

Figure 3.15: The effect of the presence of Mn^{2+} on the electron transfer kinetics from cyt c^{2+} to P^+. Red inset: P^+ recovery kinetics after laser flash excitation in the presence of cyt c^{2+}. Fits (black lines) gave a biphasic recovery with lifetimes of 50 % 720 μs, and 50 % 7.3 ms. 1st excitation (left side): P^+ recovery kinetics after flashbulb excitation in the presence of cyt c^{2+} and Mn^{2+} (purple lines) had a similar recovery to that in the presence of Mn^{2+} only (pink lines). Fits gave biphasic recoveries with the rapid components accounting for 80 % of the total amplitude, and having a lifetimes of 90 ms and 111 ms for Mn^{2+} only and cyt^{2+}+Mn^{2+}, respectively, and both slow components having lifetimes of 500 ms. 2nd excitation (right side): P^+ recovery kinetics under high-intensity continuous illumination excitation was much more rapid in the presence of cyt c^{2+} and Mn^{2+} than in the presence of Mn^{2+} only, having monophasic recoveries with lifetimes of 160 ms compared to 780 ms, respectively. Conditions: 1 μM WT in 0.03 % LDAO, 80 mM BTP pH 9.4, 30 μM cyt c^{2+} and/or 30 mM Mn^{2+}. Millisecond flash data taken from Ivanescu.[24]

3.5 Composition of the manganese-bis tris propane complex

Along with better resolving the interactions between the Mn-BTP complex and the BRC, we also further elucidated the structure of the complex itself. With the inability to use more direct imaging techniques, as 80 mM BTP is a much too high buffer concentration for mass spectrometry, and the unavailability of the time, expertise, and infrastructure required of x-ray crystallography, we resorted to less direct methods, studying the composition and function of the Mn-BTP complex. While these methods were unable to reveal the full chemical structure of our complex, they still yielded useful information on it.

3.5.1 Stability of the complex

As we spanned a large spectrum of concentrations during the manganese titration of Figure 3.16, and evidence of a Mn-BTP complex capable of reducing the oxidized dimer had not been previously observed at these lower concentrations, we decided to determine the stability of the Mn-BTP complex over a similar span of concentrations. To accomplish this we monitored the

optical absorption bands of the Mn-BTP complex at various concentrations. As the oxidized complex has an additional absorption band overlapping that of the reduced complex, (~265 nm compared to 236 nm; see Figure 3.18 for more details), care had to be taken to avoid auto-oxidation of the complex, which would corrupt the measured spectrum with a contribution from this band. All measurements were, therefore, taken immediately upon preparation of the complex, and each measurement was repeated numerous times. The strongest peak associated with the Mn-BTP complex was found to be in the UV, at 236 nm. The spectra, and the extinction coefficients as a function of manganese concentration are shown in Figure 3.16. A significant change in the extinction coefficient of this band would suggest a dissociation of the Mn-BTP complex, and thus a skewing of the previous manganese titration result. However no variation of the extinction coefficient greater than experimental uncertainty is visible.

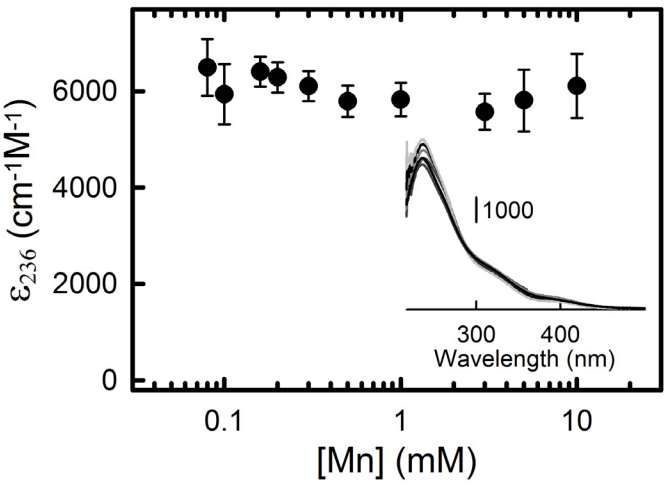

Figure 3.16: Stability of the UV absorption spectrum of the Mn-BTP complex at various manganese concentrations. Inset: UV-Vis spectrum of the Mn-BTP complex. Main figure: extinction coefficient of the strongest peak (236 nm) as a function of manganese concentration. Conditions: 80 mM BTP at pH 9.4, 0.03 % LDAO, and varying concentrations of Mn^{2+}.

3.5.2 Evidence of a homogeneous manganese complex

The accessibility of the Mn-BTP complex to the binding sites of the BRC will be limited by the size of this complex, and its total charge, dictated by the number of Mn ions of the complex, and their oxidation states. While we could not measure any of these parameters directly, we were able to test for the number of different manganese species of the complex by looking at its magnetic and redox properties. As the complex is able to bind to Site 1 of the BRC, it must be fairly small. It is, thus, unlikely that multiple manganese ions could be present on the complex without affecting each other's magnetic and redox properties, and making them distinguishable. Therefore the number of distinguishable manganese species of the Mn-BTP

complex is most likely also the total number of manganese ions of the complex. We first determined the number of manganese species of the Mn-BTP complex by taking electronic paramagnetic resonance (EPR) spectra of the complex[‡], and comparing this to a water soluble hexa-aqua manganese ($Mn(H_2O)_6$) spectrum, which contains a single manganese ion. As EPR provides a spectrum of the energy levels of the electronic spin states of paramagnetic atoms, such as manganese, we should be able to detect the presence of multiple species of manganese as a splitting of the energy levels of the single manganese spectrum. The two spectra can be seen in Figure 3.17. No splitting in the peaks, or difference in peak width from the $Mn(H_2O)_6$ complex is visible in the spectrum of the Mn-BTP complex. This, therefore, suggests a homogeneous complex, most likely containing a single manganese ion.

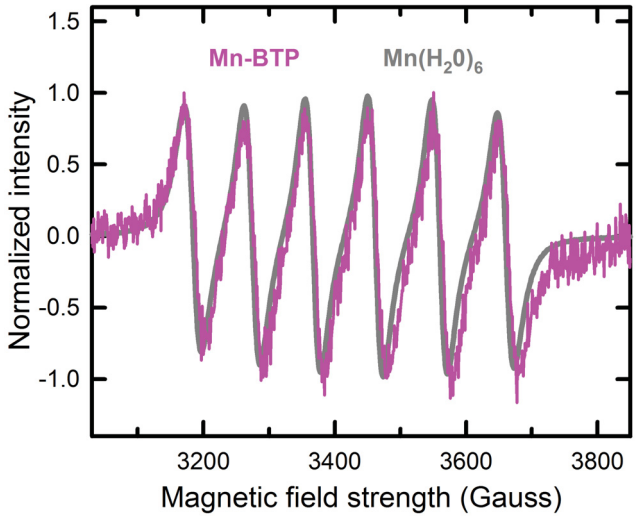

Figure 3.17: Normalized X-band EPR spectra of the Mn-BTP complex and the water soluble hexa-aqua manganese complex. Grey lines: hexa-aqua manganese, pink lines: Mn-BTP complex. Spectra have the same widths and number of peaks. The $Mn(H_2O)_6$ spectrum has been red-shifted by 45 Gauss to facilitate comparison. This will not affect our conclusions as the number of manganese species will depend on the width of the peaks but not the position. Conditions: pink: 5 mM Mn^{2+} in 80 mM BTP pH 9.4 and 0.03 % LDAO; grey: 1 mM Mn^{2+} in 10 mM CHES pH 9.0 and 0.05 % TX-100. Recorded at ~9.61 GHz. Measurements of Mn-BTP samples taken by Li and Andronenko.

We also confirmed the homogeneous composition of the Mn-BTP complex by measuring the redox potential of the Mn^{2+}/Mn^{3+} couple of the complex. As we have shown evidence of electron transfer from the Mn-BTP complex to P^+, this complex must have a Mn^{2+}/Mn^{3+} potential below that of the P/P^+ potential (found to be 505 mV in the absence of manganese, or 555 mV in the presence of manganese, at our conditions[24]). Therefore a homogeneous complex should have exactly one Mn^{2+}/Mn^{3+} potential between 0 mV applied potential (243 mV rela-

[‡]Measurements of Mn-BTP samples were taken with the kind help of Li and Andronenko.

tive to standard hydrogen electrode) and 555 mV. We verified this by measuring absorbance changes in the UV spectrum of the Mn-BTP complex, where Mn^{3+} is known to absorb under our conditions,[24] while applying a potential, which was varied across this range of interest. Specifically, the increase in amplitude of the absorption peaks at 265 nm and 341 nm, as well as the shift of the peak, which is found at 248 nm at our conditions, and shifts to 265 nm upon applying an oxidation potential, were monitored. Measurements were carried out in the same electrochemical redox cell as Section 3.1.1. We then plotted the normalized changes in peak amplitude and the peak position as a function of applied potential. These plots can be seen in Figure 3.18, with their associated spectra being shown in the insets. Both data were fit with a Nernst equation (Eq. 2.5.7) yielding midpoint potentials (E_m) of 379 mV and 398 mV for the amplitude of the 265 nm and 341 nm peak, respectively, and 396 mV for the 265 nm peak shift. The close agreement between the E_m attained from the 341 nm peak and the 248 nm - 265 nm peak shift supports the Mn-BTP complex being composed of a single species of manganese. Further discussion on the variation in these results will be given in Section 4.5.2.

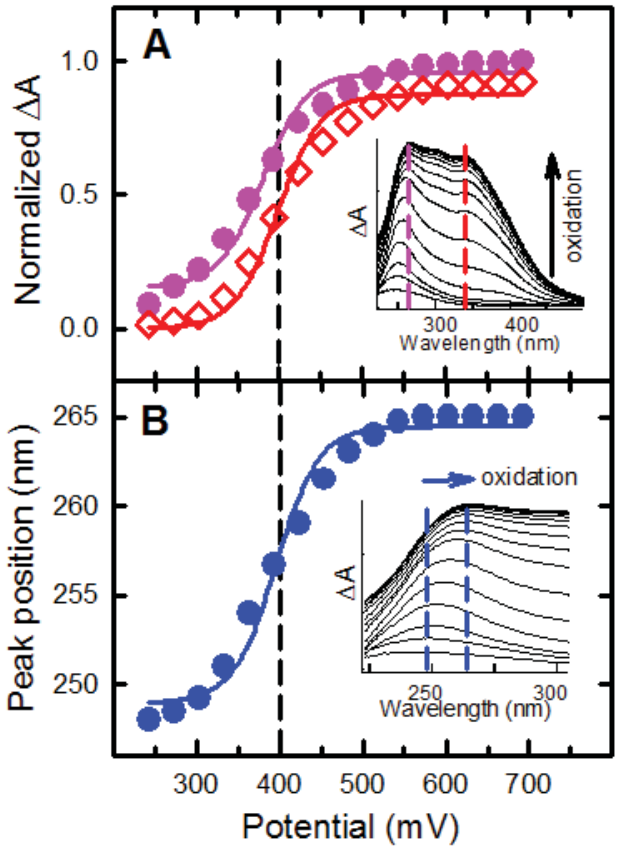

Figure 3.18: Electrochemical potential of the Mn^{2+}/Mn^{3+} redox couple in the Mn-BTP complex. A: determination of the potential by monitoring the amplitude of the UV absorbance peak at 341 nm and 265 nm, assigned to the oxidized (Mn^{3+}) Mn-BTP complex, as the applied potential is varied. B: determination of the potential by monitoring the shift of the highest energy peak, from 248 nm to 265 nm. Pink closed symbols represent the 265 nm peak, red open symbols represent the 341 nm and blue closed symbols represent the peak position shift from 248 nm to 265 nm. The insets shows the difference spectra at several applied potentials, with the colored dashed lines marking the corresponding monitored spectral features. Solid lines represent fits to a Nernst equation, with the 265 nm peak, the 341 nm peak and the 248 nm - 265 nm shift having midpoint potentials of 379 mV, 398 mV and 396 mV, respectively. Conditions as for Figure 3.2, but without BRC.

4

Discussion

Manganese has recently been shown to be able to act as a secondary electron donor to native bacterial reaction centers, through coordination by BTP into a complex with a much lower redox midpoint potential. This is particularly interesting as the incorporation of a coordinated manganese complex by the BRC shows a resemblance to the oxygen evolving complex (OEC) of PSII, a manganese calcium complex which catalyzes the splitting of water. There is therefore a potential to offer an alternative pathway of the evolution of anoxygenic photosynthetic organisms, containing BRC-like RCs, into oxygenic ones, containing PSII-like RCs, which would not require several simultaneous mutations, or other unlikely assumptions, as in other proposed pathways.[6,7,28,67] In this work we have resolved many details of this Mn-BRC coupling, determining the binding sites of manganese in the BRC, the redox activity of these bound ions, and the rate of electron donation, along with learning more about the Mn-BTP complex itself. In this discussion we attempt to incorporate these results into a consistent model of manganese binding and electron donation to the BRC, and examine the evolutionary feasibility and implications of this model.

4.1 Evidence of manganese binding

4.1.1 Site 1

Evidence was found for the binding of manganese to two sites previously predicted by ligand binding site modeling software. Manganese binding to Site 1 was confirmed by the spectral changes in the Q_y bands, induced by the presence of Mn^{2+} (see Figure 3.2). The binding location was first restricted to the proximity of the positions and axes of the Q_y dipoles responsible for these bands, and then further localized to the vicinity of the carotenoid binding site, from the influence of the carotenoid on these spectral changes. The intersection of these spatial requirements is at, or very close to Site 1 (see dipole directions and carotenoid molecule of panels A and B).

In R-26 BRCs, the observed effects on the Q_y bands of P and B, and the lack of an effect on the Q_y band of H (panel C), are as to be expected for a bound ion to Site 1, as a Mn bound here would interact with the Q_y dipoles of P and B pointing through this site. However, WT BRCs show quite different effects, with a blue shift of the H band, and a blue shift of the B band instead of a broadening. This could be due to steric interference by the carotenoid, which can be seen to occupy a large part of the binding site. In fact the carotenoid completely blocks a small cavity leading to the protein's exterior, which could provide an optimal point of access to the manganese ion. The presence of the carotenoid may, therefore force manganese to bind elsewhere in this large cavity, changing the cation's position relative to the Q_y dipoles of B and H, and giving rise to the observed shifts.

The carotenoid cofactor has been previously shown to have a similar negative impact on binding near this same site, for lipids.[51] In this case lipid binding was detected by a red shifted H band in the light - dark difference spectrum, in the absence of a secondary donor. This shift was only observed in conditions which have been shown by crystallographic structures to coincide with an inward orientation of the 2-acetyl group of B_B (see Figure 4.1). In R-26 BRCs this group was found to be pointing inward when the carotenoid binding site was occupied by an LDAO molecule,[49] and outward when the carotenoid binding site was vacant.[68] In WT the orientation was dependent on the type of carotenoid bound, with the occupation by a spheroidene molecule, that which is produced by anaerobic growth and would be present in our samples, yielding an outward orientation of the acetyl group.[52,68,69] As these conditions for lipid binding match those that we have observed for Mn binding, a gatekeeping action by the 2-acetyl group of B_B may be the true molecular mechanism for the impairment of Mn binding to Site 1, with the other factors just determining the orientation of this group.

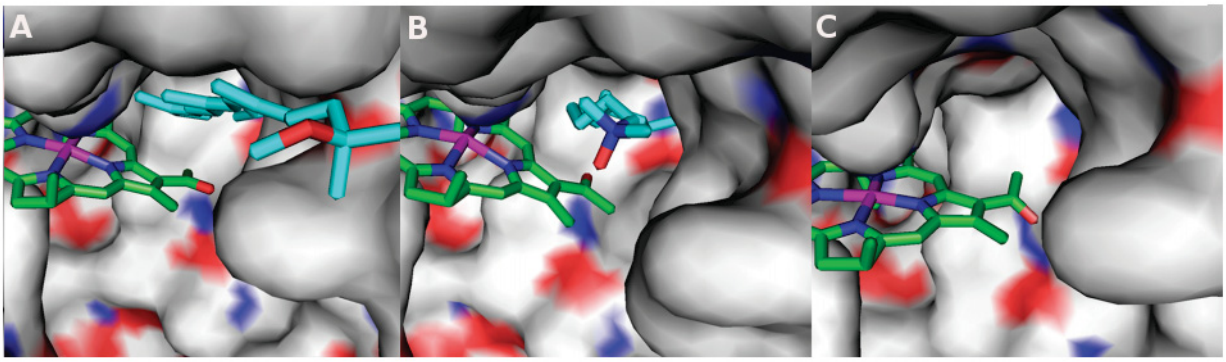

Figure 4.1: Orientation of 2-acetyl group of B_B determined by the occupation of Site 1. The B_B molecule is pictured near Site 1 and colored by atoms: carbon (green), nitrogen (blue), oxygen (red), and Mg^{2+} (magenta). The molecule occupying Site 1 is colored similarly to B_B but with cyan instead of green for carbon atoms. The protein is represented as a white surface with negatively charged regions colored red, and positively charged ones colored blue. Site 1 is shown occupied by a spheroidene (A), an LDAO molecule (B), and nothing (C). Coordinates taken from PDB entry codes: (A) 1PCR, (B) 1RG5, and (C) 1OGV. Figure reproduced with permission from Deshmukh et al.[51]

4.1.2 Site 2

The binding of manganese to Site 2 was confirmed by the prevented binding of the cyt c secondary electron donor protein, with a binding site overlapping that of Site 2, to the BRC. This lack of cyt c binding was observed by measuring similar thicknesses of protein monolayers composed of cyt c alone (2.2 nm), and cyt c with BRC pre-exposed to Mn^{2+} (2.5 nm), and comparing this to the measured thickness of cyt c with BRC in the absence of manganese (5.7 nm) (see Figure 3.3). The thickness of the cyt c only layer matches closely to the protein's thickness obtained from crystal structures (2.3 - 3.0 nm, depending on orientation[70]). This suggests a high surface coverage of monolayer cyt c on the chip was accomplished, as would be expected from a surface-charged, water-soluble protein. The thickness of the cyt c + BRC layer, however, was much lower than the ~9.6 nm thickness of crystal structures.[71] This is likely due to two reasons. The main one being the large area occupied by the detergent belt of the BRC. Neutron diffraction experiments have shown that detergent belts and detergent intermicellar bridges occupy ~45 % of the total volume in protein crystals[72,73] (see Figure 4.2). As these detergent structures are thin but wide, they would occupy a large area on the chip, but contribute only about $1/3$ of the protein thickness. This would cause an effective surface coverage of ~70 % compared to the observed 59 %. Of course the detergent-protein monolayer on our chip is likely different from the three-dimensional protein crystals, however large detergent belts, and possibly connecting structures, will still be present in our case, and likely have similar effects. The other reason for low measured thickness comes from the slight excess of cyt c needed in mixing with BRC to assure complete binding of BRCs. This leads to

some unbound cyt c which can bind to the chip, and contribute, again, a thickness of about 1/3 of the cyt c-BRC thickness. Thus while not a perfect bi-protein monolayer, the measured thickness of the layer with cyt c and BRC reflects proper cyt c-BRC binding. The final layer, containing cyt c, BRC, and Mn was much thinner, closer in thickness to the layer of cyt c only than to that of cyt c and BRC. The 3 Å difference between this layer and that containing cyt c only could be attributed to a contribution to the measured thickness from a small fraction of BRCs which do not have manganese bound to Site 2. The binding curve of Figure 3.9 shows that ~10 % of BRCs did not have Mn bound to Site 1 of the BRC. A similar non-saturating binding of Mn to Site 2 would be in agreement with the fraction of BRCs with bound cyt c required (8 %) to cause this difference in thickness.

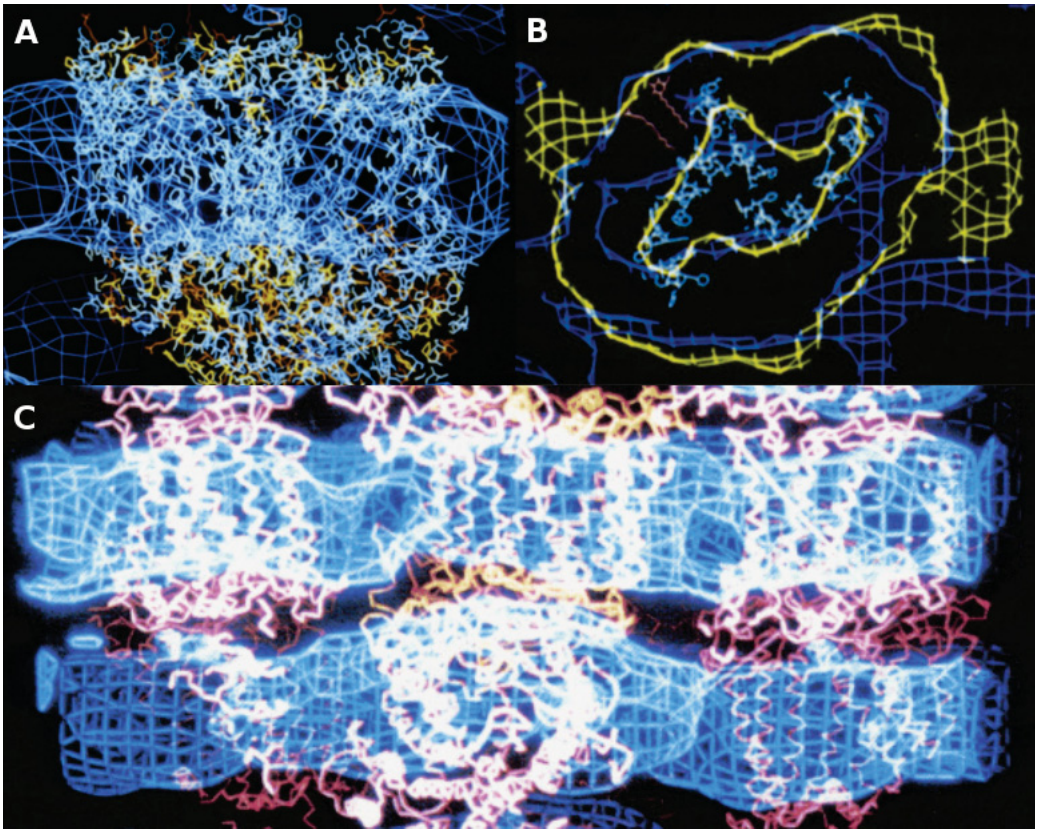

Figure 4.2: Neutron diffraction images of detergent micelle belt surrounding the BRC. A, B: side and top view, respectively, of a single BRC and its detergent belt. C: multiple layers of the BRC crystal which share micellar structures. Note the amount of surface coverage taken by the detergent relative to the protein. Images reproduced with permission from Roth et al.[72]

4.2 Establishing Site 1 as the location of the manganese electron donor

A Mn^{2+} ion bound to Site 1 was identified as the secondary electron donor of the BRC, with several forms of evidence. The accessibility of this site to Mn^{2+} was found to be a limiting factor of ET, as would be expected from the hydrophobic environment of Site 1, and ET was further impaired upon reducing the accessibility of this site by incorporating the BRC into liposomes. Evidence of a bound, oxidized manganese was also found to be present near Site 1. Furthermore, both the kinetics of ET from Mn^{2+} to BRC, and the presence of this oxidized manganese were found to be sensitive to both the presence of molecules with known binding and/or activity near Site 1, and conformational changes known to take place at this site. On the other hand, no ET between Mn^{2+} at Site 2 and the BRC was observed.

4.2.1 Mn^{2+} binding modulated by Site 1 accessibility

The limitation of the ET from Mn^{2+} to P^+ by the accessibility of the Mn^{2+} binding site was demonstrated in several ways. One way this was shown was from the dependence of the rate constant of ET on the time Mn^{2+} was allowed to incubate with the BRC (see Figure 3.4). As the hydrophobic environment of Site 1 would be far less accessible to a Mn ion than the polar environment of Site 2, this suggested the ET originated from a Mn^{2+} bound to Site 1. What's more, conformational changes, induced by pre-illuminating the BRC, were found to partially alleviate this accessibility limitation. These light-induced conformational changes have been shown to produce an increase of the local dielectric constant in the vicinity of B_B,[47] near Site 1. This increase would in turn improve the accessibility of this site to a Mn ion by reducing the energetically unfavorable configuration of charges in a low dielectric medium.

We observed further evidence of ET being limited by binding site accessibility to Mn when the BRCs were incorporated into various liposomes (see Figure 3.13 B). The increased barrier to Site 1 provided by the tighter-packed liposomes covering the BRC's hydrophobic midsection caused huge changes in the kinetics of ET from Mn^{2+} to BRC. The extent of these changes depended on the packing density of lipids in the liposomes, with the most tightly packed liposomes, those made from neutral headgroup lipids, having the greatest effect, and the less tightly packed liposomes, made of charged headgroup lipids, having a much lesser effect (see Figure 1.5 of the Introduction). As BRCs would be embedded in a lipid bilayer *in vivo*, it is possible that the effectiveness of Mn^{2+} as a secondary electron donor to the BRC could be reduced in live cells. The natural membrane, however is inhomogeneous, and may not provide as much of a barrier as observed with the homogeneous liposomes of Figure 3.13. Future work, testing Mn^{2+} ET to the BRC in chromatophores or live cells, should therefore be conducted.

4.2.2 Presence of a bound oxidized manganese ion

4.2.2.1 Evidence of the oxidized manganese ion at Site 1

Evidence of a bound oxidized manganese (Mn^{3+}) near Site 1 gives strong support for this being the site of the redox-active manganese. This evidence was observed as a shift of the P band in the light - dark difference spectrum of the BRC in the presence of Mn (Figure 3.6, 3rd trace from the top). As can be seen in Figure 4.3, the double difference spectra between the light - dark spectra of pre-illuminated and dark-adapted R-26 leaves us with only a shift of the P band. This shift was fit to that of a Gaussian from 865.0 nm to 862.7 nm. It was up to five times as large as that in the absence of Mn (see Figure 3.8), and as light-induced conformational changes have been shown to be blocked by the presence of Mn^{2+},[22] only changes due to the oxidized electron donor and the reduced quinone should be visible in these difference spectra. This shift is therefore, likely due to the electrostatic effects of an oxidized Mn electron donor. The location of this bound, oxidized manganese was determined from its sensitivity to the same light-induced conformational changes of the previous section (see dark-adapted trace, 2nd from top), and also to the presence of several molecules (see bottom 3 traces), including the carotenoid of WT BRCs (see brown traces). The light-induced conformational changes are a requirement for the large shift of the P band. As they were shown to facilitate manganese binding to Site 1 in the previous section, the necessity of these conformational changes is consistent with the assignment of this shift to the presence of a bound oxidized Mn. The large shift of the P band would also either weaken or disappear with the presence of the other molecules, which were shown to have access to the immediate vicinity of Site 1 in Figure 3.5. This suggests the presence of these molecules likely interferes with the tight binding of Mn to Site 1, which is further demonstrated from their retarding effect on the kinetics of ET from Mn^{2+} to P^{+}, as can be seen in Figures 3.13 and 3.14. Their effects on kinetics will be discussed more deeply in Section 4.2.3.

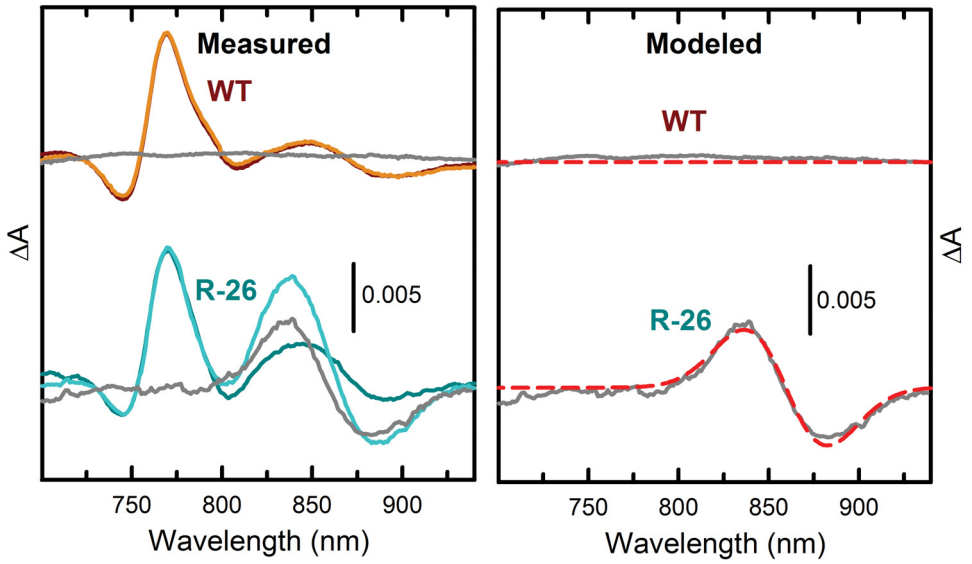

Figure 4.3: Double difference spectra of the light - dark spectra for pre-illuminated and dark-adapted BRCs. Brighter colored traces are of pre-illuminated BRCs and darker ones are dark-adapted. The R-26 trace features a blue shift of the P band which was fit to a Gaussian shift from 865.0 nm to 862.7 nm. Conditions as for Figure 3.6.

As we hypothesize that the shift of the P band is caused by a bound oxidized Mn, it should be caused by the transient electric field created by the extra charge on the oxidized manganese that remains bound, affecting the Q_y transition dipole of P. We should therefore be able to calculate the energy of this charge-dipole interaction, and see if it matches that of the elevated energy level associated to the observed blue shift of the P band. The energy of charge-dipole interactions can be described by Coulomb's law as:

$$U = \frac{\Delta z_{Mn} \vec{r} \cdot \vec{\mu}}{4\pi\epsilon r^3} \tag{4.2.1}$$

Where Δz_{Mn} is the change in the number of charges on Mn, which will be 1 when examining light - dark spectra, as effects due to charges on Mn before illumination have been subtracted out. μ is the strength of the dipole moment of P. μ of P has been found via Stark spectroscopy to be ~4.1 D.[74] To find the direction of the dipole moment, we followed Zinth et al.[75] in taking the vector sum of the the dipole of each BChl molecule of P. This was done by making Eq. 4.2.1 into a sum of interactions from two dipoles, with one being assigned to the direction of the BChl residing on the L half of P and having half of the total μ, and the other assigned to the M half. Eq. 4.2.1 can then be rewritten as:

$$U = \sum_i \frac{\Delta z_{Mn} \vec{r_i} \cdot \frac{1}{2}\vec{\mu_i}}{4\pi\epsilon r_i^3} = \sum_i \frac{\Delta z_{Mn} \frac{1}{2}\mu cos\theta_i}{4\pi\epsilon r_i^2} \tag{4.2.2}$$

We determined θ and r with the atomic coordinates of BRC structures taken from the PDB, yielding values of 1.59 nm and 2.28 nm for r_1 and r_2, respectively, and ~30° for both θs. ϵ has also been determined for the vicinity of H and B with Stark spectroscopy, having an average value of 3.8 for the inactive cofactors at room temperature.[76] These values yield an interaction energy of 7.1 meV, compared to the 3.8 meV corresponding to the change in energy associated to the shift in the P band, which is calculated simply from:

$$U = \frac{hc}{e}\left(\frac{1}{\lambda_2} - \frac{1}{\lambda_1}\right) \tag{4.2.3}$$

where h is Planck's constant, c is the speed of light in vacuum, e is the fundamental charge (used to obtain units of eV), and λ is the wavelength of the P band. A diagram of this interaction can be seen in Figure 4.4.

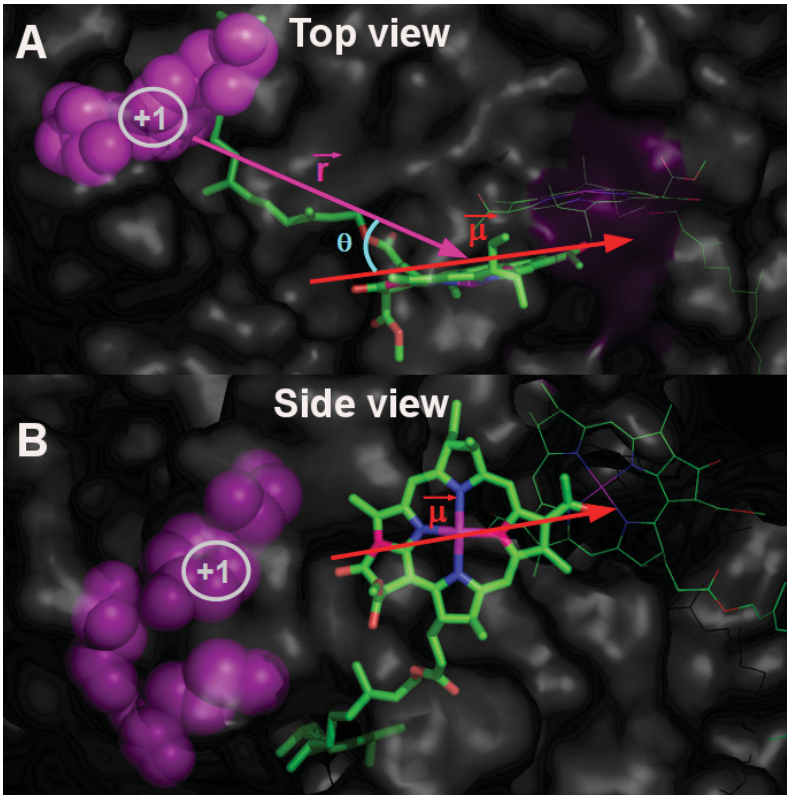

Figure 4.4: Diagram of charge-dipole interaction between additional charge on oxidized manganese and Q_y dipole of P. A: top view, and B: side view, showing vectors (colored arrows) of dipole moment $\vec{\mu}$ and charge distance $\vec{r}$. Atoms of the Mn binding site are shown as pink spheres, with the extra charge due to the oxidized Mn being depicted as a grey, circled +1. P is shown represented with sticks, colored by atom (carbon, oxygen, nitrogen and magnesium, colored green, red, blue and purple, respectively). The surrounding protein is shown as a semi-transparent surface. The top view is in plane with μ and roughly in plane with r, thus both vectors can be depicted, along with the angle between them θ. Interaction from only one BChl dipole of P is shown for clarity, however the other BChl molecule is shown, as fainter sticks, in relation to the the charge. Atomic coordinates taken from PDB code 1PCR.

While there is a disagreement between these energies, several uncertainties in the parameters used could all decrease the energy of Eq. 4.2.2. For example, depending on where exactly Mn binds to Site 1, could affect U through r by up to ~0.5 meV. More importantly, the value of ϵ could change U drastically, as there is still much debate over the dielectric strength inside the BRC. Many studies have reported much larger values of 10-20.[77–80] However, none of these other studies, directly measured ϵ near Site 1. Instead they either use computational methods to calculate the average ϵ of the BRC, or they measure ϵ, but closer to the periplasmic surface. Both methods would result in an overestimation of ϵ for our region of interest, as ϵ of Site 1, which is buried inside the membrane region of the BRC, will surely be lower than both the ϵ near the periplasmic surface, and the average ϵ of the BRC. Additionally, the conformational changes which we have induced here by pre-illuminating our samples have been shown to increase ϵ in the vicinity of P and B.[47] Therefore, our charge-dipole interaction energy is likely smaller than the 7.1 meV calculated above. Unfortunately the extent of the increase in ϵ due to these conformational changes is unknown. As the extreme, we could set the upper limit on the dielectric constant after conformational changes as 20, that measured at the hydrophillic perimeter of the BRC.[77,78] This would result in a 5 fold decrease in energy from the charge-dipole interaction, making the disagreement between this interaction energy and that of the blue shifted P band in the opposite direction.

A similar large blue shift of the P band, which is dependent on both pre-illumination and the secondary electron donor used, has been previously observed in BRCs from *Rhodobacter capsulatus*.[42] Here the large shift was observed in the light - dark difference spectrum, in addition to the typical spectrum of the PQ^- state, when 2,3,5,6-tetramethyl-p-phenylenediamine (DAD) was used as a secondary electron donor, and only when the BRC was kept out of its light-induced conformational changes state. The similar spectral products of photo-oxidation, with similar prerequisites, highlights the importance of light-induced conformational changes, and the molecular occupation of the vicinity of Site 1 to interactions between the secondary electron donor and the rest of the cofactors in the BRC.

4.2.2.2 Further resolving the binding of the oxidized manganese

We initially thought that as the source of the large shift of the P band on the light - dark difference spectrum was different from that of the rest of the spectrum, typical of the PQ^- state, it would recover with a different lifetime. However, this was not found to be the case, as all spectral features of the light - dark spectrum recovered with an indistinguishable lifetime (see Figure 3.7). This does not necessarily exclude the possibility of these spectral features being due to different sources. From the specific conditions required to observe the shift of the oxidized Mn, we can deduce that its binding must be fairly weak. It could, therefore, be possible that the binding of Mn^{3+} is affected by the negative charge residing on the quinone. In this case the electrostatic attraction of Q^- could be holding Mn^{3+} in line with the Q_y dipole

of P, and as the quinone recovers to its neutral state Mn^{3+} would shift its position, increasing r and/or θ to the point where it no longer has a significant electrostatic interaction with the dipole.

Manganese binding to the BRC had a particularly interesting dependence on LDAO concentration. As can be seen from the bottom trace of Figure 3.6, LDAO is required for the presence of the P band shift assigned to a bound Mn^{3+}. However we can see in Figure 3.11 B, that the kinetics of ET from Mn^{2+} to P^+ can be drastically hindered at high concentrations of LDAO. This dependence was explored in Figure 3.8 to determine whether the requirement was of a LDAO membrane substituent, or an integral LDAO molecule bound to the BRC. The makeup of the membrane constituent has been shown to have a significant effect on the transfer of electrons and protons for BRCs suspended in detergent micelles.[81–83] However, as the CMC occurs at a much lower LDAO concentration than that of the large dimer shift, we can conclude that it is not the makeup of the micelles themselves which are important in our case, but an LDAO molecule bound inside the protein which facilitates the binding of Mn^{3+}. Such integral LDAO molecules have been observed in many locations in and around the BRC in crystal structures.[48–50] In fact LDAO molecules have been observed right at Site 1 in R-26 BRCs,[49,50] as can be seen in Figures 3.5 and 4.1. LDAO molecules at Site 1 are not, however, observed in WT BRCs, as the carotenoid occupies this space. This could explain why bound Mn^{3+} wasn't observed in WT samples in Figure 3.6, as here the LDAO concentration was much below the K_D for WT. It could also explain the large drop in rate constant of ET from Mn^{2+} to P^+ in R-26 at high LDAO concentration, observed in Figure 3.11 B and Figure 3.14 B and C. As R-26 displays a high affinity of LDAO binding near Site 1, very high concentrations of LDAO could lead to multiple molecules binding in this location, and eventually creating the same steric interference for Mn^{2+} binding as the carotenoid molecule of WT; yielding similar rate constants for the two strains.

4.2.3 Kinetics of electron transfer from manganese modulated by molecules preferentially bound to or near Site 1

The molecules used to probe Site 1 for bound oxidized manganese were also found to have an effect on the kinetics of ET from Mn^{2+} to P^+ (see Figure 3.14), as would be expected. These molecules are likely impacting ET from Mn^{2+} to P^+ by weakening the binding of Mn^{2+} to Site 1 through steric hindrance. This could be due to either specific binding of these molecules to nearby or overlapping sites, or from a crowding of molecules near Site 1. Both the quinones and terbutryne have known nearby binding sites. It is possible that the tails of UQ_{10} and terbutryne could interfere with manganese binding, however UQ_0, with its lack of isoprene tail, could not interfere from this site The inhibitory effect of UQ_0 was found to follow a binding curve, though, which leads us to conclude that its effects must be due to specific binding. It must therefore have a binding site elsewhere in this cavity, closer to Site 1. As

previously mentioned, crystal structures show LDAO bound to Site 1. One would thus expect specific binding, however, a binding curve was not observed during this titration. This can be attributed to the more complex interaction between LDAO and Mn at Site 1, as discussed in the previous section. The contributions of the different effects that LDAO has on this binding could mask any coherent binding behavior of the titration. The very limited effect of NaCl on the kinetics can be attributed to its low affinity to the low dielectric environment of the BRC's membrane region, where Site 1 is located. The mild effect at high concentrations that is observed is likely due to a low local concentration of these ions creating a weak screening of the electrostatic interactions required for binding and electronic coupling of Mn to the BRC.

The slowing effects on the kinetics from these molecules also provides further evidence that this ET originates from the Mn^{2+} bound to Site 1. While the local concentrations of these molecules relative to Mn^{2+} may be relatively high inside the detergent belt of the BRC, due to their hydrophobic nature (aside from NaCl, as discussed above) and the hydrophilic nature of Mn^{2+}, their concentrations in solution would be insignificant relative to Mn^{2+} (30 mM). Therefore, steric hindrance of Mn^{2+} binding at Site 2 would be improbable at the concentrations added for all of these molecules, except possibly LDAO, which was added at much higher concentrations.

4.2.4 Redox activity of manganese at Site 2

While evidence for the presence of a bound manganese at Site 2 was found, we were unable to find any evidence of redox activity between this manganese and the BRC. When both cyt c^{2+} and Mn^{2+} are present, Mn^{2+} is clearly successful at competing for binding to Site 2, as seen in Figure 3.3. However, only ET from cyt c^{2+}, which must be a collisional process as its binding is blocked, is observed in this situation. We have not completely excluded the possibility of manganese electron transfer from this site though, as it is possible that Mn^{2+} and cyt c^{2+} are both able to donate an electron from this site. If this were the case we would only observe ET from cyt c^{2+}, as cyt c^{2+} is significantly more rapid than Mn^{2+}. However, we can conclude that regardless of whether Mn^{2+} bound to Site 2 takes part in reducing P^{+}, the dominant manganese secondary electron donor to the BRC must be that which is bound to Site 1. Otherwise the various Site 1 probes we have used to modulate this ET (see Figures 3.4, 3.13, 3.14) would only affect a fraction of the BRCs, leading to biphasic kinetics with one component completely independent of the presence of the probe, which is not observed.

4.3 Influence of manganese on the kinetics of various electron transfer steps

4.3.1 Charge recombination

While elevated rate constants of P^+ recovery following flash excitation were observed in Figure 3.9, this is was found to not be ET from Mn^{2+}. Instead, the elevated observed rate constants can be attributed to the increase in driving force of P^+Q^- charge recombination due to the 55 mV elevated P/P^+ potential caused by the presence of manganese, which was observed previously.[24] We can verify this with a calculation using Dutton's Ruler, a relationship developed by Dutton et al.[84] using the theoretical parameters of ET from Marcus theory, and the empirical packing density of ET proteins. The Dutton's ruler equation takes the following form:

$$log\, k_{ET} = 15 - 0.6r - 3.1\left(\Delta G + \lambda\right)^2/\lambda \tag{4.3.1}$$

where k_{ET} is the rate constant of ET, r is the edge-to-edge distance between the donor and acceptor, ΔG is the Gibbs free energy difference between donor and acceptor states, and λ is the reorganizational energy, a measure of the energy required to adjust surrounding "solvent" molecules to accommodate the change in charge of donor and acceptor. The edge-to-edge distance between Q_A and P is 23 Å.[49] The ΔG can be found from the redox potentials of -50 mV for Q/Q^-,[85] and 500 mV and 555 mV for P/P^+ in the absence and presence of of Mn, respectively,[24] yielding ΔGs of 550 mV and 605 mV. This yields a rate constant of $P^+Q_A^-$ charge recombination that is accelerated from 8.0 s^{-1} to 10.2 s^{-1}, in rough agreement with the accelerated values of 9.5 s^{-1} and 10.7 s^{-1}, observed for R-26 and WT, respectively. While this calculation assumes a constant reorganizational energy, which is unlikely with a nearby bound Mn ion, it shows us that the acceleration of the rate constant upon Mn binding could very well be caused by the elevated P/P^+ potential.

Additional proof of the observed 2 s^{-1} rate constant not being ET from Mn was found by showing that flash excitation does not produce ET from Mn^{2+} to the BRC. This was demonstrated by the lack of PQ^- state formation following a flash, in three different ways in Figure 3.10. It is shown by the lack of the PQ^-/PQ spectrum immediately after flash excitation (panel A), by the similar recovery of spectral features typical of the P^+Q^- state and PQ^- state (panel B), and by the lack of a trapping in the PQ^- state over several flashes (panel C). The lack of ET from Mn^{2+} during flash excitation is due to this process having a much slower rate constant, found to be ~1 s^{-1} in Figure 3.11, than that of charge recombination from the $P^+Q_A^-$ state, found to be ~10 s^{-1} in Figure 3.9. Therefore, the previously reported rate constant of ET from Mn^{2+} to P^+ of ~12 s^{-1},[24] during flash excitation, must in fact be charge recombination from the $P^+Q_A^-$ state.

One would still expect ET from Mn^{2+} to be observable in samples with reconstituted secondary quinone, as its rate constant is similar to that of charge recombination from the $P^+Q_B^-$ state (2 s^{-1}) which is observable in Figure 3.9. However, this is clearly not the case as panel C of Figure 3.9 shows that this slower component suffers a large drop in amplitude upon binding of Mn^{2+}. The binding of Mn^{2+} must therefore disrupt the redox activity of the secondary quinone. This will be discussed further in Section 4.4.1.1.

4.3.2 Electron donation from manganese

As ET from Mn^{2+} was found to be slower than charge recombination, we had to remove the influence of charge recombination on the kinetics of P^+ recovery to properly determine the rate constant of ET from Mn^{2+} to P^+. This was done using high-intensity continuous illumination, as seen in Figure 3.11. As explained in Section 3.3.2, the requirement for an insignificant impact of charge recombination on the kinetics is for the rate of charge separation (the photochemical rate) to be much greater than that of charge recombination, or Eq. 3.3.3 is close to zero. We can quantify the extent with which we meet this condition by using an empirical relationship from the literature between illumination light intensity and the photochemical rate constant, which was derived under similar conditions to ours. An illumination light intensity of 1 W/cm^2, close to the intensity of 1.1 W/cm^2 we used to determine rate constants of ET, was found to give a photochemical rate constant of approximately 520 s^{-1}.[86] Putting this in Eq. 3.3.3, along with the fastest rate of charge recombination, ~10 s^{-1} leaves us with ~2 % of BRCs which will not be in the charge separated state, and can therefore influence the measured rate constant. While this is a very rough calculation, it assures us that our approximation of Eq. 3.3.3 being equal to zero is valid within our experimental error.

Another possible issue with our high-intensity illumination method that is worth examining in more detail is the potential to introduce unwanted effects and alternate ET pathways by over-exciting BRCs with very high illumination intensity. High-intensity illumination has been found to induce ET along the inactive cofactor branch, due to multiple, simultaneous photoexcitations of the cofactors.[87] However, the very high-intensity, short-temporal-width pulses of excitation light used were capable of delivering 5 orders of magnitude more photons to the BRC, before any ET could take place, than possible from the continuous illumination of our setup. Another side effect of high intensity illumination has been observed with less extreme intensities. In this case BRCs with an impaired Q_B ET rate could cause the trapping of an electron on Q_B, eventually leading to an accumulated $PQ_A^-Q_B^-$ state and even a $PH_A^-Q_A^-Q_B^-$ state, which accelerated ET in the BRC.[62] This is a more realistic worry for us, as in our case the presence of manganese impairs Q_B ET. Fortunately, this reported situation was possible because of the use of a rapid secondary electron donor, cyt c, along with a large quinone pool, allowing many turnovers to take place. In our case no quinone pool was present while determining the rates of ET from Mn^{2+} to P^+, and Mn^{2+} is much slower than the rates

of charge recombination of these intermediate states (the lifetime of the $P^+Q_A^-$ state is ~100 ms, and that of $P^+H_A^-$ is ~20 ns), making their buildup an impossibility.

As we carried out this experiment under continuous illumination, we have yet another potential pitfall to address. This is that light-induced conformational changes which occur in the BRC have been shown to alter the lifetime of the charge separated state.[42,47,51,88–91] Upon prolonged exposure to continuous illumination, lifetimes changed by up to a factor of ~60 in conditions similar to ours.[47] Fortunately, these lifetimes were increased, which would only further limit the impact of charge recombination on kinetics. Furthermore, the addition of manganese was shown to block these changes.[22] We can therefore safely ignore any effects light-induced conformational changes have on the kinetics of P^+ recovery under high-intensity continuous illumination.

With these potential issues addressed, we can be confident in our assignment of the rate constants of P^+ recovery to ET from Mn^{2+} to P^+ under high-intensity continuous illumination.

4.4 Biological feasibility and evolutionary implications of the Mn-BRC system

A large part of the interest of studying the incorporation of manganese as a secondary electron donor by the BRC comes from its potential as an evolutionary link between anoxygenic and oxygenic photosynthesis. It is therefore important to ensure the function of the BRC is maintained after incorporation of the new secondary electron donor, and to examine the potential impact on the fitness of an organism using this system.

4.4.1 Manganese as a secondary electron donor preserves function of BRC

We have seen that the presence of manganese has a strong impact on the function of the quinone cycle and on the ET from the cytochrome secondary electron donor. Both of these are critical functions of the BRC, and thus, the survival of the organism. Below we examine the specifics of these impacts, and ensure the biological feasibility of manganese incorporation by the BRC.

4.4.1.1 Evidence of a functional quinone cycle

The quinone cycle allows the continuous cycling of electrons, and the transfer of protons across the membrane, creating the proton gradient that will provide energy for the organism. It is therefore a critical function of the BRC, and must be preserved for the biological feasibility of a manganese-utilizing organism. This process takes place inside living cells, but can also

take place in isolated BRCs when a continuous supply of excitation illumination and redox molecules are provided. We can therefore examine the effects of manganese on the quinone cycle, and determine whether this critical function is preserved.

In Figure 3.14 there is a large difference in the concentration dependence of the two different quinones. BRCs with UQ_0 exhibit a rate constant nearly independent of UQ_0 concentration, with the amplitude of recovered P^+ gradually dropping with increased concentration. This is what would be expected of an inhibitor. On the other hand, the addition of UQ_{10} completely changes the kinetics, with both the amplitude and rate changing abruptly with increased concentration. This is as would be expected from QH_2 formation. As UQ_{10} can be incorporated by the BRC as Q_B, adding excess UQ_{10} effectively increases the quinone pool available for the quinone cycle and the production of QH_2 (see Figure 3.12). Since the rate of ET from Mn^{2+} to P^+ is relatively slow, QH_2 formation and replacement with new oxidized Q from the quinone pool happens with a greater rate than P^+ reduction by Mn. We therefore, don't see a large drop in P^+ amplitude until the quinone pool is exhausted. Furthermore, the steeper slope of the binding fit for UQ_{10} suggests a multiplicative effect where the addition of one UQ_{10} molecule causes the inhibition of two BRCs. This can be explained by the two P^+ reduction events needed to remove each UQ_{10} molecule from the BRC, through conversion to QH_2. UQ_0, on the other hand, has a more gradual slope, and therefore only a single molecule participating in the binding. This suggests simple inhibitive binding, as discussed in Section 4.2.3. From these results we can conclude that the full quinone cycle is intact in BRCs containing UQ_{10}, but not UQ_0.

As mentioned in Section 4.3.1, however, a large drop in the fraction of BRCs exhibiting charge recombination from the $P^+Q_B^-$ state after flash excitation is observed upon the addition of Mn^{2+} (see Figure 3.9). This suggests a disruption of ET to Q_B upon binding of Mn^{2+}. It is interesting to note that the behavior of this disruption of Q_B by manganese followed a binding curve involving 2 ligands. This would suggest that the inhibition of Q_B ET involves the binding of two Mn ions to the BRC. One would think these ions must be in the vicinity of Q_B in order to affect it, with one Mn ion likely the same which binds to Site 1, and the second ion likely close by in the same cavity. An alternative possibility to this disruption mechanism will be offered below, in Figure 4.7.

Another observation we can make from Figure 3.9 is the lower K_D in WT BRCs. While this may seem in contradiction to our other results, which clearly show a higher affinity binding of Mn to R-26 BRCs, this is actually not the case here, as we are monitoring the disruption of ET from Q_A to Q_B. In WT BRCs the presence of the carotenoid must displace Mn from its optimal binding position at Site 1, as seen from the greater binding affinity and rate constant of ET of R-26 compared to WT. As ET from Mn is still observed, Mn must bind elsewhere in this cavity, and as can be seen from images of the cavity (see, for example, Figure 3.1.1) this will certainly be closer to Q_B, and likely further from P, explaining WT's higher binding affinity for Q_B disruption, but lower binding for ET to P^+.

Despite the disruption of ET to Q_B by Mn, we now know that the quinone cycle is functional in these BRCs, necessitating ET to Q_B. We must, therefore, conclude that the binding of Mn^{2+} to the BRC does not completely displace or deactivate Q_B, but hinders ET to it. The quinone cycle taking place in these observed kinetics can therefore be appended from Figure 3.12 to that of Figure 4.5 below. The Q cycle continues as normal, observed as the slow linear recovery of P^+ early in the kinetics of Figures 3.13 A and 3.14 D. As the Q pools of more and more BRCs are used up they go through one last turnover and are then trapped in the PQ^- state (the red part of Figure 4.5). This is seen as an acceleration of the P^+ recovery kinetics.

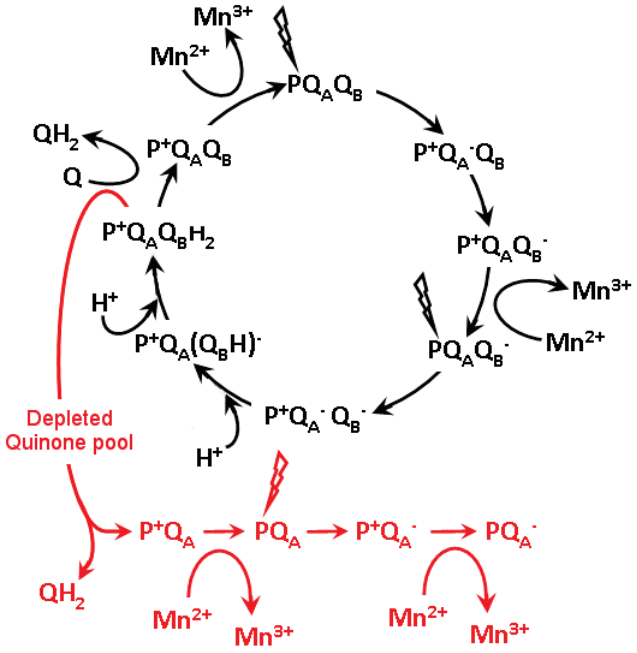

Figure 4.5: Quinone cycle, and cycle termination active in the Mn-BRC kinetics observed under continuous illumination and in the presence of excess Q_B. The cycle continues as normal (black) until the quinone pool is completely depleted. Upon depletion of the oxidized quinone pool (red), manganese presence will inhibit electron transfer to Q_B, and Mn reduction of P^+ will lead to a final trapping in the PQ_A^- state. See Figure 3.12 for details on the pre-Q depletion cycle.

ET from Q_A to Q_B is conformationally gated,[92,93] with the gating mechanism proposed to be the conformational changes resulting in a change in Q_B binding, including a translation of 2.7 Å and a flip in binding orientation about its tail, from a distal to a proximal orientation[94,95] (see Figure 4.6). As the site of ET from Mn^{2+} to P^+ has been shown to be in the same cavity as Q_B, within ~13 Å of Site 1, it is not unlikely that the proximity of this ion could impede these changes from occurring. This is particularly plausible considering the amount of space needed to move and rotate the long 50 carbon chain of UQ_{10}. The sub-optimal position and orientation of Q_B with respect to Q_A could in turn significantly slow ET from Q_A to Q_B, as this change involves moving the conjugated head of the quinone (where the electron would reside)

~4 Å towards Q_A. Without these light-induced conformational changes ET from Q_A to Q_B has been observed to slow by several orders of magnitude,[96] in line with our observations.

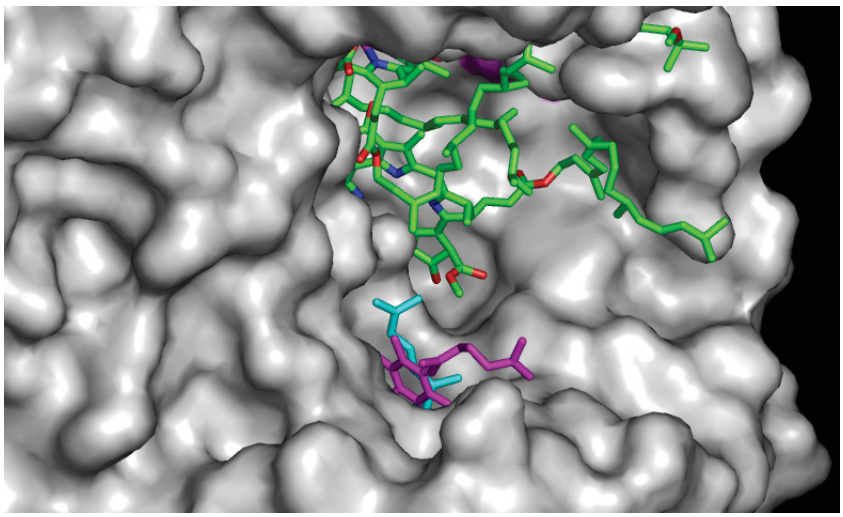

Figure 4.6: Different binding positions and orientations of the secondary quinone. Q_B is shown in its dark-adapted binding conformation (purple) and its shifted and rotated light-induced conformation (cyan). This shift is thought to be part of the conformational gating of ET from Q_A to Q_B. The full isoprene tails of the Q_Bs are not shown. The BRC is pictured as a white surface, with Site 1 colored magenta, and the cofactors are pictured as sticks colored by their atoms (carbon-green, oxygen-red, and nitrogen-blue). Coordinates from PDB code 2J8C.

An alternative explanation for the disruption of ET to Q_B could be offered by a previous observation of divalent metals binding to the BRC and blocking the proton uptake pathway to nearby amino acid residues of Q_B.[97–99] Along with the conformational changes mentioned above, proton uptake along this pathway facilitates ET from Q_A to Q_B,[100] and with a metal blocking it ET rates have been shown to drop by up to two orders of magnitude. This retarding effect on the ET to Q_B was found to be the strongest at pH's above 9,[99] where our measurements were conducted. The exact binding location of the divalent metals was found, via X-ray crystallography, to be on the cytoplasmic surface of the H subunit (see Figure 4.7). As our probing of binding sites did not include this location, it is possible that Mn^{2+} is bound here, and disrupting ET to Q_B in a similar way, by blocking proton uptake to the Q_B site.

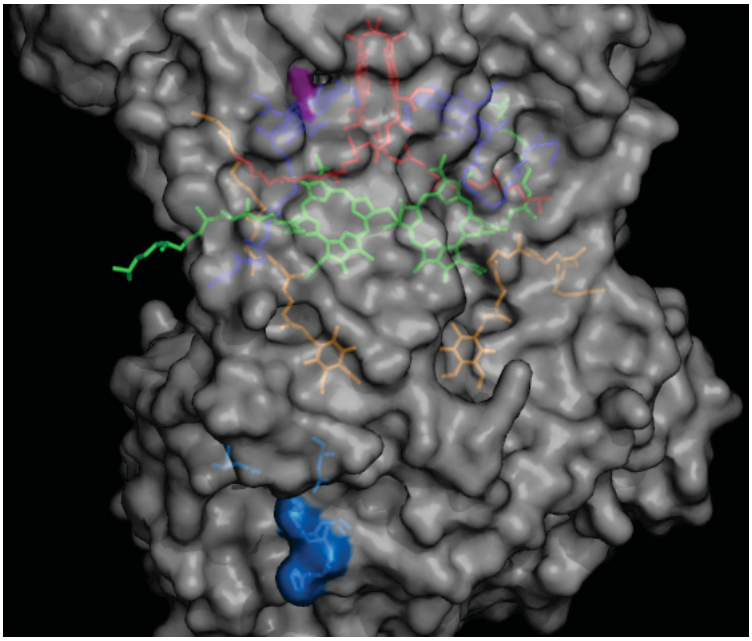

Figure 4.7: Metal binding site blocking a proton uptake pathway important for ET to Q_B. Amino acid residues comprising the opening of a proton transfer pathway leading from the cytoplasmic surface of the H subunit to the vicinity of Q_B are colored bright blue. Severe inhibition of ET from Q_A to Q_B has been observed when divalent transition metals were bound to this site. Mn could, therefore, be inhibiting ET to Q_B with this same mechanism. Representation and coloring similar to Figure 3.2. Atomic coordinates taken from PDB code 1RG5.

In summary, we have found that while ET to Q_B is hindered by the bound manganese, it is still functional under continuous illumination, allowing completion of the quinone cycle, a critical function for the organism. Thus the effects of manganese on the quinone cycle of the BRC do not exclude our system as a biologically feasible evolutionary candidate for the transition from anoxygenic to oxygenic photosynthesis.

4.4.1.2 Retardation of electron transfer from the native secondary electron donor

In Figure 3.15 the secondary electron donor of the BRC, cyt c, was found to have its rate constant slowed by nearly 3 orders of magnitude at the elevated pH of 9.4, where our Mn-BTP electron donor operates. This ET was found to slow by another order of magnitude in the presence of manganese, likely due to an interference of cyt c docking, as Mn was found to successfully compete for their shared binding site in Figure 3.3. From the combination of these effects, the rate constant of ET from cyt c^{2+} to P^+ was slowed to 160 ms, only five times faster than R-26 (opposed to a million times faster, in conditions optimal for cyt c). Manganese does not, however, completely disable cyt c as previously thought.[24] While Mn would still not be able to compete with cyt c as a secondary electron donor to the BRC with the conditions considered thus far, it is not entirely unlikely that the elevated pH and the presence of excess manganese ions could have a similar retarding effect on the re-reduction of

cyt c at the cytochrome bc_1 complex. In fact, divalent metal ions have been shown to inhibit the function of this complex at concentrations much less than what is present here.[101,102] Therefore, while cyt c remains the dominant secondary electron donor to isolated BRCs in detergent micelles, Mn could become dominant in a live cell environment, and is therefore still a possible evolutionary candidate for the transition to oxygenic photosynthesis.

4.4.2 An initial step in the development of oxygenic photosynthesis

Approximately 3 billion years ago, nature solved a difficult problem of physical chemistry that mankind struggles to solve to this day, the splitting of water into protons and oxygen, and free electrons via solar energy.[2,4] This came in the form of the evolution from the cyclical ET of anoxygenic photosynthesis, to the water-oxidizing ET of oxygenic photosynthesis. A likely starting point for this transition involves the incorporation of manganese ions as a secondary electron donor by the prehistoric, BRC-like RC.[6,7,103] However, the currently proposed mechanism of this incorporation involves either the incorporation of foreign proteins to procure manganese in a usable form,[67] or several mutations of the RC to give it the ability to utilize manganese in solution.[28] The former suffers from the lack of structural and genetic similarity between PSII and proposed manganese-carrying proteins, and a lack of evidence for the existence of such proteins in the Archean oceans.[67,104] The latter case, however, could include a system like the one presented here as an evolutionary stepping stone. In the current version of this mechanism multiple mutations are required in order to elevate the P/P^+ potential high enough for it to be able to oxidize Mn^{2+}, and more are needed to create a binding site for manganese near P.[28] Without containing simultaneously all of these mutations, no fitness would be gained by an organism, as it would still be unable to utilize Mn ions, making this an unlikely evolutionary pathway. A more plausible explanation for this transition would be the adoption of a manganese complex as a secondary electron donor by the native RC, in environments where the ET cycle of the native secondary electron donor is inhibited. The organism could then evolve to optimize this new electron source for more rapid ET, and for a higher usable energy yield from each electron received, eventually leading to the system of the PS II using the OEC to catalyze the harvesting of high energy electrons from water.

Overwhelming evidence for the ability of both R-26 and native WT BRCs to utilize manganese ions coordinated by BTP has been provided both here and previously.[24] We have used BTP, a synthesized molecule unlikely to be present in high concentrations in nature, to coordinate manganese into a complex with a redox potential accessible to the primary electron donor of the BRC. However, there is no reason to suspect that a more naturally available molecule with similar functional groups, such as the amino acids containing both amine and hydroxyl groups (tyrosine, methionine, and serine) could not coordinate manganese into a similar complex, as discussed previously.[24] The ability of cyt c to function as a secondary electron donor has been shown to be severely limited in the environment of elevated pH and high manganese

concentration, where manganese functions as a secondary electron donor, as discussed above. Manganese is thought to have existed in abundance both in the sediment of the ocean floors, as precipitates, and in surface waters of the Archean ocean,[104–107] with evidence of millimolar concentrations of manganese in some environments.[105] While Archean oceans are thought to have been slightly acidic from volcanic activity,[104] these oceans were by no means a homogeneous environment, and many niche environments with elevated pH likely existed. For example, in soda lakes, which are thought to be model water bodies for the Archean ocean, it has been found that surface waters containing high calcium concentrations raise the local pH to ~9.7 when they reach the high alkalinity of the deeper waters.[108] In addition to the slowed ET from cyt c, ET from Mn^{2+} to P^+ has been found to be slower than charge recombination from the $P^+Q_A^-$ state, and similar to charge recombination from the $P^+Q_B^-$ state, it is known that the native membrane environment helps stabilize charge recombination, with $P^+Q_B^-$ charge recovery retarded from 1 s to 10 s.[109] Stabilization would provide a better chance for ET from Mn^{2+} to P^+ to occur, increasing the productive yield of the Mn-BRC system.

From the above considerations, the currently proposed Mn-BRC system meets, or has the potential to meet, the requirements for a transitionary step along an alternative evolutionary pathway from anoxygenic to oxygenic photosynthesis.

4.5 Composition of the manganese complex

4.5.1 Stability of the complex

The Mn-BTP complex was found to be stable over the large range of concentrations probed in Figure 3.16. The high Rayleigh scattering of manganese and the high absorbance of buffer in the UV lead to quite large uncertainties at very high and very low concentrations, as can be seen from the large error bars. This is due to the large span in concentration requiring a variety of vessels, stocks, and volumes, creating high relative volume uncertainties at the extreme concentrations. While it was impossible to go beyond a concentration of 10 mM, as the absorbance-concentration relationship significantly deviates from the linear regime at these high concentrations, rapid P^+ recovery kinetics and near-saturating binding is already observed at this concentration (see Figure 3.9), providing evidence of a fully assembled Mn-BTP complex.

4.5.2 Homogeneity of the complex

It had previously been proposed that the Mn-BTP complex was likely heterogeneous in manganese, made up of a trimer of dimers.[24] If this were the case, however, we should be able to resolve these different species of manganese from the different energy levels of their electronic spin states. This was not seen in the EPR spectrum of Figure 3.17, as both the number

of lines, and their widths were identical to the spectrum of the manganese hexa-aqua complex, which is mono-nuclear in manganese. Similar conclusions were drawn from the redox properties of this complex, seen in Figure 3.18. Here fits to a Nernst equation for two of the three spectral signatures monitored yielded midpoint potentials within 2 mV of each other. While there is an 18 mV difference of the midpoint potential attained from the 265 nm peak, this peak has a more complex composition, being made up of one peak and one shift. This measurement is therefore likely the least reliable.

From these results, we suggest that the secondary electron donor to the BRC is a BTP-coordinated complex which is mono-nuclear in manganese. This interpretation is consistent with not only the above results, but also the access of the complex to the tight confinement of Site 1. Examples in nature of mono-nuclear manganese being coordinated by organic ligands can be seen in proteins requiring strong redox abilities, such as superoxide dismutase, which coordinates a central manganese ion with three amine groups and one hydroxyl group of nearby amino acids, and a nearby water molecule.[110,111]

5

Conclusion

In this work we have done much to further the understanding of the interactions between a manganese (II) ion acting as a secondary electron donor to native bacterial reaction centers. First we confirmed the binding of manganese to two sites in the BRC, previously predicted by ligand-binding simulation software. Next we found multiple forms of evidence through a variety of techniques that Site 1, located at the carotenoid binding site near the inactive bacteriochlorophyll monomer, was the dominant site of electron transfer from the manganese to the BRC. We determined the rate constant of this electron transfer, and clarified that the more rapid rate constant observed after flash was due to a modified observed rate of charge recombination. This modification was found to be from the compound effects of the presence of nearby bound manganese, which both elevated the rate constant of charge recombination from the $P^+Q_A^-$ state, and inhibited electron transfer from Q_A to Q_B. A molecular mechanism for this inhibition was proposed. Finally we examined the biological feasibility of an evolutionary pathway to oxygenic photosynthesis, involving manganese acting as an electron donor to ancient anoxygenic photosynthetic organisms. From these results and considerations, we can offer the evolutionary transition scheme, from anoxygenic to oxygenic photosynthesis, of Figure 5.1. On top of this we also furthered the characterization of the coordinated manganese electron donor, providing evidence for a complex homogeneous in manganese, and likely composed of a single manganese ion.

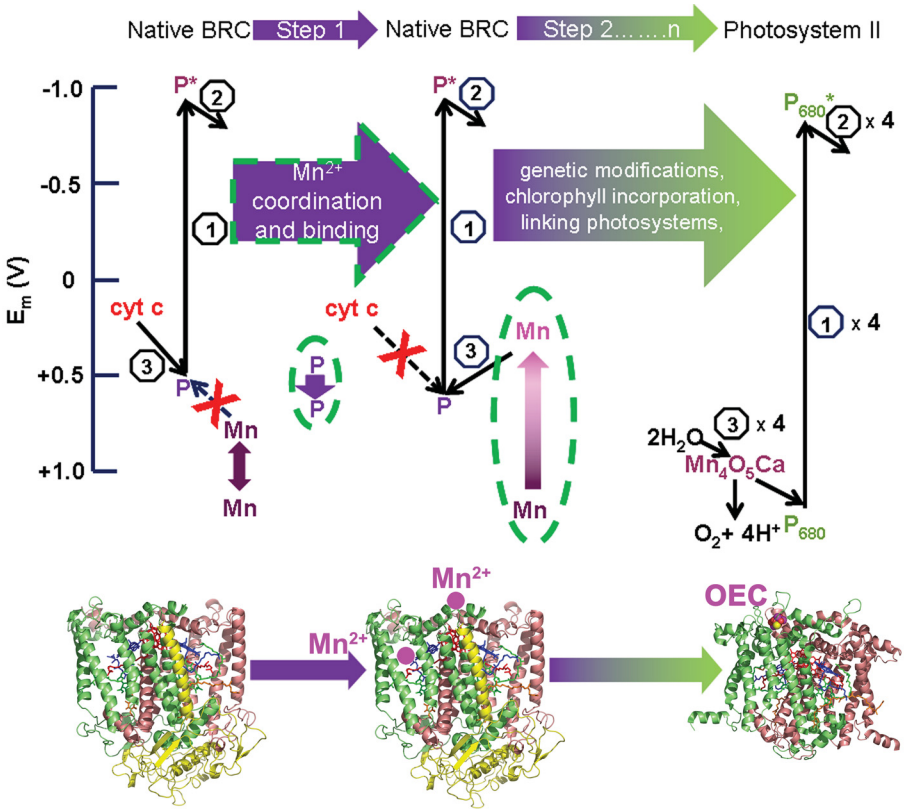

Figure 5.1: Proposed scheme of evolution to oxygenic photosynthesis. Bar diagram on left shows oxidation potentials of secondary and primary electron donors of the RCs. Arrows show thermodynamically possible ETs. In Step 1 Mn is coordinated to a low potential complex. It then binds to the anoxygenic RC, elevating the potential of P, and acting as a secondary electron donor. Mn binding and environmental factors inhibit cyt c ET function. Steps 2 to n represent the slow adaptation of this new electron donor by evolution, eventually leading to the OEC of PSII, and of an oxygenic photosynthetic RC.

6

Future work

As divalent metals have been shown to have numerous effects on both the BRC, and other proteins involved in the early processes of photosynthesis,[22,24,101,102] the ability of manganese to act as a secondary electron donor should be tested in chromatophores and eventually live cells. This would be the best way to directly test the biological feasibility of this proposed evolutionary transition. This way we can see whether the cumulative effects of all Mn interactions allow an organism to continue vital functions and survive, and if this is the case, we can determine which secondary electron donor is dominant in this environment, the native cyt c or Mn.

As discussed in Section 4.4.2, BTP, the molecule we have used to coordinate manganese into a low-potential complex, is not likely to have existed in sufficient amounts in the Archean ocean. It would therefore be useful to find more naturally available Mn ligands to create the low-potential complex. Bicarbonate has been shown to have been present in large concentrations, and to coordinate Mn into a complex that significantly lowers its potential.[31] However this potential is still above that of the unmodified P/P^+ potential, at 520 mV compared to 505 mV, making the ET too slow to be biologically feasible. This leads us to our above suggestion of coordination by amino acids with appropriate functional groups. Work has been started to explore Mn coordination by tyrosine, methionine and serine. This will hopefully yield a complex more relevant to this evolutionary transition.

Another interesting potential of the Mn-BRC system worth exploring is its capability to form oxygen. The evolutionary pathway proposed here would eventually lead to a Mn-BRC system in which the oxidized Mn electron donor in turn oxidizes water. However water has a very high oxidation potential of 820 mV at pH 7, far beyond the oxidizing ability of our low-potential Mn complex.[67] It could be possible that the BRC would use Mn as a terminal electron donor, until further evolutionary pressure forced it to adapt its Mn complex to incorporate a more plentiful terminal electron donor. However an intermediate process has been proposed, involving the oxidation of hydrogen peroxide, with a potential of 270 mV at pH 7.[67,112] With this low

potential, hydrogen peroxide could be oxidized by our Mn-BTP complex, with its Mn^{2+}/Mn^{3+} potential of ~400 mV. If accomplished, this would be first-ever evidence of oxygen production by BRCs.

Bibliography

[1] Pipkin B.W., Trent D.D., Geology and the Environment. p. 339. Minneapolis, MN.: West Pub. Co. (1994)

[2] Xiong J. et al., Science 289, 1724 (2000)

[3] Schubert W.D. et al., J. Mol. Biol. 280, 297 (1998)

[4] Des Marais D.J., Science 289, 1703 (2000)

[5] Dismukes G.C. et al., Proc. Natl. Acad. Sci. 98, 2170 (2001)

[6] Ananyev G.M. et al., Biochim. Biophys. Acta 1503, 52 (2001)

[7] Pierson B.K., The emergence, diversification, and role of photosynthetic eubacteria. p. 161–180. New York: Columbia University Press (1994)

[8] Koepke J. et al., J. Mol. Biol. 371, 396 (2007)

[9] Umena Y. et al., Nature 473, 55 (2011)

[10] Ke B., Advances in Photosynthesis 10, Photosynthesis: Photobiochemistry and Photobiophysics. Dordrecht, The Netherlands: Kluwer, p. 47-305 (2001)

[11] deWinter A., Boxer S.G., J. Phys. Chem. B 103, 8786 (1999)

[12] Pan J. et al., J. Phys. Chem. B 115, 7058 (2011)

[13] Axelrod H.L. et al., Photosynth. Res. 85, 101 (2005)

[14] Borisov A.Y., Topics in Photosynthesis 3, Photosynthesis in relation to model systems. Amsterdam, Holland: Elsevier, p. 2-26 (1979)

[15] Deshmukh S., M.Sc. thesis, Concordia University (2009)

[16] van Mourik F. et al., Biochim. Biophys. Acta 1504, 311 (2001)

[17] Trotta M. et al., Mat. Sci. Eng. C 22, 263 (2002)

[18] Sperotto M.M., Mouritsen O.G., Biophys. J. 59, 261 (1991)

[19] Bowie J.U., J. Mol. Biol. 272, 780 (1997)

[20] Lag S., BSc. honors thesis, Concordia University (2014)

[21] Clayton R.K., Photosynth. Res. 73, 63 (2002)

[22] Deshmukh S., Ph.D. thesis, Concordia University (2013)

[23] Parson W.W., Modern Optical Spectroscopy. Berlin, Germany: Springer-Verlag, p. 174-188 (2007)

[24] Ivanescu M.A., M.Sc. thesis, Concordia University (2014)

[25] Clayton R.K., Photosynthesis: Physical mechanisms and chemical patterns. Cambridge, U.K.: Cambridge University Press (1980)

[26] Dutton P.L., Jackson J.B., Eur. J. Biochem. 30, 495 (1972)

[27] Kálmán L. et al., Nature 402, 696 (1999)

[28] Thielges M. et al., Biochem. 44, 7389 (2005)

[29] Kálmán L. et al., Biochem. 42, 11016 (2003)

[30] Terentyev V.V. et al., Biochem. (Moscow) 76, 1360 (2011)

[31] Khorobrykh A. et al., Chem. BioChem. 14, 1725 (2013)

[32] Melaina M.W. et al., Alternative Fuel Infrastructure Expansion: Costs, Resources, Production Capacity, and Retail Availability for Low-Carbon Scenarios., Golden, Colorado: National Renewable Energy Laboratory (2013)

[33] Carmo M. et al. Int. J. of Hydrogen Energ. 38, 4901 (2013)

[34] U.S. Department of Energy, Energy Efficiency and Renewable Energy Informaiton center: www.eere.energy.gov/informationcenter (2010), accessed December 23, 2015

[35] May M.M. et al., Nature Comm. 6, 8286 (2015)

[36] Marshall J., Nature 510, 22 (2014)

[37] Feher G., Okamura M.Y., The photosynthetic bacteria. New York: Plenum Press, p. 349-386 (1978)

[38] Stanley S.C. et al., Biochim. Biophys. Acta 305, 597 (1973)

[39] Maróti P., Wraight C.A., Prog. Photosynth. Res. 2, 401 (1987)

[40] Williams J.C. et al., Research in photosynthesis. Dordrecht, The Netherlands: Kluwer, p. 377-380 (1991)

[41] McPherson P.H. et al., Biochim. Biophys., Acta 1144, 309 (1993)

[42] Deshmukh S.S. et al., Biochem. 50, 5249 (2011)

[43] O'Reilly J.E., Biochim. Biophys. Acta 292, 509 (1973)

[44] Laurie A.T.R., Jackson R.M., Bioinformatics 21, 1908 (2004)

[45] Ke B. et al., Biochim. Biophys. Acta - Bioenergetics 216, 373 (1970)

[46] Rosen D. et al., Biochem. 19, 5687 (1980)

[47] Deshmukh S. et al., Biochem. 50, 340 (2011)

[48] Yeates T.O. et al., Proc. Natl. Acad. Sci. U.S.A. 85, 7993 (1988)

[49] Roszak A.W. et al., Structure 12, 765 (2004)

[50] Roszak A.W. et al., Biochem. 46, 2909 (2007)

[51] Deshmukh S., Tang K, Kálmán L., J. Am. Chem. Soc. 133, 16309 (2011)

[52] Ermler U. et al., Structure 2, 925 (1994)

[53] Wraight, C.A., Israel J. Chem. 21, 348 (1981)

[54] Ditson S.L. et al., Biochim. Biophys. Acta 766, 623 (1984)

[55] Brackman J.C., Engberts J.B.F.N., Langmuir 8, 424 (1992)

[56] Munkert U. et al., Trends in Colloid and Interface Science VII, Springer, 93, 137 (2008)

[57] Abdel-Rahem R.A., Al-Odail F.A., J. Dispersion Sci. Technol. 35, 1009 (2014)

[58] Pettigrew G.W. et al., Biochim. Biophys. Acta 503, 509 (1978)

[59] Wraight C.A., Stein R.R., FEBS Lett. 113, 73 (1980)

[60] Kleinfeld D. et al., Biochim. Biophys. Acta 766, 126 (1984)

[61] Vermeglio A., Clayton R.K., Biochim. Biophys. Acta 461, 159 (1977)

[62] Gerencsér L., Maróti P., Biopolymers 74, 96 (2004)

[63] Milano F. et al., J. Phys. Chem. B 111, 4261 (2007)

[64] Overfield R.E., Wraight C.A., Photosynth. Res. 9, 167 (1986)

[65] Overfield R.E., Wraight C.A., Biochem. 19, 3322 (1980)

[66] Riegler D. et al., Biochim. Biophys. Acta 1706, 126 (2005)

[67] Blankenship R.E., Hartman H., Trends. Biol. Sci. 23, 94 (1998)

[68] Katona G. et al., J. Mol. Biol. 331, 681 (2003)

[69] Arnoux B. et al., Acta Crystallogr., Sect. D: Biol. Crystallogr. 51, 368 (1995)

[70] Bushnell G.W. et al., J. Mol. Biol. 214, 585 (1990)

[71] Axelrod H.L. et al., J. Mol. Biol. 319, 501 (2002)

[72] Roth M. et al., Biochem. 30, 9403 (1991)

[73] Rivas E. et al., Biochem. 19, 2943 (1980)

[74] Middendorf T.R. et al.,Biochim. Biophys. Acta 1143, 223 (1993)

[75] Zinth Q. et al., Series in Chemical Physics on Antennas and Reaction Centers of Photosynthetic Bacteria. p. 97 (Berlin: Springer) (1985)

[76] Steffen M.A. et al., Science 264, 810 (1994)

[77] Williams J.C. et al., Biochem. 40, 15403 (2001)

[78] Antosiewicz J. et al., J. Mol. Biol. 238, 415 (1994)

[79] Mauzerall D.C. et al., Biophys. J. 68, 275 (1995)

[80] Demchuk E., Wade R.C., J. Phys. Chem. 100, 17373 (1996)

[81] Clayton R.K., Biochim. Biophys. Acta 504, 255 (1978)

[82] Debus R.J. et al., Biochem. 24, 2488 (1985)

[83] Eastman J.E. et al., Biochem. 39, 14787 (2000)

[84] Moser C.C., Dutton P.L., Biochim. Biophys. Acta 1101, 171 (1992)

[85] Dutton P.L. et al., FEBS Lett. 36, 171 (1973)

[86] Osvath S., Maróti P., Biophys. J. 73, 972 (1997)

[87] Lin S. et al., J. Phys. Chem. B 103, 4757 (1999)

[88] Goushcha A.O. et al., J. Phys. Chem. B 101, 259 (1997)

[89] Kalman L., Maróti P., Biochem. 36, 15269 (1997)

[90] Stowell M.H.B. et al., Science 276, 812 (1997)

[91] Deshmukh S.S. et al., Biochem. 50, 3321 (2011)

[92] Li J. et al., Biochem. 37, 2818 (1998)

[93] Graige M.S. et al., Proc. Natl. Acad. Sci. 95, 11679 (1998)

[94] Stowell M.H.B et al., Science 276, 812 (1997)

[95] Lancaster R., Michel H., Structure 5, 1339 (1997)

[96] Kleinfeld D. et al., Biochem. 23, 5780 (1984)

[97] Paddock M.L. et al., Proc. Natl. Acad. Sci. U.S.A. 96, 6183 (1999)

[98] Axelrod H.L. et al., Proc. Natl. Acad. Sci. U.S.A. 97, 1542 (2000)

[99] Gerencser L., Maroti P., Biochem. 40, 1850 (2001)

[100] Maroti P., Wraight C.A., Biophys. J. 73, 367 (1997)

[101] Lorusso M. et al., Eur. J. Biochem. 197, 555 (1991)

[102] Link T.A., Vonjagow G., J. Bio. Chem. 270, 25001 (1995)

[103] Johnsona J.E. et al., Proc. Natl. Acad. Sci. USA 110, 11238 (2013)

[104] Sauer K., Yachandra V.K., Proc. Natl. Acad. Sci. USA 99, 8631 (2002)

[105] Gold M.H. et al., Manganese and Its Role in Biological Systems. p. 559-586 New York: Marcel Dekker Publishers (2000)

[106] Holland H.D., The Chemical Evolution of the Atmosphere and Oceans. Princeton: Princeton Univ. Press (1984)

[107] Fischer W.W., Knoll A.H., Geol. Soc. Am. Bull. 121, 222 (2009)

[108] Kempe S. et al., Nature 349, 605 (1991)

[109] Trotta M. et al., Int. J. Pharm. 241, 319 (2002)

[110] Borgstahl G.E. et al., Cell 71, 107 (1992)

[111] Miller A.F., Curr. Opin. Chem. Biol. 8, 162 (2004)

[112] Bader K.P. Biochim. Biophys. Acta 1188, 213 (1994)